Electronic Thesis and Dissertation Repository

11-27-2017 2:00 PM

Time Series Analysis of Surface Deformation Associated With Fluid Injection and Induced Seismicity in Timpson, Texas Using DInSAR Methods

Simon Thorpe
The University of Western Ontario

Supervisor
Tiampo, Kristy F.
The University of Western Ontario Co-Supervisor
Atkinson, Gail M.
The University of Western Ontario

Follow this and additional works at: https://ir.lib.uwo.ca/etd

Part of the Geophysics and Seismology Commons

Abstract

In recent years, a rise in unconventional oil and gas production in North America has been linked to an increase in seismicity rate in these regions (Ellsworth, 2013). As fluid is pumped into deep formations, the state of stress within the subsurface changes, potentially reactivating pre-existing faults and/or causing subsidence or uplift of the surface. Therefore, hydraulic fracturing and/or fluid disposal injection can significantly increase the seismic hazard to communities and structures surrounding the injection sites (Barnhart et al., 2014). On 17th May 2012 an Mw4.8 earthquake occurred near Timpson, TX and has been linked with wastewater injection operations in the area (Shirzaei et al., 2016). This study aims to spatiotemporally relate, wastewater injection operations to seismicity near Timpson using differential interferometric synthetic aperture radar (DInSAR) analysis. Results are presented as a set of time series, produced using the Multidimensional Small Baseline Subset (MSBAS) InSAR technique, revealing two-dimensional surface deformation.

Keywords

Co-Authorship Statement

Original RADARSAT-2 DInSAR scripts (Appendix A) were provided by Dr. Kristy Tiampo, which formed the basis of my RADARSAT-2 processing in Chapter 3. Sentinel-1A scripts (Appendix C and D) were written entirely by myself, as well as ALOS PALSAR 1 and 2 processing scripts (Appendix B). MSBAS software was developed by Samsonov & D'Oreye, (2017) and was accessed for free at http://www.insar.ca/. Processing of all DInSAR datasets using *GAMMA* and running of the MSBAS algorithm in *C++*, were performed entirely by myself. Differential interferogram results presented in Chapter 4 were written by myself, using a combination of *Generic Mapping Tools (GMT)* and *Python*, with suggestions for improvements from Dr. Kristy Tiampo, Dr. Sergey Samsonov and Dr. Wanpeng Feng. Elastic model script was acquired from Le Mouélic et al., (2002). Processing of the model was performed using *IDL* and plotting in *MATLAB* (Chapter 5.2) was assisted by Shaun Hadden. Finally, discussions and conclusions on the success of implementing MSBAS at Timpson, including the recommendations for future work were developed entirely by myself.

Acknowledgements

Table of Contents

List of Tables

List of Figures

List of Appendices

List of Acronyms

ALOS	Advanced Land Observing Satellite
API	American Petroleum Institute
DEM	Digital Elevation Model
DInSAR	Differential Interferometric Synthetic Aperture Radar
DSM	Digital Surface Map
EPA	Environmental Protection Agency
ERS	European Remote-sensing Satellite
ESA	European Space Agency
FBD	Fine Beam Dual
FBS	Fine Beam Single
GMT	Generic Mapping Tools
GPS	Global Positioning System
GR	Gamma Ray
InSAR	Interferometric Synthetic Aperture Radar
IW	Interferometric Wide Swath
LOS	Line-of-sight
MCF	Minimum Cost Flow
MSBAS	Multidimensional Small Baseline Subset
PALSAR	Phased Array type L-band Synthetic Aperture Radar
PDF	Probability Density Function
PE	Photoelectric Absorption
PRF	Pulse Repetition Frequency
PS	Persistent Scatterer
RADAR	Radio Detection and Ranging
RRC	Texas Railroad Commission
SAR	Synthetic Aperture Radar
SBAS	Small Baseline Subset
SLC	Single Look Complex Image
SNR	Signal-to-noise Ratio
SP	Spontaneous Potential
SRTM	Shuttle Radar Topography Mission
SVD	Singular Value Decomposition
TOPS	Terrain Observation by Progressive Scans
TX	Texas
UIC	Underground Injection Control
USGS	United States Geological Survey
WGS	World Geodetic System

Chapter 1

1   General Introduction

1.1   Motivation

In recent years, parts of central United States and western Canada, regions considered geologically stable, have seen a large increase in number of earthquakes (McGarr et al., 2015). In the US alone, there have been more than 1570 earthquakes with moment magnitude (M_w) $\geq$ 3 between 2009 and 2015 (Ellsworth, 2013; Rubinstein & Mahani, 2015). This rise in seismicity coincides with a recent increase in unconventional oil and gas extraction techniques such as hydraulic fracturing, as well as wastewater disposal. Deep disposal of wastewater fluids in particular has been linked to the major increase in seismicity in central US, including Texas and Oklahoma (Weingarten et al., 2015). Many of these events, such as the 2012 M_w 4.8 Timpson, TX earthquake, were preceded by high-rate injection (>300,000 barrels per month) of wastewater, suggesting a link between wastewater injection activity and seismicity (Frohlich et al., 2014; Shirzaei et al., 2016).

As wastewater is pumped into the subsurface at a high-rate, this may cause the surface of Earth to uplift, which can be detected using geodetic remote sensing techniques. For example, Differential Interferometric Synthetic Aperture Radar (DInSAR) is a space-borne remote sensing technique that measures deformation of Earth's surface at high resolution (millimeter scale), covering large areas and acquiring images in any weather condition, day or night (Wright, 2002). Combining surface deformation from multiple satellites, the two-dimensional (east-west and vertical) deformation time series can be constructed (Berardino et al., 2002; Ferretti et al., 2001; Samsonov & D'Oreye, 2017). In this study, I focus on using advanced time series analysis and DInSAR methods to relate induced seismicity and wastewater disposal at Timpson, TX.

1.2   Aims, Objectives and Organization of Work

The aim of this thesis is to spatiotemporally relate induced seismicity and wastewater disposal activities at Timpson, using advanced DInSAR (Differential Interferometric Synthetic Aperture Radar) analysis. This will be achieved by applying differential interferometry and time series analysis using data from four space-borne satellites, RADARSAT-2, ALOS, ALOS-2 and Sentinel-1A. Upon acquiring data over the region, I apply advanced DInSAR analysis for each individual satellite, producing a highly coherent stack of interferograms. I will apply time series analysis by combining images from different satellites, using the Multidimensional Small Baseline Subset (MSBAS) technique, which will reveal the spatial and temporal correlation between induced seismicity and wastewater disposal activities. Finally, I model the associated deformation using a simple elastic model and compare results to previous studies.

Chapter 1 provides a general introduction to induced seismicity in North America, including central and eastern US and western Canada. Also discussed are the basic principles behind Synthetic Aperture Radar (SAR) and SAR interferometry (InSAR), the technique used in this study. Finally, time series analysis methods are presented, including the MSBAS approach.

Chapter 2 focusses on the area of interest for this study, Timpson, TX, where I discuss the recent induced seismicity in the region and associated wastewater disposal activity. Finally, I discuss the geology of the region, including the geological setting and analysis of well logs that were acquired in this study.

Chapter 3 discusses the methodology of this study, explaining the four satellites used to perform DInSAR analysis. In particular, I discuss the individual processing steps involved with DInSAR analysis and MSBAS processing procedure used to calculate time series over the Timpson region.

In Chapter 4 I discuss the differential interferogram results for each satellite used in this study, along with SBAS and MSBAS time series results for Timpson.

Finally in Chapter 5, the time series results are discussed and a simple elastic model is applied to model the surface displacements. I close by presenting the future work and final conclusions of this investigation.

1.3 Induced Seismicity

Induced seismicity is a term used frequently in scientific literature, defined as, those earthquakes that are attributed to human (anthropogenic) activities, including reservoir impoundment behind dams, enhanced geothermal development, injection or withdrawal of fluids from the subsurface, mining or underground nuclear tests (Eaton, 2017). However, for the remainder of this thesis the term *induced seismicity* applies to seismic events associated with the injection and withdrawal of fluids due to oil and gas production.

The following sections describe the increase in seismicity in North America (including western Canada and mid-continental United States), earthquakes induced by both hydraulic fracturing and wastewater disposal and surface deformation linked with deep disposal of wastewater.

1.3.1 Induced Seismicity in North America

The recent increase in use of unconventional oil and gas extraction techniques such as hydraulic fracturing and horizontal drilling, has been linked to increased seismic activity in North America. The recent advances in these technologies have resulted in their widespread use in regions across western Canada and the central United States and the profitable production of large volumes of oil and gas resources in regions which were previously uneconomical (The Academy of Medicine Engineering and Science of Texas, 2017).

It has been known since the 1960s that the injection of fluids into the subsurface induces earthquakes (Simon, 1969). Between 1962 and 1965, large volumes of toxic wastewater were injected at the Rocky Mountain Arsenal near Denver, Colorado. Evans (1966) found a relationship between wastewater injection and seismicity in the region, whereby 710 earthquakes were detected in the Denver area. Similarly, in northwestern Colorado, an

experiment was setup to investigate the relationship between seismicity and fluid injection at Rangely. By varying the fluid injection pressure, the US Geological Survey (USGS) discovered a correlation between deep water well injection and seismicity, whereby 976 earthquakes were recorded between 1962 and 1972 in the Rangely Oil Field (Gibbs et al., 1973).

However, recently has the US and Canada seen an unprecedented increase in seismicity related to fluid injection. A study by Ellsworth (2013) found there was a rapid increase in the rate of seismicity in central and eastern United States beginning in 2003, as shown in Figure 1-1. From 1967 to 2000 there was, on average, a rate of 21 earthquakes per year with $M \geq 3$, highlighted by the dashed line. However, this increased to a rate of 300 events per year from 2010 to 2012 (Ellsworth, 2013).
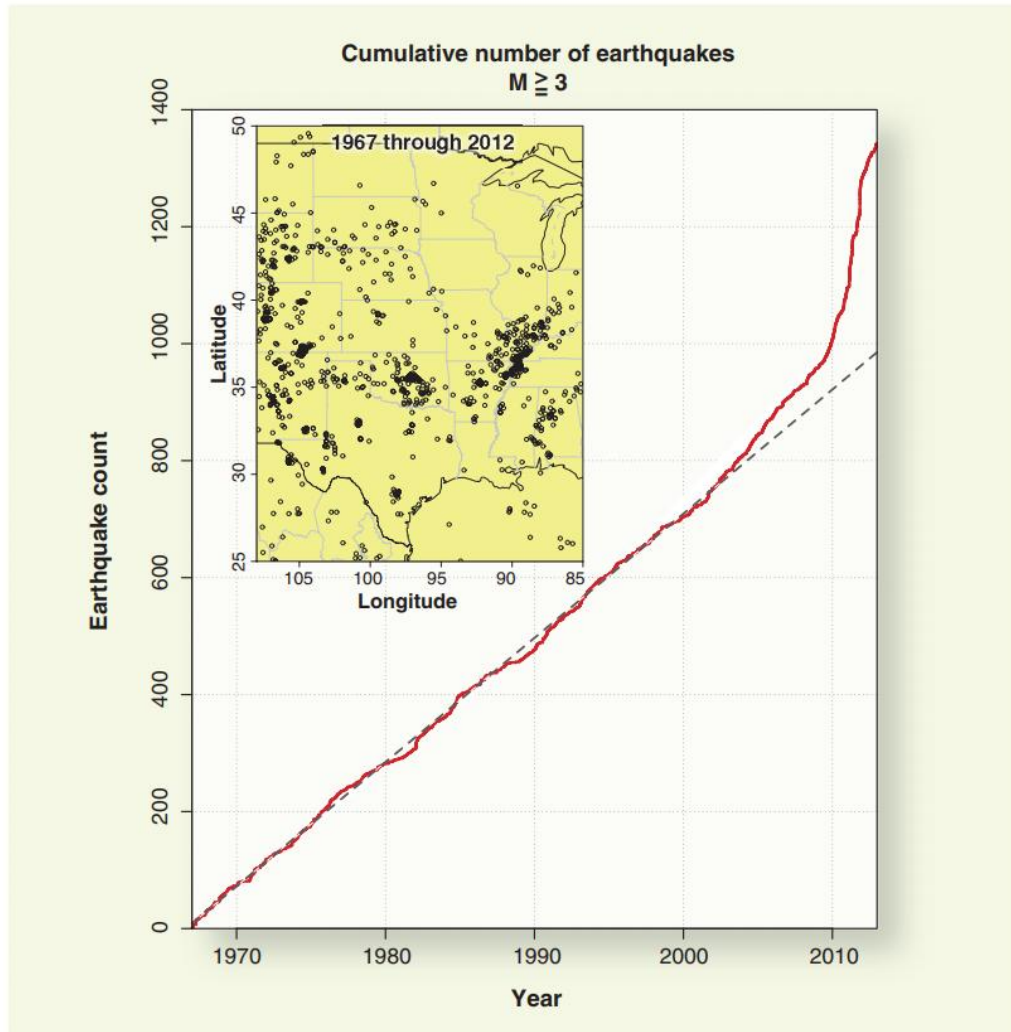
Figure 1-1 Cumulative number of earthquakes with M ≥ 3 in central and eastern United States from 1967-2012 (Inset). The dashed line corresponds to the long-term rate of 21 earthquakes per year. (from Ellsworth, 2013).

As well as an increase in seismicity rate, there have been a number of damaging earthquakes which have been attributed to fluid injection activities such as hydraulic fracturing. These include the 2015 M3.9 and 2016 M4.1 Fox Creek earthquakes (Schultz et al., 2017), a series of M2.9 earthquakes in 2011 in South-Central Oklahoma (Holland, 2013) and the 2014 M4.2 Fort St. John earthquake (Atkinson et al., 2015).

In addition to hydraulic fracturing, deep disposal of waste fluids is also another major source of induced seismicity (Weingarten et al., 2015). In fact in the central US, most

induced seismicity is linked to deep disposal of wastewater from oil and gas production (Ellsworth, 2013; Frohlich et al., 2014; Ghofrani & Atkinson, 2016; Keranen et al., 2014; McGarr et al., 2015). Induced events as large as M5.8 in 2016 in Pawnee, Oklahoma (Keranen et al., 2014; Yeck et al., 2017) and M4.8 in 2012, Timpson (Frohlich et al., 2014) have been associated with wastewater injection wells.

In general, the hazard associated with earthquakes is proportional to the seismicity rate (Ellsworth, 2013). Therefore, with the recent increase in seismicity in the eastern and central United States, there is also an increase in the seismic hazard in this region.

1.3.2 Earthquakes Induced by Hydraulic Fracturing and Wastewater Disposal

Although the greatest attention on induced seismic hazard has been on wastewater disposal, hydraulic fracturing (often referred to as *fracking*) is increasingly becoming recognized as another major source of induced seismicity (Atkinson et al., 2016).

Hydraulic fracturing and horizontal drilling techniques target hydrocarbon-rich, low permeability oil and gas reservoirs, where fluid is pumped into the formations at high pressure to form fractures that allow otherwise trapped oil and gas to escape. This process generates micro-fractures – such that the increase in subsurface pore pressure causes the rock to fracture or stimulate slip across pre-existing fractures (Rubinstein & Mahani, 2015). Hydraulic fractures are pumped in stages, generating micro-earthquakes typically with $M_w < 1$ which are too small to be felt at the surface (Ellsworth, 2013). However, in cases where hydraulic fracturing induces larger earthquakes which can be felt at the surface, these earthquakes are likely related to the reactivation of proximal pre-existing faults (Rubinstein & Mahani, 2015).

Once hydraulic fracturing has been completed, the well can undergo its production phase, to extract oil and gas from the now fractured subsurface. These production wells extract oil and gas and as a byproduct, brine water. This water is found alongside oil and gas within the rock formation and is commonly termed "produced water". This produced water is highly mineralized and unsuitable for other purposes, so must be disposed of in deep, porous reservoirs. In the US, waste disposal wells are regulated by the US

Environmental Protection Agency (EPA) as UIC (Underground Injection Control) Class II wells.

The amount of fluid injected into waste disposal wells can vary greatly, with some injecting around 20 m^3/month and others greater than 160,000 m^3/month (Rubinstein & Mahani, 2015). However, on average, injection rates for disposal wells remain much larger compared to hydraulic fracturing operations (around only 2500 m^3 total injected volume during an entire hydraulic fracturing procedure (Schultz et al., 2015)). Due to the large injection volumes associated with wastewater disposal wells, which greatly surpasses volumes injected by hydraulic fracturing, wastewater disposal presents a significant source for inducing earthquakes (Rubinstein & Mahani, 2015).

An earthquake occurs when a fault slips, releasing stored elastic strain energy. A fault will remain locked if the applied shear stress is less than the stresses holding the fault together. The failure of a fault is dependent on the effective shear stress $\tau_{crit} = \mu(\sigma_n - P) + \tau_0$ where τ_{crit} is the critical shear stress (Ellsworth, 2013). This critical shear stress is a function of the coefficient of friction μ, effective normal stress σ_n and pore pressure P. As fluid is injected into the subsurface, through hydraulic fracturing or wastewater disposal, pore pressure increases, reducing normal stress and lowering the critical stress needed to induce rupture. Therefore, a small increase in pore pressure can cause an unstable fault to rupture, releasing the stored elastic strain energy produced during an earthquake.

There are two known primary mechanisms for inducing earthquakes, by means of modifying the stress and/or pore pressures at proximal, pre-existing faults (Ellsworth, 2013). First, injected fluid directly interacts with pre-existing faults through high-permeability pathways, increasing the pore-fluid pressure within the fault. This mechanism lowers the normal stress and effectively reduces the frictional resistance to slip so the fault is more prone to fail. The second mechanism involves changing the shear and normal stresses indirectly acting on proximal faults. Slip is induced through changing the loading conditions on the fault, whereby there is no direct hydrologic connection between the fault and injected fluid (Ellsworth, 2013).

1.3.3   Wastewater Disposal and Associated Surface Deformation

There have been many studies linking induced seismicity and associated wastewater disposal activity (Healy et al., 1968; Keranen et al., 2013; Shirzaei et al., 2016). However less documented is the hazard associated with surface deformation due to wastewater disposal.

As above, injecting large volumes of fluid into the subsurface causes an increase in pore pressure in the underlying hydrogeologic system. This increase in pressure in the reservoir results in reservoir swelling, producing surface *uplift* (Chen, 2012). Likewise, if fluid is being withdrawn from the subsurface, the pressure decrease will cause the reservoir to contract and produce surface *subsidence*. Therefore, measuring deformation at the surface, which can be done using various geodetic techniques, provides a method for detecting the hydrogeological evolution of the subsurface (Shirzaei et al., 2016). Of these geodetic techniques, tilt meters, global positioning system (GPS) and interferometric synthetic aperture radar (InSAR), have all been successfully applied to monitor fluid flow (Vasco et al., 1998), wastewater disposal (Shirzaei et al., 2016) and carbon dioxide (CO_2) storage (Vasco et al., 2010; Czarnogorska et al., 2014).

Over time as fluid is injected into the subsurface, pore pressure perturbations can diffuse over large distances. For example, Keranen et al. (2014) modelled fluid pressure perturbations that propagated up to 35 kilometers to trigger seismicity in central Oklahoma. Pore pressure increases at a faster rate for permeable reservoirs, compared to surrounding low permeability formations (Chen, 2012). This increase in pore pressure within the reservoir must be accommodated through expansion that deforms the surrounding rocks and translates to the surface as *uplift*.

There have been many studies measuring surface deformation related to subsurface fluid flow including, wastewater injection, hydraulic fracturing, geothermal heat extraction, groundwater use and CO_2 storage. Vasco et al. (2010) successfully used InSAR measurements of surface deformation to reveal fluid flow associated with the geological storage of CO_2. Figure 1-2 shows surface deformation of up to 5 mm/year surrounding

these CO_2 injection sites. From 2004 to 2008, 3 million tons of CO_2 had been injected at a depth of 1800 to 1900 meters.
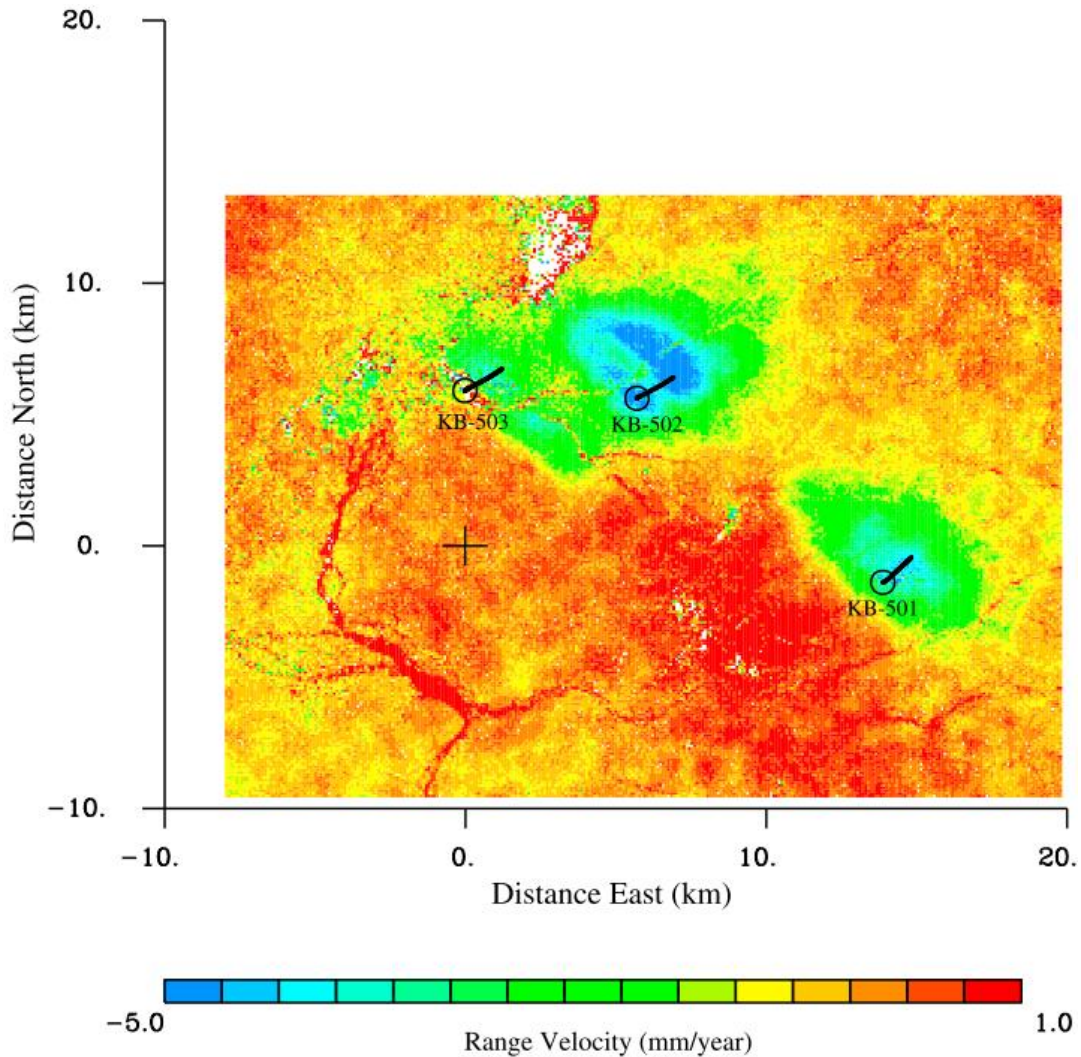
Figure 1-2 Range velocities (mm/year) from DInSAR measurements of surface deformation due to CO_2 injection at In Salah, Algeria. Negative range velocities infer surface uplift of up to 5 mm/year surrounding the injection sites (KB-501, KB-502 and KB-503), from Vasco et al. (2010).

Similarly, Shirzaei et al. (2016) used DInSAR measurements to detect surface uplift due to wastewater disposal at Timpson, TX, a location where an M_w 4.8 event occurred on

17th May 2012. Using satellite measurements over a 4-year period, up to 3 mm/year uplift was detected (Figure 1-3) and models of the injected fluid showed a pore pressure increase of ~1MPa.
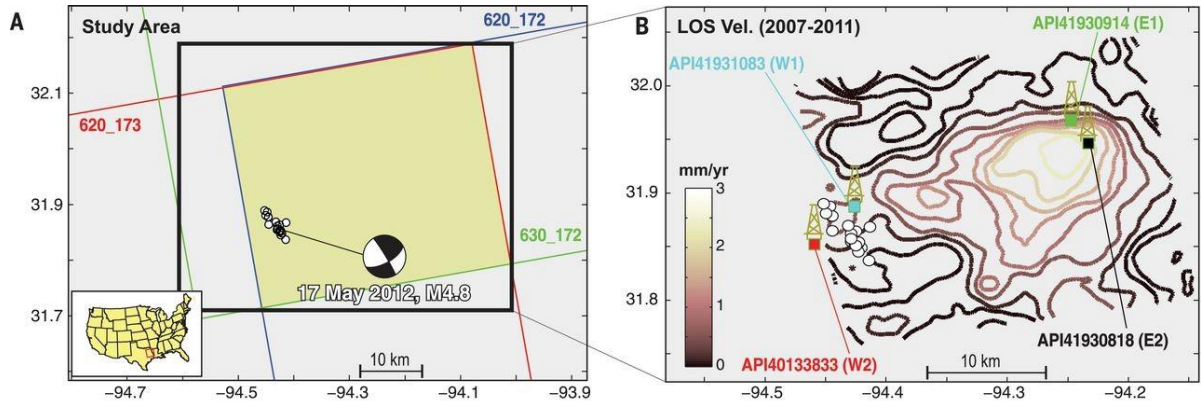
Figure 1-3 A) region of induced seismicity over the 2012 Timpson, TX earthquake sequence (white circles) and associated focal mechanism, along with three overlapping InSAR frames used to model for wastewater injection. **B)** Contour map of line-of-sight (LOS) velocity field with four major injection wells labelled along with location of seismicity from Shirzaei et al. (2016).

1.4   Differential Interferometric Synthetic Aperture Radar

DInSAR is an effective space-borne, remote sensing application that images the surface of the Earth, in all weather conditions, in order to reveal subtle ground deformation. In this section, synthetic aperture radar (SAR) will be introduced along with interferometric synthetic aperture radar (InSAR), before DInSAR analysis and its limitations are discussed.

1.4.1   Synthetic Aperture Radar (SAR)

Synthetic Aperture Radar (SAR) is a space-borne remote sensing imaging system which actively illuminates the surface of the Earth with electromagnetic pulses, typically with radio- and micro- wavelengths (Hanssen, 2001). SAR provides the ability to measure surface deformation with high spatial and temporal resolution. Combining multiple images allows for the construction of a temporally dense time series of ground

displacement (Berardino et al., 2002; Ferretti et al., 2001; Samsonov & D'Oreye, 2017). SAR is an active technique, whereby it transmits its own electromagnetic energy at the surface and records the energy reflected back to the sensor.

Radio detection and ranging, or radar, was driven by the findings of Maxwell's equations of electromagnetism in 1873 and Hertz' experiments in 1866 (Franceschetti & Lanari, 1999). Radar systems were first fitted to air-borne satellites for military purposes, before an L-band SAR system onboard Seasat was launched in 1978 to measure ocean topography (Hanssen, 2001), a mission that paved the way in satellite remote sensing.

Initially, satellite remote sensing began with optical systems, such as the Landsat satellites utilizing visible to infrared wavelengths. However, these optical satellites were severely limited by cloud coverage and lack of solar illumination. Radar satellites overcame these issues, using radar- and micro-waves (typically 5-25 cm wavelength) around 100000 times longer than optical wavelengths and which can penetrate through clouds (Wright, 2002). Therefore, radar satellites can collect data in any weather condition and day or night.

SAR satellites image the surface of the Earth by aligning the radar antenna parallel with the satellite`s orbit, side-looking down at an inclined angle (look angle). The conventional imaging geometry of side-looking SAR satellites is shown in Figure 1-4. As the satellite travels along its trajectory at a velocity v, it emits a single pulse at a specific frequency that illuminates a region of the surface (footprint). The emitted pulse may have different wavelengths and frequency characteristics based on the type of sensor. For example, typical SAR pulse wavelengths range from 3 cm (X-band, TerraSAR-X), 6 cm (C-band, Envisat and RADARSAT-2), 10 cm (S-band, NovaSAR-S) to 24 cm (L-band, ALOS) (Ferretti et al., 2007).

SAR satellites are launched into near-polar orbits and provide two viewing angles of the Earth's surface. When the satellite travels from the North to the South Pole, this is known as a descending orbit, whereas an ascending orbit views Earth's surface when travelling from the South to the North Pole.
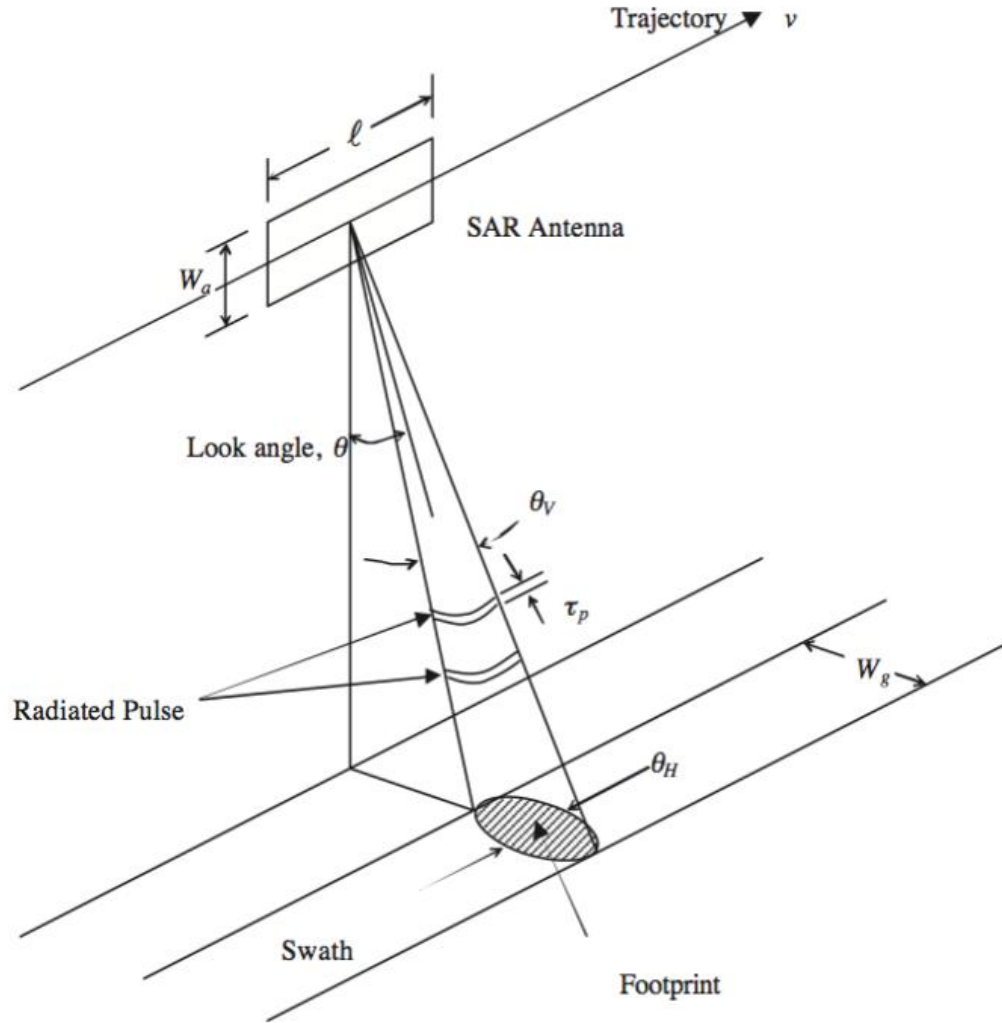
Figure 1-4 Conventional side-looking SAR imaging geometry reproduced from Curlander and Mcdonough, (1991). Satellite velocity (v), antenna length (l), antenna width (W_a), look angle (Θ), beam width (Θ_v), radar pulse duration (τ_p), azimuth beam width (Θ_H) and swath width (W_g) are all shown.

Synthetic aperture, or virtual antenna, is the concept that a large antenna size can be simulated by processing signal from a short, real, antenna. This concept of a long virtual antenna is the basis for SAR to achieve high azimuthal resolution (ESA, 2014). A synthetic aperture is formed by pointing the small radar antenna at the surface, perpendicular to the satellites direction of motion. The radar antenna emits pulses at a

repetition frequency known as the pulse repetition frequency (PRF). The points at which successive pulses are transmitted are interpreted as elements of a large synthetic array. A signal processor within the SAR sensor is then able to process these points to generate a high-resolution SAR image. Therefore, synthetic aperture has the effect of producing a high-resolution image as if it were from a large antenna. The azimuthal resolution of a SAR satellite is approximately half the length of the radar antenna length, and is independent of range distance.

A SAR sensor records echoed backscatter energy, where each pulse represents a small area of the Earth`s surface, known as a resolution cell (Hanssen, 2001). This backscattered energy is dependent on the roughness and dielectric properties of the surface. Combined, these resolution cells form a two-dimensional array (formed of lines and columns) resembling the final digital SAR image. Each of these resolution cells represent a complex number which hold amplitude and phase information of the backscattered electromagnetic energy (Ferretti et al., 2007).

The amplitude information represents the portion of the transmitted energy that is returned to the radar from the surface targets. How the radar energy interacts with the surface is a function of many variables including, the characteristics of the radar system (electromagnetic frequency, polarization and wavelength) and characteristics of the surface conditions (dielectric properties, landcover type, topography and relief) (Canada Center for Mapping and Earth Observation, 2016). Exposed rock and buildings represent strong (bright) amplitudes, whereas low (dim) amplitudes are represented by smooth, flat surfaces which reflect the signal away from the radar, such as water bodies (Ferretti et al., 2007).

When performing interferometry, it is not the amplitude but the phase component of the wave that is used (described in Chapter 1.4.2). We know the wavelength of the radar wave, the phase of the emitted wave and the returned phase of the backscattered energy (returning from a pixel in the SAR image). Therefore, the distance from the satellite to the surface and back is simply a number of whole wavelengths plus some fraction of that wavelength, which is determined from the difference in phase between the emitting and

returning waves (Wright, 2002). In fact, this phase difference can be calculated very accurately, which due to the near perfect sinusoidal nature of the waves, will range uniformly between $-\pi$ and π. The phase component alone appears as a noisy SAR image since it records many different effects which can only be removed by differencing (Massonnet & Feigl, 1998). This is the fundamental principle behind calculating interferograms, as discussed through Chapters 1.4.2 and 1.4.3.

1.4.2   Radar (SAR) Interferometry

The basic principle InSAR utilizes is the phase difference between two radar images taken from the same position but acquired at different times (Wright, 2002). Using the repeat orbit of satellites along a fixed track, two radar images taken at slightly varying look angles can be cross-correlated on a pixel by pixel basis to produce an interferogram. The interferogram amplitude is the amplitude of the first image multiplied by the amplitude of the second, whilst the interferometric phase is simply the phase difference between images (Ferretti et al., 2007).

During two acquisitions from a satellite on a fixed path, if nothing has changed, an identical phase will be recorded at the sensor to that measured previously (Wright, 2002). However, if a point on the surface moves between acquisitions, due to subsidence or an earthquake, a different path length will have been recorded as a phase change. These phase changes are mapped as interference fringes, creating what is known as an interferogram, and is effectively a digital map of surface deformation. Each of these fringes give information on the radar path length and represent a line of constant phase on the Earth's surface.

In reality however, images are not taken from exactly the same location in space, which introduces phase shifts due to orbital separation and surface topography (Wright, 2002). Since we know the exact position of satellites when images are acquired, we are able to calculate the orbital separation and correct for this phase shift in the recorded signal. As the SAR satellite observes the Earth's surface from two different look angles, phase shifts also arise from a stereoscopic effect due to surface topography (Massonnet & Feigl, 1998). However, using a digital elevation model (DEM), we are able to remove this

phase shift in our interferogram. What remains is information relating the phase change to surface deformation across our target area, with some additional nuisance terms such as atmospheric effects.
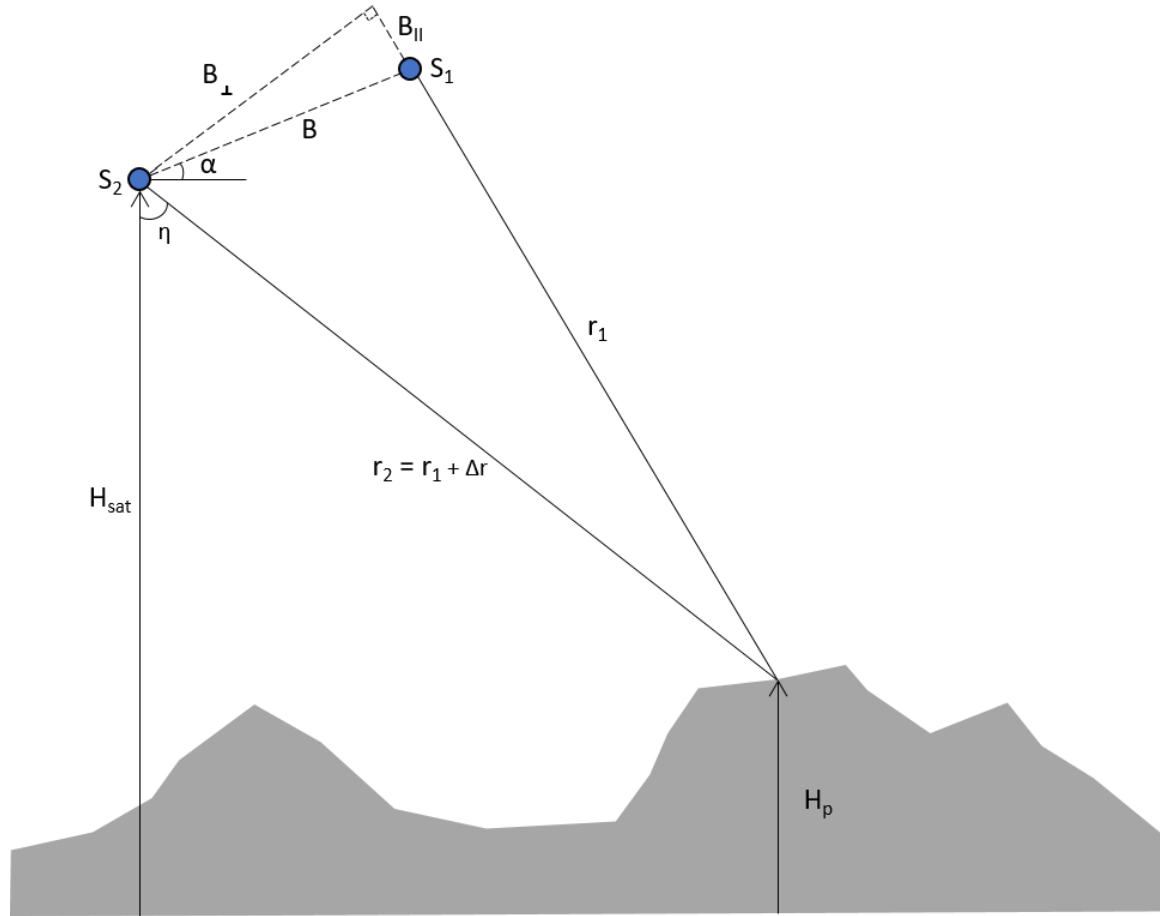
Figure 1-5 Interferometric configuration of two SAR satellite acquisitions at an initial time S_1 and later time S_2. Satellite acquisitions are separated by a spatial baseline B and illuminate the same target on the surface at a look angle η. The spatial baseline can be decomposed into the perpendicular baseline $B_\perp$ and parallel baseline B_{II}. The distance between the surface and satellite is denoted by r_1 and r_2, whereby r_2 is equal to r_1 plus some additional path length Δr.

A typical interferometric image configuration can be seen in Figure 1-5, and from this figure the key physical and geometrical relationships between two SAR observations can be derived (Hanssen, 2001). From two full-resolution SAR images, an interferogram can be created to form an array of x (range) and y (azimuthal) phase values, whereby the interferometric phase for each resolution cell can be written as (Zebker et al., 1994)

$$\Delta\varphi = \frac{4\pi\Delta r}{\lambda}$$ (Equation 1-1)

Here, λ is the radar wavelength, typically 6 cm for C-band satellites. The path length difference between acquisitions $\Delta r = r_2 - r_1$ can then be approximated as,

$$\Delta r = B sin(\eta - \alpha)$$ (Equation 1-2)

an assumption known as the far-field or parallel ray approximation (Zebker & Goldstein, 1986).

In addition to the phase due to surface deformation $\Delta\varphi_{defo}$, there are many other contributions to the recorded interferometric signal,

$$\Delta\varphi = \Delta\varphi_{topo} + \Delta\varphi_{flat} + \Delta\varphi_{defo} + \Delta\varphi_{atmo} + \Delta\varphi_{noise} + \Delta\varphi_{err}$$ (Equation 1-3)

which include effects due to: topography $\Delta\varphi_{topo}$, Earth curvature $\Delta\varphi_{flat}$, atmosphere $\Delta\varphi_{atmo}$, noise $\Delta\varphi_{noise}$ and other errors $\Delta\varphi_{err}$ such as orbital errors. In order to determine surface deformation from the measured interferometric phase, all the above-mentioned contributions must be removed from the signal.

First, the topographic phase contribution is a function of the perpendicular baseline due to differing look angles given by (Zebker et al., 1994),

$$\Delta\varphi_{topo} = \frac{4\pi B_\perp H_p}{\lambda r_1 sin(\eta)}$$ Equation 1-4

Here, H_p is the measured height from an arbitrary reference level (for example an ellipsoid) to the target resolution cell and η is the satellite look angle as shown in Figure 1-5. This shows that the sensitivity of the interferogram due to topography increases with increasing perpendicular baseline $B_\perp$.

This topographic phase can be removed using an external DEM, which is typically derived using interferogram of large perpendicular baseline component (Kenyi & Kaufmann, 2003). For example, the Shuttle Radar Topography Mission (SRTM) (Werner, 2001) mapped Earth's surface between ~60°N/S using C-band and is widely used to correct for topography in the interferometric phase (Hanssen, 2001).

High-resolution InSAR DEMs also can be generated using TerraSAR-X and TanDEM-X satellites (German Aerospace Center, 2014; Kramer, 2014), or digital surface maps (DSMs) using optical imagery such as the GeoEye-1 or WorldView satellites (Satellite Imaging Corporation, 2017). Removing this topographic component of phase is essential in differential interferometry and is discussed in Chapter 1.4.3.

The flat Earth phase is the interferometric phase contribution due to the curvature of the Earth. The removal of this *reference phase* (named after the reference ellipsoid) is performed by interferogram flattening and is defined as (DEOS, 2008),

$$\Delta\varphi_{flat} = \frac{-4\pi}{\lambda} B_\perp \Delta\eta \qquad \text{(Equation 1-5)}$$

where $\Delta\eta$ is the change in look angle between satellite acquisitions. To remove the flat Earth phase, precise satellite orbits are used and a reference surface, most commonly World Geodetic System 1984 (WGS1984). The flat Earth phase is independent from topography and surface deformation and is an important step in interferometry since it can increase phase density and complexity of unwrapping (Ai et al., 2008).

Further interferometric phase errors arise from thermal noise, orbital errors and temporal noise introduced by the difference in look angles, volume scatterers and change in surface properties. However, the atmospheric contribution is the largest source of error in

interferometry and is difficult to eliminate. These limitations are discussed further in Chapter 1.4.4.

Once phase contributions from topography $\Delta\varphi_{topo}$, flat Earth $\Delta\varphi_{flat}$ and the atmosphere $\Delta\varphi_{atmo}$ are accounted for, the remaining phase signal will be mainly due to surface deformation of the ground, parallel to the radar Line-of-sight (LOS). This can be written in the form,

$$\Delta\varphi_{defo} = \frac{4\pi}{\lambda}\Delta\rho \qquad \text{(Equation 1-6)}$$

where $\Delta\rho$ is surface deformation in LOS direction. This implies that ground displacement of half a wavelength in LOS direction produces one interference fringe. For example, for the European Remote-sensing Satellite (ERS) (wavelength λ of 5.6 cm) a single fringe represents 28.3mm of surface displacement. It is also important to note that the interferogram sensitivity to surface deformation is independent to the satellite configuration (Samsonov, 2007)

From Equation 1-4 and Equation 1-6, we can compare the sensitivity of the interferometric phase due to surface displacement $\Delta\varphi_{defo}$ and topography $\Delta\varphi_{topo}$ (Hanssen, 2001),

$$\delta\phi = -\frac{4\pi}{\lambda}(\Delta\rho - \frac{B_\perp}{r_1\sin(\eta)}H_p) \qquad \text{(Equation 1-7)}$$

This relationship demonstrates that for space-borne satellites, sensitivity to surface deformation is approximately one thousand times greater than the sensitivity due to topography (Samsonov, 2007).

1.4.3　Differential Interferometry

DInSAR aims to measure ground deformation, with sub-centimeter precision and high spatial resolution and coverage using repeat-pass interferometry (Czarnogorska et al., 2014). The resulting differential interferogram can be constructed via several methods including, two-pass, three-pass and four-pass techniques. Using repeatedly acquired SAR

data from a single sensor, the line-of-sight (LOS) time series of ground deformation can then be determined (Czarnogorska et al., 2014).

DInSAR satellites therefore are ideal for monitoring surface deformation, and have been widely applied across the field of geophysics. These include volcano monitoring (Samsonov et al., 2017; Weissel et al., 2004), earthquake cycle analysis (Wright et al., 2001; Wright, 2002), resource extraction (Amelung et al., 1999; Motagh et al., 2007), glacial ice motion (Goldstein et al., 1993; Schneevoigt et al., 2012), thematic mapping (Santoro et al., 2009) and landslides (Nishiguchi et al., 2017). SAR systems have the ability to map a continuous region, many tens of kilometers in width (Zebker et al., 1994), with the precision of a small fraction of the radar wavelength (Wright, 2002).

As discussed in Chapter 1.4.2, it is first necessary to remove the topographic contribution from the interferometric phase, leaving the ground displacement component. Two-pass DInSAR method uses a DEM that is converted to radar coordinates and subtracted from the interferogram (Massonnet et al., 1993). In regions where a DEM is available (between ~60°N/S for SRTM), this two-pass approach is an effective method. It is important to note that any errors in the external DEM will propagate into the final deformation results in the final interferogram. The magnitude of this propagated error depends on the baseline characteristics, whereby larger perpendicular baselines result in larger topographic error, as shown in Equation 1-4 (Hanssen, 2001).

However, in regions where a DEM is not available or of poor quality, an extra SAR acquisition is combined with an appropriate partner acquisition to create a *topographic pair*. In this three-pass method, this pair is assumed to have no deformation and a small perpendicular baseline with good coherence. This *topographic* pair can then be unwrapped, scaled to the baseline of the *deformation pair* and subtracted from it to produce a differential interferogram (Hanssen, 2001). Further techniques such as the four-pass method can be applied to generate a differential interferogram when a common image is not available between the deformation and topographic pair.

1.4.4 DInSAR Limitations

DInSAR analysis relies on the correlation between two images that make up the interferogram. In other words, DInSAR works only under coherent conditions, whereby it is only possible if the character of the ground surface does not change between acquisitions (Wright, 2002). Any significant surface change can lead to a random phase contribution, affecting the phase measurement, known as *decorrelation*. There are many sources of decorrelation in the interferometric phase. The observed decorrelation δ_{obs} can be presented as the multiplicative sum of its components,

$$\delta_{obs} = \delta_{geom}\delta_{process}\delta_{vol}\delta_{therm}\delta_{dop}\delta_{temp}\delta_{atmo} \qquad \text{(Equation 1-8)}$$

highlighting the major contributions to decorrelation, geometric δ_{geom}, processing $\delta_{process}$, volume δ_{vol}, thermal δ_{therm}, doppler δ_{dop} and temporal δ_{temp}. Each of these components are fully described in Zebker and Villasenor (1992) with the major sources summarized below.

Changes in surface characteristics is the main contribution to decorrelation in the interferometric phase. Scattering properties of the surface will vary based on the type of surface coverage, for example vegetation or snow do not retain correlation for long time periods, whereas rock outcrops or buildings often remain coherent for a long time. This is particularly an issue in vegetated areas, such as forests, where if a C-band system (wavelength = ~6 cm) is used, the signal will decorrelate rapidly (Wright, 2002). Decorrelation can also occur when the surface deforms rapidly, for example during a landslide or large earthquake, causing steep phase gradients that cannot be detected by DInSAR (Samsonov et al., 2017).

Other than the above contributions, which affect the coherence of a differential interferogram, there are other limitations associated with DInSAR measurements. For example, the largest source of error in DInSAR analysis are atmospheric phase delays which are difficult to eliminate. There are three factors that affect atmospheric variability: electron density in the ionosphere, hydrostatic due to pressure changes and a "*wet*" component dependent on water vapor content in the troposphere (Bevis & Businger,

1992; Parker et al., 2015; Thapa & Chatterjee, 2015). These three factors cause phase shifts in the interferometric phase, as the electromagnetic waves interact with the electrons and/or water vapor in the atmosphere. Due to the varying electron content in the ionosphere, electromagnetic waves are dispersed and can cause phase shifts around half a wavelength for C-band SAR satellites (Ding et al., 2008). However, phase delay due to water vapor provides the dominant source of atmospheric error in differential interferograms. Water vapor can correlate with surface topography, whereby it concentrates in areas of low relief, causing localized variations in phase delays. Tropospheric delays are often a few cm in magnitude, for example a relative humidity variation of 20% causes 10 cm in surface deformation error (Zebker et al., 1997). An example of the atmospheric effect within an interferogram is shown in Figure 1-6. The lower half of the image shows clear atmospheric phase signals affecting the interferometric phase, with up to 8 cm deformation.
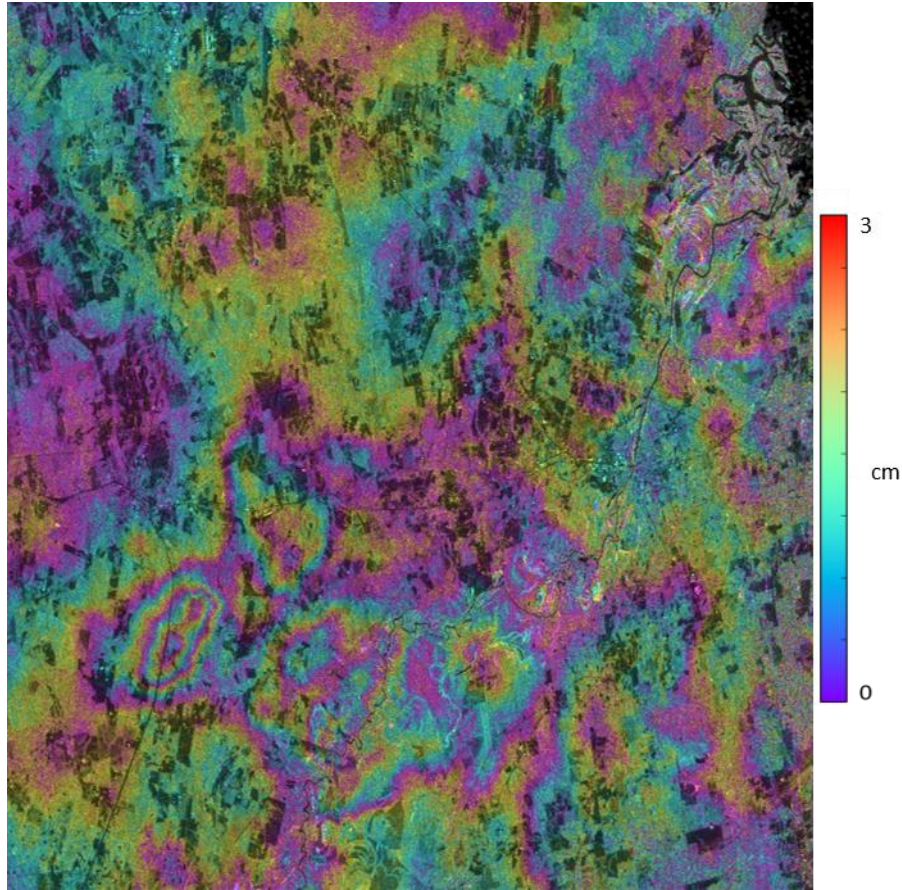
Figure 1-6 Displacement map from ALOS satellite over Timpson, TX, overlaid on the SAR intensity image. Each phase cycle (purple to red), represents 3 cm LOS displacement. Large atmospheric affect can be seen in the lower half of the image.

Atmospheric delays also often correlate with topography, whereby an area of an interferogram with high topography will witness small atmospheric delay (low water vapor content) compared to large delay over low topography (high water vapor content). This is problematic in volcanic studies, where significant topographic relief causes variation in the atmospheric delay across the image. Turbulent atmospheric features may also delay the propagation of electromagnetic waves due to varying humidity, temperature and pressure changes.

A better understanding of the relationship describing atmospheric delay in DInSAR is required in order to mitigate this noise (Samsonov et al., 2017). There have however been developments in this field using other remote sensing techniques to model for

atmospheric changes to correct DInSAR data (Bekaert et al., 2015). First, tropospheric delay effects can be corrected for using GPS or high resolution meteorological models (Ding et al., 2008). Second, a statistical approach could be applied for example using correlation analysis (Sarti et al., 1999). Third, since atmospheric errors are decorrelated in time, interferograms can be stacked to remove the incoherent signal (Zebker et al., 1997).

DInSAR is also limited by its ability to only measure motion in the satellites LOS, so we only have information for a single dimension. This can lead to uncertainties and ambiguities in physical models of surface deformation (Wright, 2002).

However, in time series analysis we are able to combine multiple satellites to decompose the LOS displacement into individual vertical and horizontal components, using Multidimensional Small Baseline Subset (MSBAS) technique for example. Not only is DInSAR limited to measuring a single dimension of motion, due to the polar orbit of SAR satellites, it is also insensitive to measuring north-south (along-track) surface displacements.

1.5   DInSAR Time Series Analysis

1.5.1   Time Series Methods

DInSAR time series analysis is a technique used to map changes on the surface of the Earth through time and space (Berardino et al., 2002; Ferretti et al., 2001; Samsonov & D'Oreye, 2017). Using a large stack of highly coherent interferograms, time series analysis can be applied to determine the temporal characteristics of surface deformation for the entire area where the differential interferograms remain coherent, enabling the analysis of long-term and time-varying surface changes (Lanari et al., 2004).

There are a few methods commonly used in time series analysis, including Persistent Scatterer (PS) (Ferretti et al., 2001; Hooper et al., 2004), Small Baseline Subset (SBAS) (Berardino et al., 2002) and Multidimensional Small Baseline Subset (MSBAS) (Samsonov & D'Oreye, 2017).

The PS approach, for example, identifies "persistent scatterer" pixels. In this method, pixel's whose scattering characteristics remain stable through time when viewed from varying look angles are identified. This method takes advantage of a single point scatterer in a resolution cell, with this point returning significantly more energy than other point scatterers. This reduces decorrelation, thus providing a reliable, coherent phase measurement (Ferretti et al., 2001). StaMPS (Stanford Method for PS) is a method of PS developed by Hooper et al. (2007). This technique uses the spatial correlation of interferogram phase to identify phase-stable pixels even with low amplitude stability, which is useful in rural, highly vegetated areas.

On the other hand, SBAS inverts interferograms to derive surface displacements for incremental time steps (Berardino et al., 2002). This technique is characterized by choosing appropriate differential interferogram combinations with a small orbital separation (or baseline). This method limits the spatial decorrelation in each resolution cell, and applies singular value decomposition (SVD) to invert for surface displacements. However, this technique is limited by the temporal sampling of DInSAR data and computes only one-dimensional surface deformation in the satellites LOS.

A more recent method that has been used in the scientific community is MSBAS. This technique is an extension of SBAS, however this method computes horizontal east-west and vertical deformation time series from multiple ascending and descending DInSAR data (Samsonov & D'Oreye, 2017). This is the main technique that I use in this study, and is further discussed in Chapter 1.5.2.

Time series analysis has been applied to a number of geophysical applications to analyze long-term ground deformation, including volcanic activity (Samsonov et al., 2017), CO_2 storage (Czarnogorska et al., 2014), urban development (Samsonov et al., 2014; Samsonov et al., 2016) and mining (Samsonov et al., 2013).

1.5.2 Multidimensional Small Baseline Subset

As aforementioned, the MSBAS technique computes two-dimensional deformation time series from overlapping, in time and space, ascending and descending DInSAR data

(Samsonov & D'Oreye, 2017). To overcome the limitations of classical DInSAR time series analysis methods (SBAS), MSBAS combines multiple DInSAR datasets into one, with improved characteristics including lower noise and higher temporal resolution. Both air-borne and space-borne data can be combined, integrating SAR data acquired with different sensor characteristics such as, azimuth, incidence angles, temporal and spatial resolution and sampling, wavelength and polarization (Samsonov & D'Oreye, 2012).

In the case of applying a single dataset, SBAS methodology can be applied (Berardino et al., 2002),

$$AV_{LOS} = \Phi_{obs} \qquad \text{(Equation 1-9)}$$

where matrix A is made up of time intervals between SAR acquisitions, V_{LOS} is a vector of unknown surface velocities, and Φ_{obs} is observed DInSAR data. This problem is overdetermined when: 1) the number of linearly independent equations, M^* equals the number of unknown velocities: $M^* = (N-1)$, where N is the number of SAR images and 2) the total number of equations (or number of interferograms) is greater than the number of unknown velocities: $M > (N-1)$. On the other hand, this problem is underdetermined when the number of unknowns is greater than the number of linearly independent equations $M < (N-1)$.

The above applies for the use of a single dataset for time series analysis, however if multiple, k datasets are used in the case of MSBAS Equation 1-9 becomes (Samsonov & D'Oreye, 2012),

$$\left| S_N^k A \; S_E^k A \; S_U^k A \right| \cdot \left| V_N V_E V_U \right|^T = \Phi_{obs}^k \qquad \text{(Equation 1-10)}$$

This assumes that V_{LOS} can be written as a sum of its components: $V_{LOS} = SV = S_N + S_E + S_U$ where S is a LOS vector with north, east and up components, S_N, S_E, S_U and V represents surface velocities.

Applying MSBAS method, the following equation can be derived from Equation 1-10 for a set of K sets of independent SAR data,

$$\begin{pmatrix} A^1 \\ A^2 \\ A^k \end{pmatrix} \begin{pmatrix} V_N \\ V_E \\ V_U \end{pmatrix} = \begin{pmatrix} \Phi^1 \\ \Phi^2 \\ \Phi^k \end{pmatrix} \quad \text{or} \quad \hat{A}\,\hat{V}_{LOS} = \hat{\Phi}_{obs} \qquad \text{(Equation 1-11)}$$

Due to the polar orbit of space-borne satellites, ground motion in the north-south direction is not well resolved, therefore northern motion terms in Equation 1-11 can be removed. This equation comprises of an undetermined set of linear equations and can be solved by applying SVD, which selects the minimum norm solution. This solution oscillates around the unknown, true solution which can be removed by applying another inversion technique, Tikhonov Regularization (Tikhonov & Arsenin, 1977). This regularized solution accounts for the problem due to rank deficiency and can be represented as

$$\begin{pmatrix} \hat{A} \\ \lambda L \end{pmatrix} \begin{pmatrix} V_E \\ V_U \end{pmatrix} = \begin{pmatrix} \hat{\Phi}_{obs} \\ 0 \end{pmatrix} \qquad \text{(Equation 1-12)}$$

where matrix $\hat{A} = \{S_E A, S_U A\}$ is composed of time intervals between successive SAR acquisitions A. θ represents azimuth, Φ incidence angle, V_E and V_U unknown surface velocities, $\hat{\Phi}_{obs}$ observed DInSAR data, λ is Tikhonov regularization parameter (which can be found using L-curve method (Hansen & O'Leary, 1993)) and L is a zero-, first- or second-order operator (Samsonov & D'Oreye, 2017).

Choice of regularization (zero-, first- or second-order) depends on the signal characteristics and the goal of the investigation. Zero order finds a solution using least squares fitting by minimizing the solution norm. This order is applied when the mean deformation rate is expected to be around zero (for example oscillating motion). First and second order regularization finds a solution using least square fitting and minimizing the first and second differences between successive deformation rates (Samsonov et al., 2017). First and second orders should be applied for steady mean deformation rates. The strength of each of these orders of regularization are controlled by the Tikhonov regularization parameter λ, where larger values of λ result in larger degrees of smoothing.

Explicit demonstration for a set of equations from Equation 1-12 can be found in Samsonov and D'Oreye (2017) for a simplified case of one ascending and one descending SAR dataset.

1.5.3   MSBAS Advantages and Limitations

MSBAS has four major advantages over standard DInSAR and time series techniques , 1) extended temporal coverage by combining data from different satellites to more accurately analyze long-term surface deformation, 2) increase in temporal resolution by combining data from multiple satellites giving a more dense sampling of ground deformation, 3) LOS deformation is decomposed into two-dimensional surface displacements, horizontal east-west and vertical components providing more detailed interpretation of ground motion and 4) sources of noise, mentioned in Chapter 1.4.4 such as atmospheric, topographic, thermal and orbital are averaged out during processing, increasing the signal-to-noise ratio (SNR).

However, some challenges still remain in DInSAR time series analysis. Atmospheric noise in particular is significant in regions of high topographic relief, for example volcanoes, which cannot be easily modeled for and removed (Samsonov et al., 2017). A better understanding of these errors are needed, despite work utilizing other remote sensing techniques to combat atmospheric errors (Bekaert et al., 2015). Residual orbital ramps similarly introduce noise that propagates through MSBAS processing, however with the improved location of modern satellite orbits (for example the Sentinel-1 satellite) this source of error is becoming less of an issue. Finally, it is important to note that deformation rates and time series of deformation are reconstructed by integration between successive acquisitions. Therefore, any error in velocity at a given time step, will propagate through to future time steps, so future time steps will be offset by the value of the error. However, given a problem with good rank and dense temporal and spatial coverage, the offset will converge to zero over time (Samsonov & D'Oreye, 2012).

Chapter 2

2 Study Area

2.1 Induced Seismicity at Timpson, TX

On Thursday 17th May 2012, a M$_w$4.8 earthquake occurred 4 km northeast of the city of Timpson, TX. This event was the largest earthquake in the historical record for eastern Texas (Frohlich et al., 2014) and was felt as far away as Nacogdoches, 50 km southwest of Timpson and in the nearby town of Garrison.
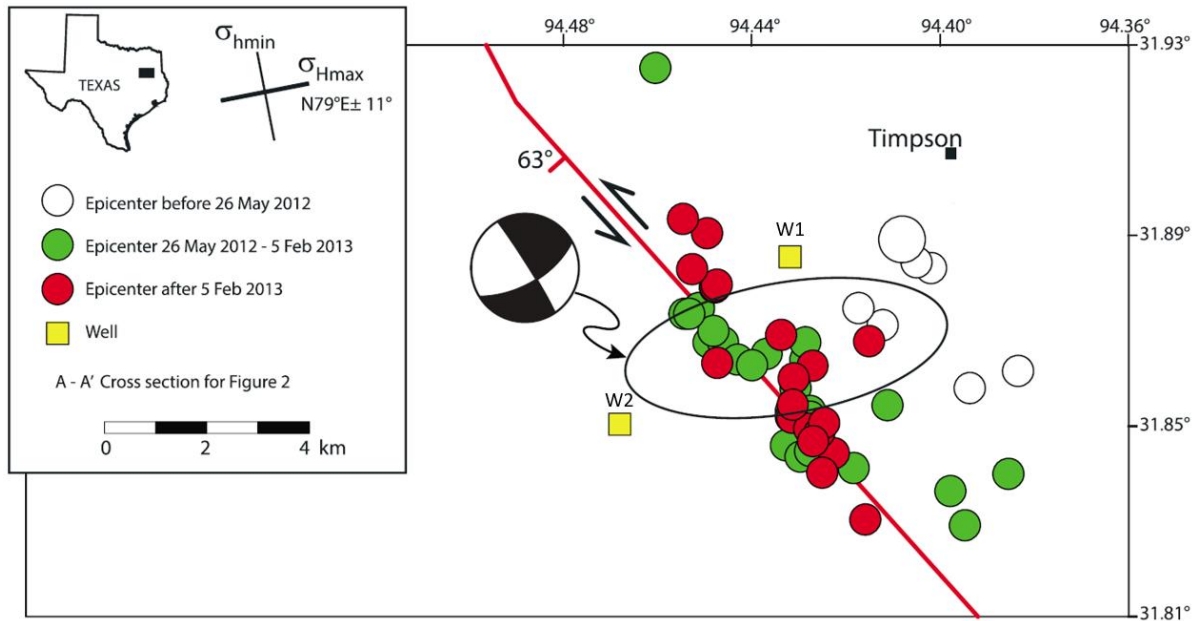
Figure 2-1 Map of seismicity (circles), major injection wells (yellow squares) and moment tensor solution for the M$_w$4.8 event near Timpson, TX, which likely occurred within the elliptical region defined by the Mercalli Intensity VII region. White circles represent events before 26th May 2012, when the first temporary seismic stations were deployed. Green circles represent epicenters of events occurring between 26th May 2012 and 5th February 2013. Red circles represent the most reliable epicenter locations after 5th February 2013. Modified after Frohlich et al. (2014).

Prior to the events mentioned above, seismicity was scarce in this region (Frohlich et al., 2014). The only previous events near this study region were in January 1981, Rusk, TX

where a M 4.0 occurred 80 km west of the epicentral area, and M 3.0 in June 1981, Center, TX, 25 km southeast of Timpson, as discussed in Frohlich and Davis (2002). However, due to the unreliability of the seismic stations at this time, there are uncertainties over the accuracy of these reported events.

One week prior to the main event, a M_w4.0 foreshock was recorded 10 km northwest of Timpson on 10th May 2012. This sequence of events included aftershocks on 25th January 2013 (M_w 4.1) and 2nd September 2013 (M_w 4.1 and M_w 4.3) (Frohlich et al., 2014) in the region. As of August 2017, no further seismic activity has been recorded in this region since September 2013.

Figure 2-1 shows seismicity in the region of Timpson; prior to 26th May 2012 (before temporary seismometers were installed), between 26th May 2012 and 5th February 2013, and relocated events after this date. The clustering of this seismicity can be seen to trend along a mapped basement fault in the region, trending NW-SE. Figure 2-1 also shows the *beach ball*, or more accurately, global centroid moment tensor for the M_w 4.8 event indicating predominantly a strike slip mechanism, reported by the Columbia group (Ekström et al., 2012). Focal depths for these events are shallow, between 1.6 and 5 km depth, with the majority of strain released on average at a depth of 3.5 to 5 km depth (Frohlich et al., 2014).

Seismicity at Timpson and its relationship to wastewater injection wells is presented in Figure 2-2. Two high-rate injection wells, W1 and W2 (discussed in Chapter 2.2), are located within ~4 km of the 2012 M_w 4.8 event, and even closer to other seismicity in the region. The following section will describe the wastewater injection wells investigated in this study.

2.2   Wastewater Disposal Activities

The Railroad Commission of Texas (RRC) regulates wastewater injection wells in Texas through its Oil and Gas Division. The RRC no longer monitors railroads in Texas, but regulates well injection activities, production, exploration and transportation of oil and gas within the state. The RRC has a vast collection of well data, provided by the well

operators for the past two decades including fluid injection information such as, volumes of water and gas extracted or injected, all of which is free to access online.

In eastern Texas, vast oil and gas reservoirs have been exploited since 1901 and Texas is the US' leading oil- and natural gas-producing state, holding more than 25% of the US proven natural gas reserves and 1/3 of the nation's crude oil reserves (The Academy of Medicine Engineering and Science of Texas, 2017). There are also more than 10,000 injection wells in Texas that have been active since 2000, all of which are regulated by the RRC (Frohlich et al., 2014).

There are four high volume class II wastewater injection wells located within ~15 km from the seismicity at Timpson. Two of these high-volume disposal wells lay directly above the earthquake hypocenters, labelled in Figure 2-1 and Figure 2-2B (W1 and W2). The other two high-volume wells (E1 and E2) are located ~15 km east of Timpson are also shown in Figure 2-2B.

Figure 2-2 shows the spatial relationship between seismicity Figure 2-2A and well injection sites in the region Figure 2-2B. In addition to the four major wastewater injection wells in the region, there are 19 other class II wells within 15 km of Timpson shown in Figure 2-2B. These 19 injection wells inject considerably less wastewater into the subsurface compared to the four major injection wells, W1, W2, E1 and E2, as highlighted in Figure 2-4, but lie proximal to the seismicity in Timpson. In Figure 2-2B, wells are coloured based on their distance from the four major injection wells and each are labelled with their API number. All of the wells in this study area dispose coproduced salt formation water, typically the waste product of hydraulic fracturing operations, into geologically confined underground formations (Railroad Commission of Texas, 2015).
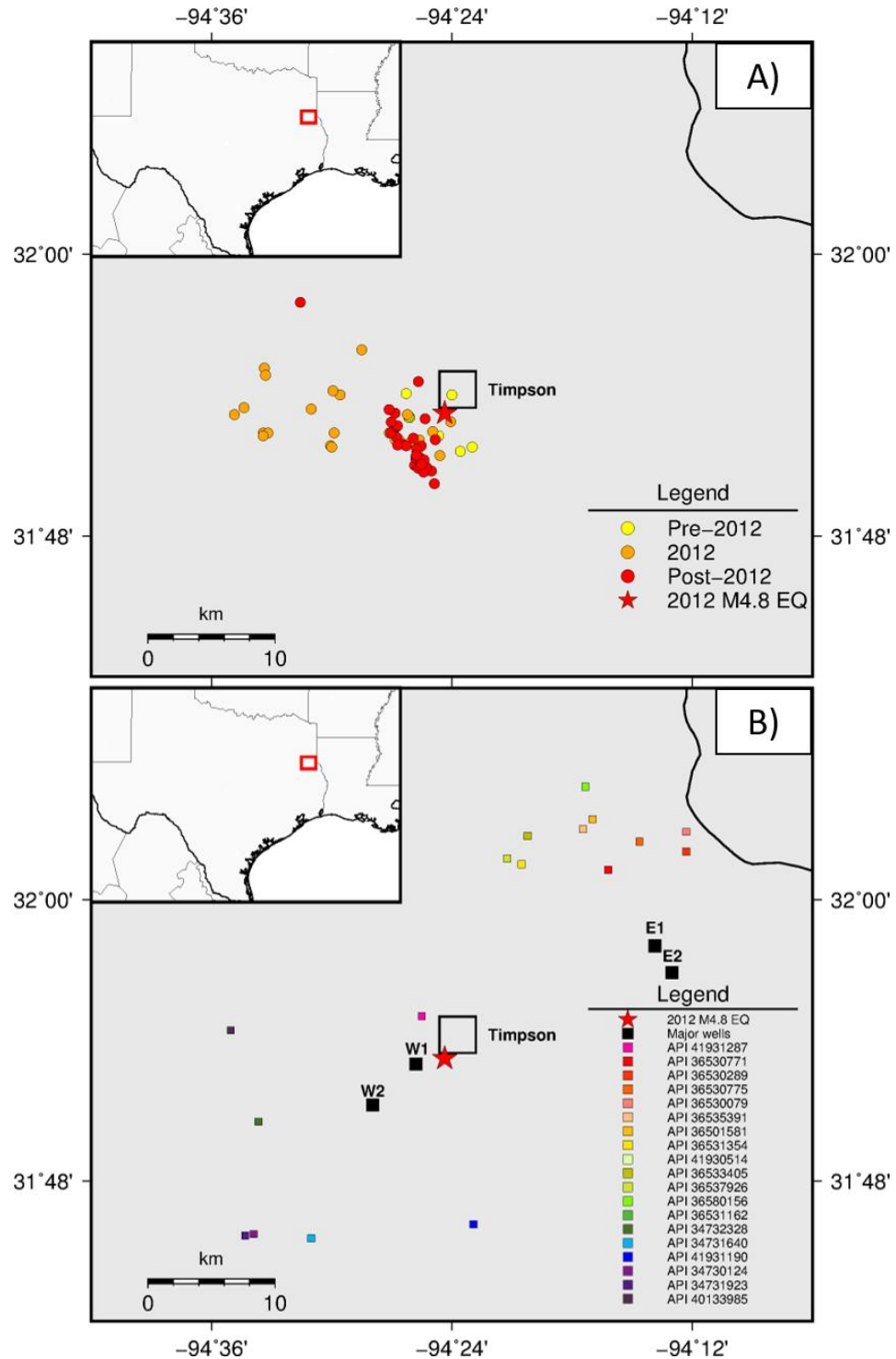
Figure 2-2 A) Timpson seismicity (circles) plotted as a function of time, pre-2012, 2012 and post-2012, including the 2012 $M_w4.8$ earthquake (red star) and **B)** major disposal wells (black squares) and minor disposal wells (coloured squares) included in this study surrounding the city of Timpson (black outline).

Table 2-1 highlights the major parameters from the RRC for the four major injection wells in the region, E1, E2, W1 and W2. To this date, the total injected volumes for the two west wells W1 and W2, were 1.27 million m^3 and 2.78 million m^3 respectively. The eastern wells have injected similar volumes, 1.53 million m^3 and 2.5 million m^3 for E1 and E2 wells respectively. Injection rates for the past 20 years are shown for these four wells in Figure 2-3. Figure 2-3 shows that the two western wells, W1 and W2 have recently ceased injecting into the subsurface, W2 since late 2014 and W1 since late 2016, whereas the two eastern wells, E1 and E2 have remained injecting large volumes of fluid into the subsurface.

API	Well Label	Lat (°)	Lon (°)	Max Liquid Injection Volume (BBLs/day)	Max Liquid Injection Pressure (PSI)	H-10 Status
41931083	W1	31.883	-94.430	10000	2790	Active
40133833	W2	31.854	-94.465	15000	3025	Tmp. Abn
41930914	E1	31.967	-94.231	6000	1410	Active
41930818	E2	31.948	-94.217	6000	1410	Active

Table 2-1 Major waste disposal wells located within the study area. Table includes well identification number (API), well label (W1, W2, E1, E2), location (latitude and longitude), max liquid injection volume and pressure, average injection depth and current H-10 well-status (Tmp. Abn = Temporarily Abandoned). Data collected from Railroad Commission of Texas, (2015).
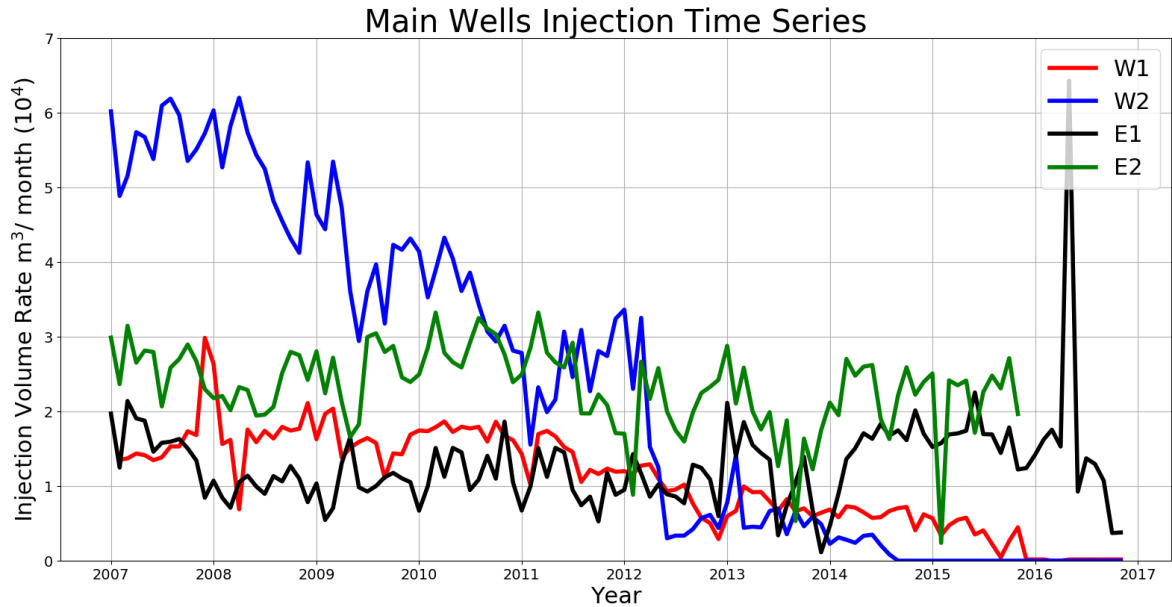
Figure 2-3 Injection volume rates for four major injection wells (W1, W2, E1 and E2) over a 10-year period. Data collected from Railroad Commission of Texas (2015).

Depths of fluid injection also are provided by the RRC and are shown in Table 2-2 for each well used in this study. Data is shown for the entire RRC catalogue ranging twenty years from 2007 to 2017, and collected from H-10 reports that each operator must file each year. The top and bottom depths of the fluid injection interval are presented in Table 2-2. The injection depths for each well do not vary greatly through time, with the majority of the wells injecting at a consistent depth throughout the wells lifetime.

For the main wells, it is important to note that the west wells (W1 and W2) inject around 1900-2000 m deep into the Rodessa of the Trinity Formation (Chapter 2.3). However, the eastern wells (E1 and E2) inject into a shallower carbonate formation of the Washita Group at around 900m depth. The geological units which these wells inject fluid into, the Rodessa and Washita Group, are discussed further in Chapter 2.3.

		Top – Bottom Injection Depths (m)										
API	**Well Label**	**2007**	**2008**	**2009**	**2010**	**2011**	**2012**	**2013**	**2014**	**2015**	**2016**	**2017**
41931083	W1		1889-1981	1889-1981	1889-1981	1889-1981	1889-1981	1889-1917	1889-1981	1889-1981	1798-1825	
40133833	W2	1844-1871	1844-1871	1844-1871	1844-1871	1844-1871	1853-1868	1844-1871	1844-1871	1844-1871	1844-1871	
41930914	E1		859-883	859-883	859-883	859-883	859-883	859-883	859-883	859-883	859-883	
41930818	E2		875-910	875-910	875-910	875-910	859-911	859-911	859-911	859-911	859-911	
36530771		1584-1617	1584-1617	1584-1617	1584-1617	1584-1617	1584-1617	1584-1645	1600-1617	1600-1617	1600-1617	1600-1617
36530775		1539-2072	1539-2072	1539-2072	1539-2072	1539-2072	1539-2072	1539-2072	1539-2072	1539-2072	1539-2072	1539-2072
36530289		798-810	798-810	798-810	798-810	798-810	798-810	798-810	798-810	798-810	798-810	
36530079			809-811	788-811	788-811	788-811	788-811	788-811	788-811	788-811	788-811	
36535391		1825-1842	1825-1842	1825-1842	1825-1842	1825-1842	1825-1842	1825-1842	1825-1842	1825-1842	1825-1842	
36580156		1543-1552	1543-1552	1543-1552	1493-1584	1493-1584	1493-1584	1493-1584	1493-1584	1493-1584	1493-1584	
36501581		1804-1819	1804-1819	1804-1819	1804-1819	1804-1819	1804-1819	1804-1819	1804-1819	1804-1819	1804-1819	
36533405			1582-1585	1582-1585	1582-1585	1582-1585	1582-1585	1582-1585	1582-1585	1582-1585	1582-1585	
36531354							1860-1894	1860-1894	1860-1894	1860-1894	1860-1894	
36537926								1871-1901	1871-1901	1871-1901	1871-1901	1871-1901
41930514			1554-1584	1554-1584	1554-1584	1554-1584	1554-1584	1554-1584	1554-1584			
36531162							1537-1559	1537-1559	1537-1559	1537-1559	1537-1559	
41931287				1780-1793	1780-1793	1780-1793	1780-1793	1780-1793	1780-1793			
40133985				1900-1932	1900-1932	1900-1932	1900-1932	1900-1932	1900-1932	1900-1932	1900-1932	
34732328		1984-2051	2031-2051	1252-1271	1252-1271	1252-1271	1252-1271	1252-1271	1252-1271	1252-1271	1252-1271	1252-1271
34731923				2087-2104	2087-2104	2087-2104	2087-2104	2087-2104	2087-2104	2087-2104	2087-2104	
34730124			2078-2097	2078-2097	2078-2097	2078-2097	2078-2097	2078-2097	2078-2097	2078-2097	2078-2097	
34731640			1235-1305	1235-1305	1235-1305	1235-1305	1235-1305	1235-1305	1235-1305	1235-1305	1235-1305	
41931190			1214-1219	1214-1219	1214-1219	1214-1219	1214-1219	1214-1219	1214-1219	1214-1219	1214-1219	

Table 2-2 Fluid injection depths for each well investigated in this study. Well APIs represent each well, the location of which can be seen in Figure 2-2. The main injection wells W1, W2, E1 and E2 are also labelled. Depth units in meters for the top and bottom intervals of fluid injection.

The 19 other class II injection wells surrounding the location of the Timpson earthquakes inject considerably smaller volumes of injected fluid compared to the four major wells in this study (W1, W2, E1 and E2). Table 2-3 shows a summary of the 19 class II injection wells within 15 km of the four major injection wells, whereby the API number corresponds with the location of each well in Figure 2-2 B. The injection rates per month for these minor wells over the last two decades are considerably less than the major injectors (Figure 2-4). However, two wells, API3650771 and API3650079, have injected significantly larger volumes (2 million m^3) than the other wells.

API	Lat (°)	Lon (°)	Max Liquid Injection Volume (BBLs/day)	Max Liquid Injection Pressure (PSI)	Total Injected Volume to Date (million m³)	H-10 Status
36530771	32.021	-94.270	10000	2600	2.04	Active
36530775	32.041	-94.244	6000	2525	0.13	Active
36530289	32.034	-94.205	2500	1310	0.36	Active
36530079	32.048	-94.205	5000	1275	0.62	Active
36535391	32.050	-94.291	25000	2500	2.05	Active
36580156	32.080	-94.289	3000	1600	0.94	Active
36501581	32.057	-94.283	3500	1400	0.47	Active
36533405	32.045	-94.337	3000	1700	0.09	Active
36531354	32.025	-94.342	4000	2000	0.15	Active
36537926	32.029	-94.354	5000	1000	0.15	Active
41930514	31.937	-94.080	7500	2550	1.05	Temp. Abn
36531162	32.016	-94.087	8000	2520	0.92	Active
41931287	31.917	-94.425	15000	2850	0.43	Temp. Abn
40133985	31.907	-94.584	4000	3000	0.24	Active
34732328	31.842	-94.561	8000	2000	0.66	Active
34731923	31.761	-94.572	10000	3300	0.58	Active
34730124	31.762	-94.565	10000	2250	0.77	Active
34731640	31.759	-94.517	10000	2026	0.61	Active
41931190	31.769	-94.382	10000	1800	1.25	Active

Table 2-3 Waste disposal wells located within 15 km of the four main injection wells, including well identification number (API), location (latitude and longitude), maximum liquid injection volume and pressure, average injection depth, total injected volume (Jan-07 to Jan-17) and current H-10 well-status (Tmp. Abn = Temporarily Abandoned). Data collected from Railroad Commission of Texas (2015).
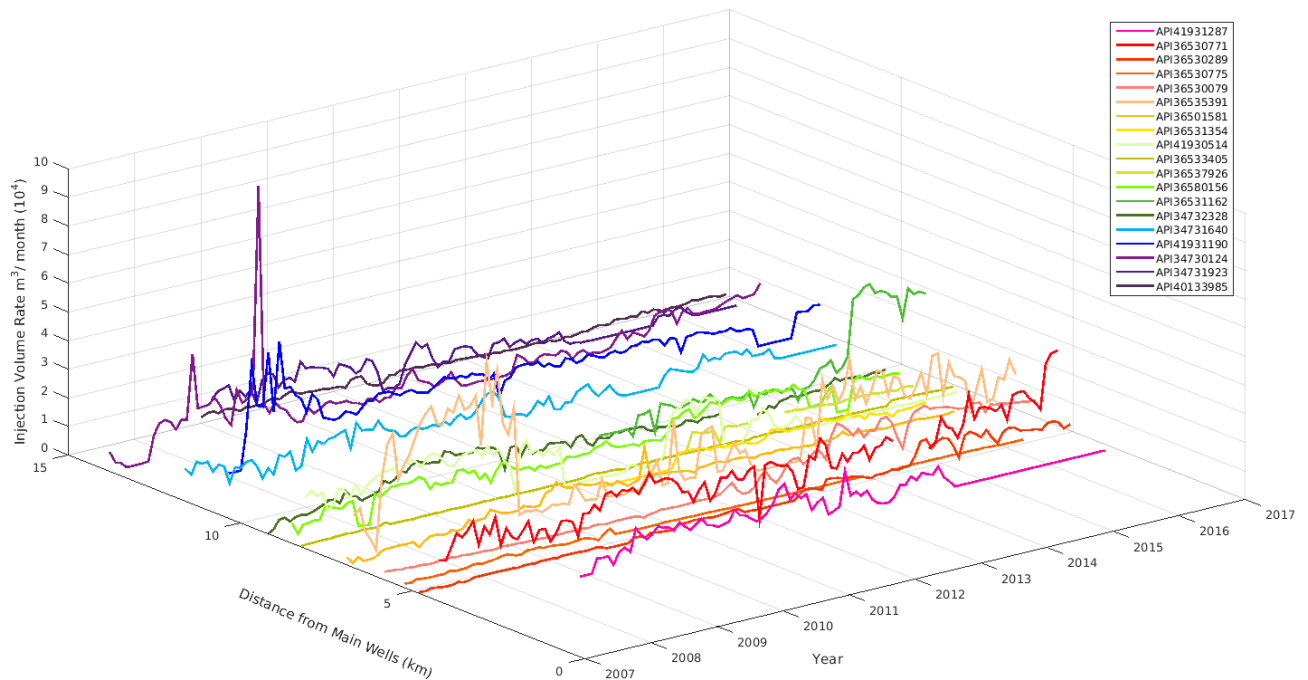
Figure 2-4 Injection volume rate for 19 waste disposal wells located within 15 km of the four main injection wells. Data is plotted over a 10-year period and coloured as a function of distance from the main wells. Colours correspond to their location shown in Figure 2-2. Injection volume data collected from Railroad Commission of Texas (2015).

2.3   Geology

2.3.1   Geological Setting

Timpson is located within the East Texas hydrocarbon basin, a basin known for its abundance of salt diapirs (The Academy of Medicine Engineering and Science of Texas, 2017). These mobile structures are important for trapping rich reserves of hydrocarbons and is a component in most oil and gas plays in eastern Texas. Regional tectonics in eastern Texas also indicate an east-west trending fault system of Cretaceous-Paleogene age, the Mt. Enterprise fault zone northwest of Timpson (Frohlich et al., 2014).

Another major fault is mapped in the region by Jackson (1982) on a map of the Paleozoic basement, but he does not identify this at any shallower depths. This fault can be seen in Figure 2-1 and seismicity in the region follows the trend of this fault. However, further research is needed in order to accurately locate this fault at depth.

The underlying stratigraphy at Timpson can be seen in the cross section in Figure 2-5. The eastward upward dip corresponds to a structural feature known as the Sabine Uplift, a basement fault block that originated as a mid-rift high during rifting in the Triassic (Adams, 2009). The crystalline basement is located at a depth of 4 km and it is around this depth that it was found that the seismicity at Timpson occurred, corresponding with the location of the aforementioned basement faults (Fan et al., 2016).
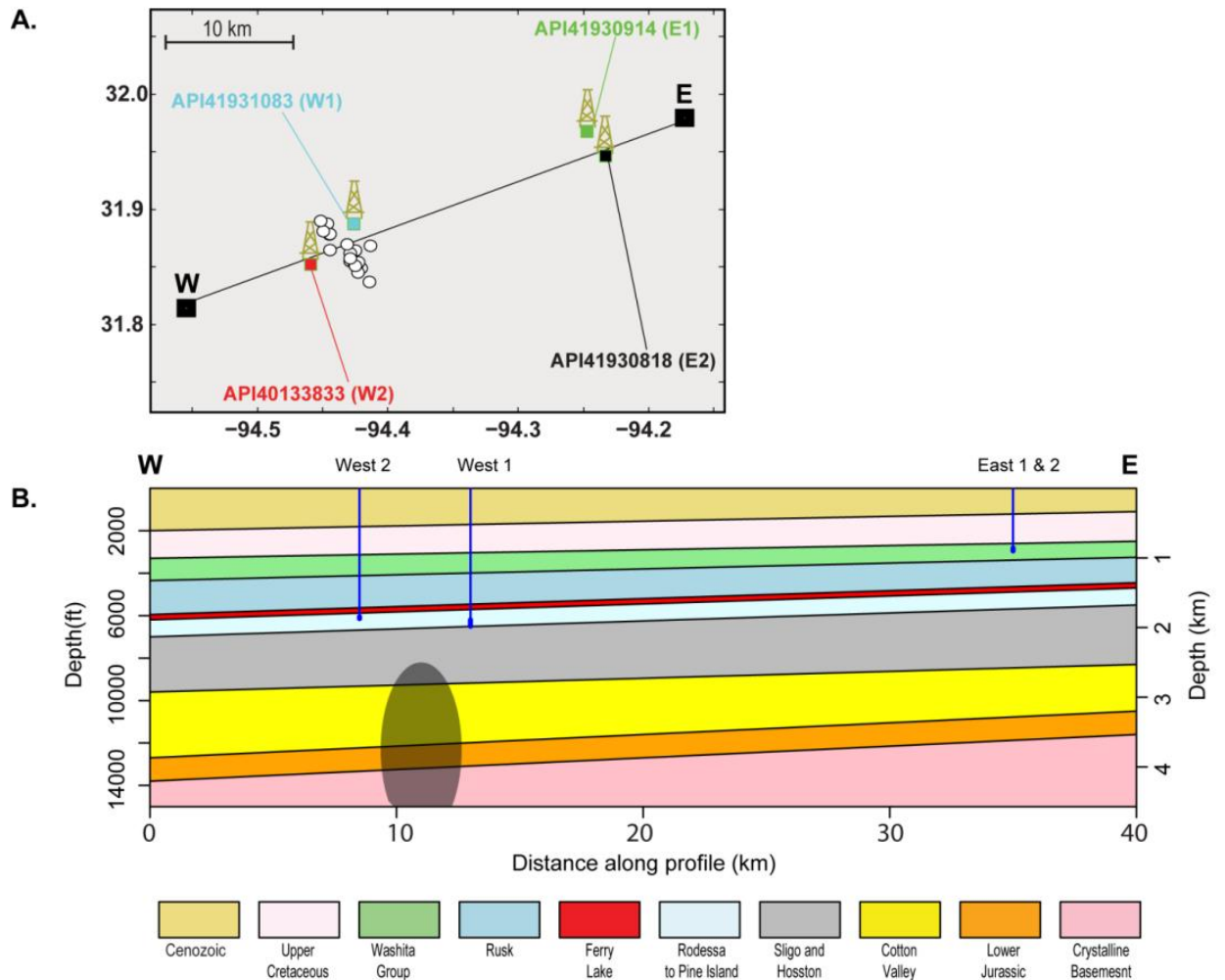
Figure 2-5 A) Map view of geological east-west profile across region of seismicity (white circles) between four major injection wells **B)** Geologic profile with formation names and shaded region showing depth of seismicity, from Shirzaei et al. (2016).

From Figure 2-5 and Table 2-2, the west wells both inject into the Rodessa Formation, a thick, porous limestone that is favorable to store large volumes of injected fluid. The

thickness of this limestone unit ranges between 90 and 150 meters across the study region and lies at a depth of 1.8 km (Granata, 1963). This limestone unit was deposited during the Lower Cretaceous period on a broad, restricted shallow marine platform that has undergone significant micritization, cementation, dissolution and compaction (Triyana, 2003). Conformably overlaying the Rodessa Formation is the Ferry Lake Anhydrite, a Lower Cretaceous unit of alternating carbonate and evaporate beds. The Ferry Lake was deposited on a restricted shallow marine shelf that had limited connection to the open ocean due to an extensive barrier reef located on the edge of the carbonate shelf (USGS, 1794). Although this salt layer is thin in this region (up to 15m in thickness), it is regionally extensive and is much less permeable than the underlying Rodessa limestone (Granata, 1963). Therefore, this salt unit acts as a regional seal for the upward migration of fluid within the Rodessa.

Similarly, from Figure 2-5 and Table 2-2, the eastern wells inject at a shallower depth into the Washita Group, which is located at a depth of 0.9 km. Stratigraphically, this unit is above the Ferry Lake Anhydrite. The Washita Group was deposited towards the end of the Lower Cretaceous period and is composed of alternating thick clay and limestone units. Where the Washita Group is completely preserved, it thickens in an easterly direction up to a thickness of 270m (Granata, 1963).

2.3.2   Well Logs

In addition to well injection data and findings from previous studies on the geology of the region, well logs were available for three wells used in this investigation. Well logs for the major injection well, W2 and two other injection wells, API34731923 and API40133985 are presented in Figure 2-6 and Figure 2-7. These logs were obtained from the Railroad Commission of Texas (2015) and provide more information on the geologic units into which the wastewater is pumped, such as the porosity and thickness of the units. A well log or wireline log measures the petrophysical properties of rocks in the subsurface using various techniques such as resistivity, spontaneous potential (SP), gamma ray (GR), density porosity, neutron porosity and sonic measurements. Using a combination of these techniques, well logs can be interpreted to provide information on the lithology of the subsurface (Schlumberger, 2017).
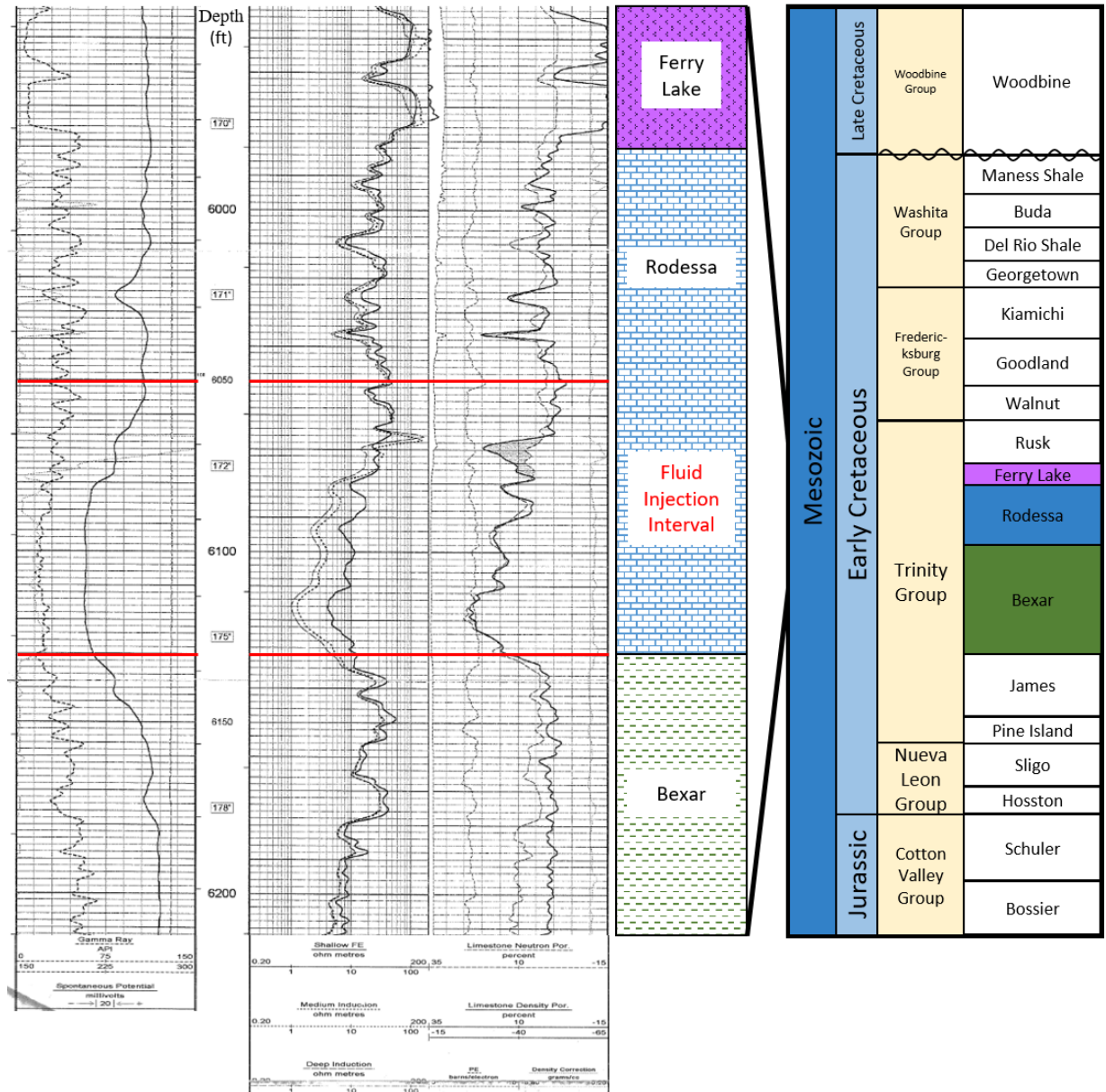
Figure 2-6 Well log for well W2 (API40133833), lithology and stratigraphic column. The major units investigated in this study, Ferry Lake and Rodessa are highlighted, along with interval of fluid injection. Well log depth measured in feet. Well log was obtained from Railroad Commission of Texas (2015) and stratigraphic column adapted from Granata (1963).

Figure 2-6 shows the well log obtained from well W2, including a lithology and stratigraphic column. This well log was performed at Naconiche Creek Field within Nacogdoches County in July 2004, prior to the injection of wastewater. This well log provides further information and constraints on subsurface properties, such as the porosity and permeability of the target reservoir unit, in this case the Rodessa Limestone Formation. The lithology column was interpreted based on the characteristics of the wireline logs. The stratigraphic column describes the time period when each geologic unit was deposited.

As previously discussed, the Rodessa Formation is predominantly composed of a porous, fragmented crystalline limestone, interbedded with dark gray shales (Granata, 1963). It is distinctive on the well log from the underlying unit, the Bexar Shale and the overlying Ferry Lake Anhydrite. Due to the high porosity of this unit, we can identify this unit using a number of attributes of the well log.

First, neutron measurements provide an indication of a formation's porosity based on the number of hydrogen molecules present. The density log however measures the porosity of a formation based on the assumed density of the formation and drill fluid in gram per cubic centimeter (g/cm^3) (Evenick, 2008). Using these two pieces of information on a well log, the type and porosity of the formation can be interpreted. For example, limestone typically shows little to no separation of the density and neutron porosity logs, if plotted on a limestone scale (AAPG, 2016). The Rodessa Limestone in Figure 2-6 also shows this characteristic; the density and neutron porosity overlay each other and show high porosity values between 15 to 25% at the most porous section of the formation.

Second, a GR log records the natural radioactivity of a formation in API (American Petroleum Institute) units, where shale units have high (75-200) API values and sandstone or limestones have low (10-40) API values (Evenick, 2008). Figure 2-6 shows that the lower section of the interpreted limestone unit has a GR reading around 15 API. At the top of the Rodessa Formation (5980ft – 6080ft), GR readings increase, suggesting an influx of shale or mud.

Third, photoelectric absorption (PE) measures gamma radiation emitted from a formation after being bombarded by photos. This radiation depends on the mineralogy of the formation therefore is a good indicator of lithology (Evenick, 2008). The Rodessa Limestone in Figure 2-6 shows a consistent PE reading of 5 barns/electron, a typical response for a limestone unit (Evenick, 2008). Towards the top of the Rodessa Formation, the increase in shale reduces the PE towards readings of 4 barns/electron.

Finally, the resistivity segment of the well log measures the resistivity, or resistance to the flow of electricity through the formation, indicating the porosity and type of fluid present within the rock. Porous or hydrocarbon rich rocks have high-resistivity, whereas non-porous (tight) or saltwater (brine) filled formations have low resistivity. In the Rodessa Limestone, although resistivity (deep induction) is low, this indicates a porous formation saturated with brine.

In Figure 2-6 in the stratigraphic column, the Ferry Lake Anhydrite overlies the Rodessa Limestone. The contact between these two units at well W2 can be seen in the well log around 5980ft depth. This contact is visible due to the distinct differences in well log measurements between anhydrite and limestone. Compared to the Rodessa Limestone, the Ferry Lake Anhydrite has lower gamma readings (<15 API), very high resistivity (>200 Ωm) and very large neutron – density separation, indicative of anhydrite.

Figure 2-6 also presents the interval of fluid injection at the depths indicated in Table 2-2, from the official H-10 well status reports. This zone, ~90 ft. thick, corresponds with the most porous limestone section of the Rodessa Formation based on the evidence mentioned above.
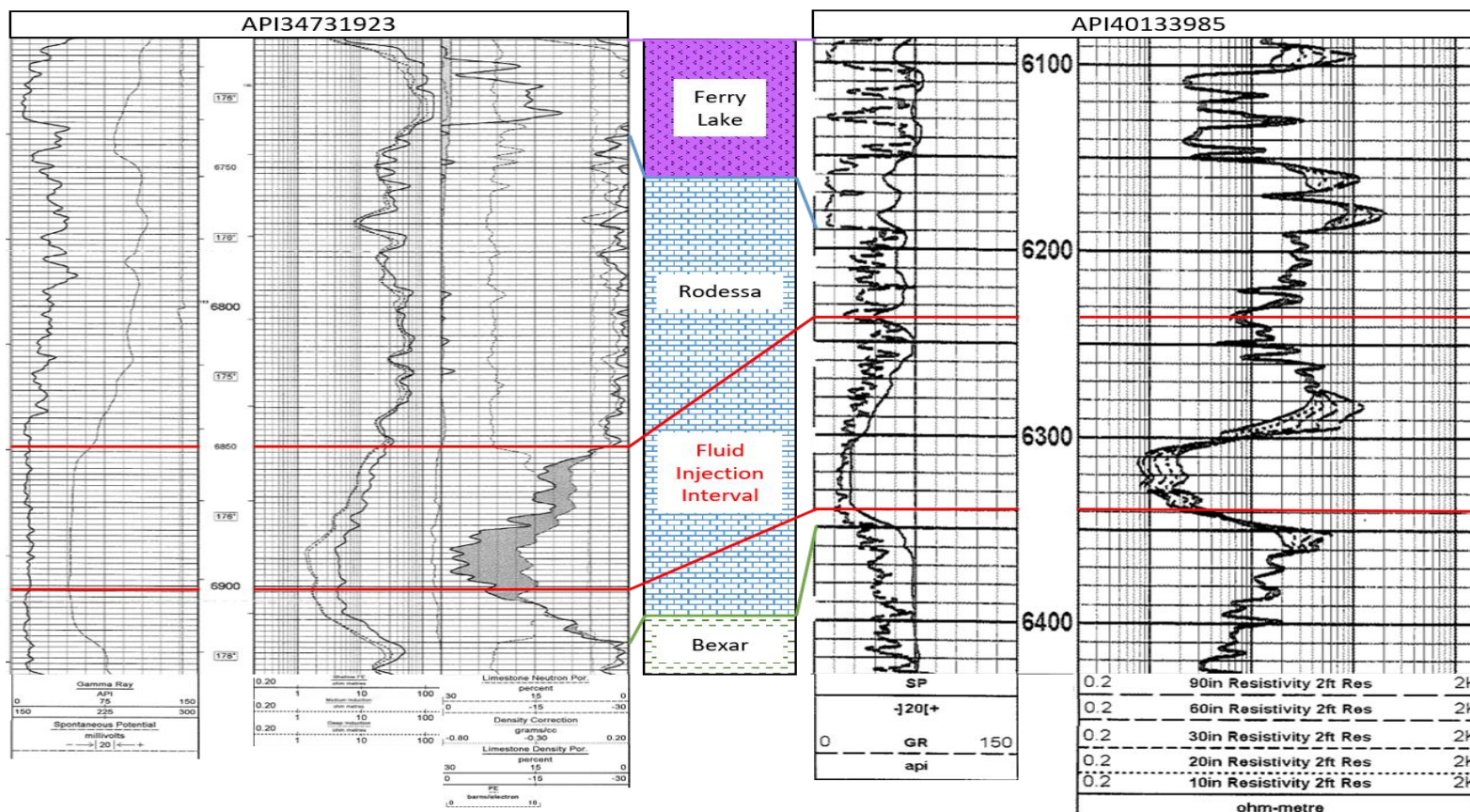
Figure 2-7 Well logs for wells API34731923 and API40133985 and corresponding lithology column. Location of wells can be seen in Figure 2-2 B). The major units investigated in this study, Rodessa Limestone and Ferry Lake Anhydrite are highlighted across the well logs, along with interval of fluid injection. Well log depth measured in feet. Well log was obtained from Railroad Commission of Texas (2015).

Two additional well logs were acquired in the study region, API34731923 and API40133985, shown in Figure 2-7. These two wells are located west of Timpson, 16 km apart and provide further information on the lithology and petrophysical properties of the reservoirs that wastewater is being injected into to the west of our study area. Similar to Figure 2-6, a lithology profile was constructed based on the well log characteristics and formation tops are highlighted between the three major units in this region, Bexar, Rodessa and Ferry Lake Formations. Although only GR and resistivity measurements are provided for well API40133985, formation tops can still be identified due to the distinctive difference in GR and resistivity characteristics between formations.

There is a strong similarity between well log characteristics of the Rodessa Limestone at well W2 and those presented in Figure 2-7. In all three wells, the Rodessa shows a similar region of low GR values, lower resistivity and PE value of 5 barns/electron. Similarly, where these characteristics vary from that typical of a limestone, we can assume an increase in shales and muds, particularly in the upper Rodessa. This shows that the Rodessa reservoir remains consistent across our study area, with no major lateral changes in petrophysical properties.

However, in the lower Rodessa in API34731923, the neutron-density logs present an outstanding feature (6850 – 6900ft.). This shaded region is commonly identified in hydrocarbon exploration as a gas-saturated zone. The neutron log underestimates porosity and is significantly lower than the density log which overestimates the porosity of a gas-filled formation because the measured bulk density is lower (Evenick, 2008). This effect indicates a ~90ft thick, gas-saturated zone and was the target for gas production in this region. H-10 disposal well reports confirm that wastewater was disposed into a productive zone, within this Rodessa Limestone formation.

Chapter 3

3 Methods

This chapter discusses the DInSAR dataset used in this investigation at Timpson, the processing steps for generating differential interferograms and analysis of the MSBAS algorithm.

3.1 DInSAR Data

In this investigation, I collected data from four different satellites, ALOS (Advanced Land Observing Satellite), ALOS-2, RADARSAT-2 and Sentinel-1A. ALOS, ALOS-2 and Sentinel data were requested and downloaded from the Alaskan Satellite Facility portal (available from https://vertex.daac.asf.alaska.edu/) (ASF, 2017), whereas RADARSAT-2 images were provided by the Canadian Space Agency (CSA) under a SOAR Education proposal (soareduc-5226).

An analysis of each satellite used in this study is described in Chapters 3.1.1 to 3.1.3 and a comparison of these satellites are shown in Table 3-1. For each satellite, the characteristics of each sensor vary, as well as the type of beam mode used to acquire an image of the Earth. RADARSAT-2 and Sentinel-1A acquire images with a C-band sensor, which operates at 5.6 cm wavelength. However, ALOS and ALOS-2 acquire data with an L-band sensor, operating at 24 cm wavelengths. This difference in wavelength is an important factor in DInSAR analysis. Shorter wavelengths (such as C-band) are more sensitive to surface deformation than longer wavelengths (Zink, 2003), thus C-band is preferred in DInSAR to detect small ground motions. However, in vegetated regions, shorter wavelengths are unable to penetrate through vegetation, causing decorrelation over long temporal baselines. Whereas longer wavelengths (such as L-band) tend to have some penetration of vegetation and are less sensitive to small changes in surface conditions over time. Therefore, ALOS L-band sensor is able to remain coherent with large orbital repeat cycles of 46 days, in highly vegetated regions.

InSAR dataset	Acquisition Beam Mode	Orbital Repeat Cycle (days)	Sensor Wavelength (cm)	Nominal Pixel Resolution: ground range x azimuth (m)
RADARSAT-2	Wide	24	5.6 (C-band)	13.5 x 7.7
Sentinel-1A	Interferometric Wide Swath (IW)	12	5.6 (C-band)	5 x 20
ALOS	Fine Beam Single (FBS)	46	24 (L-band)	FBS: 10 x 5
	Fine Beam Double (FBD)			FBD: 20 x 5
ALOS 2	Fine Beam Double (FBD)	14	24 (L-band)	FBD: 9.1 x 5.3

Table 3-1 Comparison of four satellites used in this study, RADARSAT-2, Sentinel-1A, ALOS and ALOS 2.

Frames were selected over the study area based on their spatial and temporal coverage, as shown in Figure 3-1, along with the location of the M_w4.8 Timpson event and wastewater disposal wells. Spatial coverage for each sensor varies over the study area, with some frames (ALOS), only covering approximately half the region of interest, whereas other (Sentinel-1 and RADARSAT-2) cover the entire area.
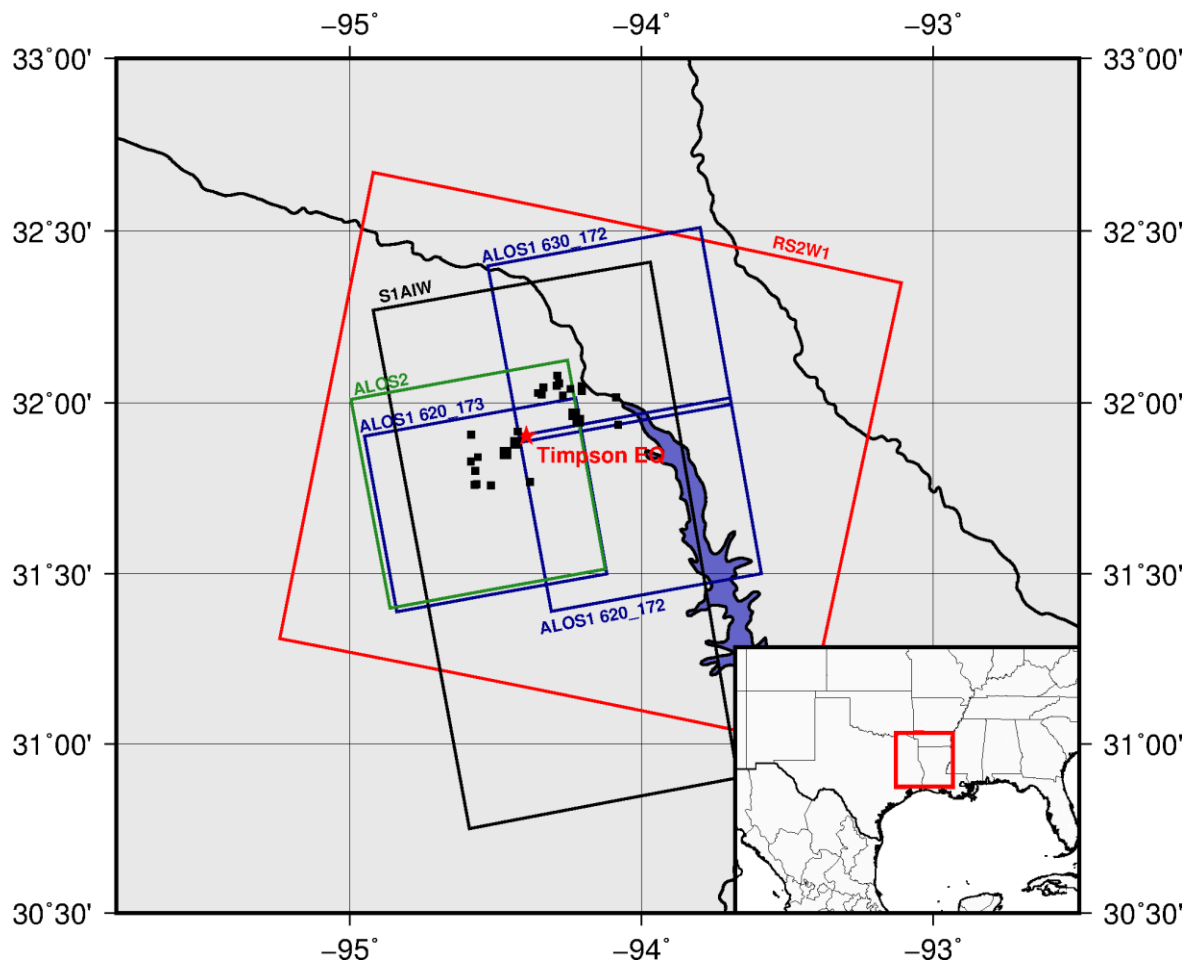
Figure 3-1 Footprints of satellite images used in this study (red: RADARSAT-2, blue: ALOS, green: ALOS-2 and black: Sentinel-1A). Major and minor injection wells are shown (black squares), as well as location of M4.8 2012 Timpson earthquake (red star).

The temporal coverage and sensor characteristics of each dataset is shown in Table 3-2. RADARSAT-2 is the only *descending* satellite used in this investigation. A descending satellite travels in an orbit from north towards the south. However, the other satellites in this study orbit from south to north, therefore in an *ascending* orbit. From Table 3-2, each satellite covers a different time period, each with different number of images acquired over this period.

DInSAR dataset	Temporal Coverage	Orbit	θ (•)	φ (•)	N	M
RS2-W1	20140306 - 20170314	dsc	-168	26	29	407
S1A-IW	20161004 - 20170520	asc	-13	39	19	138
ALOS1 620_173	20070621 - 20101114	asc	-10	39	14	89
ALOS1 630_172	20070506 - 20101114	asc	-10	39	19	181
ALOS1 620_172	20070708 - 20101201	asc	-10	39	16	118
ALOS-2	20141002 - 20160929	asc	-10	36	3	3

Table 3-2 DInSAR dataset collected over Timpson from this study, RADARSAT-2 (RS2-W1), Sentinel-1A (S1A-IW), three ALOS frames (ALOS1) and ALOS-2. Temporal coverage in the format YYYYMMDD, ascending (asc) or descending (dsc) orbit, azimuth angle (θ), incidence angle (Φ), number of images (N) and number of interferograms (M).

A detailed breakdown of the acquisition date for each dataset is shown in Table 3-3. In total, 29 descending RADARSAT-2 Wide-1 (RS2-W1) images were acquired, 19 ascending Sentinel-1A Interferometric Wide (S1A-IW), 14 ALOS1 620_173, 19 ALOS1 630_172, 16 ALOS1 620_172 and 3 ALOS-2. Highlighted in bold and red in Table 3-3 are the images chosen as the master images for DInSAR processing. Master images were chosen that minimized the perpendicular baseline for each interferometric pair. Once a master is chosen for each dataset, the perpendicular baseline can be calculated for each interferogram. These perpendicular baselines can be represented on a baseline plot, showing the temporal vs spatial perpendicular baselines (Figure 3-2). Details on the acquisition modes and characteristics for each of these satellites is described in the following sections (Chapters 3.1.1 to 3.1.3).

RS2-W1	S1A-IW	ALOS1 620_173	ALOS1 630_172	ALOS1 620_172	ALOS-2
20140306	20161004	20070708	***20070506***	20070506	20141002
20140330	20161016	20071008	20070621	20070621	***20151001***
20140423	20161028	20080108	20070921	20070921	20160929
20140517	20161109	20080525	20071222	***20071222***	
20140610	20161121	20080710	20080206	20080508	
20140704	***20161203***	20091013	20080323	20080623	
20140728	20161215	20100113	20080508	20090626	
20140821	20161227	20100415	20080623	20091227	
20150512	20170108	***20100531***	20090208	20100211	
20150629	20170120	20100716	20091227	20100329	
20150723	20170201	20100831	20100211	20100514	
20150816	20170225	20101016	20100329	20100629	
20150909	20170309	20101201	20100514	20100929	
20151003	20170321	20110116	20100629	20101114	
20151027	20170402		20100814	20101230	
20151120	20170414		20100929	20110214	
20151214	20170508		20101114		
20160107	20170520		20101230		
20160131			20110214		
20160717					
20160810					
20160903					
20160927					
20161021					
20161114					
20161208					
20170125					
20170218					
20170314					

Table 3-3 Table of acquisition dates for each SAR data set, RADARSAT-2 (RS2-W1), Sentinel-1A (S1A-IW), three overlapping ALOS frames (ALOS1) and ALOS-2. The location of these tracks are shown in Figure 3-1. Acquisition dates in the format YYYYMMDD and bold, red dates represent the master images chosen during processing.
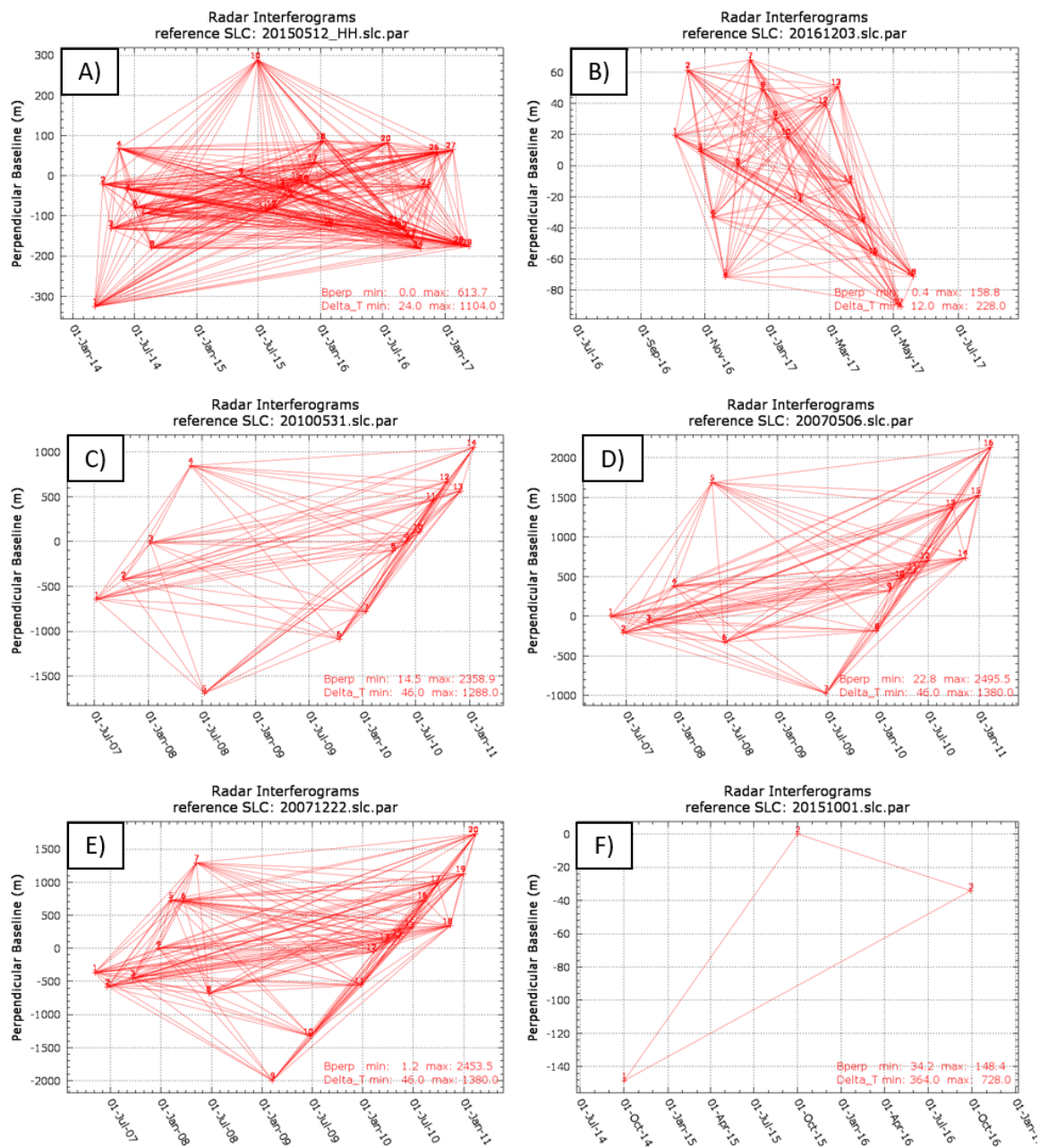
Figure 3-2 Perpendicular baseline plot for the four satellites used in this study, A) RADARSAT-2 W1, B) Sentinel-1A IW, C) ALOS1-620_173, D) ALOS1-630_172, E) ALOS1-620_172 and F) ALOS-2 Note the different scales for perpendicular baseline and time.

3.1.1   RADARSAT-2

The Canadian RADARSAT-2 satellite was launched in December 2007 as an expansion in remote sensing capabilities to that of the RADARSAT-1 satellite. RADARSAT-2 is still currently operational and acquires data at various spatial resolution and coverage, ranging from ~1 meter resolution using Spotlight mode (18 x 8 km coverage) to 100 m resolution from ScanSAR wide mode (500 x 500 km spatial coverage) (Canadian Space Agency, 2015)

RADARSAT-2 operates with a C-band (5.6 cm wavelength) sensor, single, dual or quad polarization (transmit H and/or V, receive H and/or V), with an orbital repeat cycle of 24 days. SAR antennas are designed to emit and receive specific polarizations, most commonly they operate with horizontal (H) or vertical (V) linear polarizations (Natural Resources Canada, 2014). These characteristics make this satellite an ideal candidate for interferometric applications and time series analysis.

In this study, 29 RADARSAT-2 wide beam images were collected over the region between 6 March 2014 and 14 March 2017. These wide beam mode images have 150 km swath width with 30 m spatial resolution. These images were processed using HH polarization as discussed in Chapter 3.2.

3.1.2   Sentinel-1A

The Sentinel-1 constellation consists of two C-band satellites (Sentinel-1A and Sentinel-1B) each with an orbital period of 12 days each, or 6 days when both are operational. Sentinel-1A was launched on 3 April 2014 and Sentinel-1B on 22 April 2016 and are both operated by the European Space Agency (ESA, 2017a). A variety of beam modes are available including Stripmap (SM), Interferometric Wide swath mode (IW), Extra Wide (EW) and wave mode (WV).

In this study, I collected (IW) images over the study region between 4 October 2016 and 20 May 2017. This large, ascending set of images compliment the spatially overlapping descending RADARSAT-2 dataset acquired over the same time period (2016 to 2017).

Similarly, Sentinel operates with the same C-band sensor as RADARSAT-2, with 5.6 cm wavelength.

IW mode images acquired in this study cover 250 km, with a range and azimuthal resolution of 2.3 and 14.1 meters respectively (ESA, 2013). IW images are also imaged with a unique mode known as Terrain Observation by Progressive Scans (TOPS) that must be taken into consideration when processing, as discussed in Chapter 3.2.9.

3.1.3   ALOS PALSAR 1 and 2

ALOS and ALOS-2 PALSAR (Phased Array type L-band Synthetic Aperture Radar) are satellites operated by the Japan Aerospace Agency (JAXA), ALOS launched in 2006 and deactivated in 2011, whereas ALOS-2 is still operational and has been collecting images since 2014.

ALOS PALSAR has two main beam modes, fine beam single polarization (FBS) and fine beam dual polarization (FBD), as well as ScanSAR wide beam and a polarimetric mode (PLR). Table 3-4 shows the characteristics for the FBS and FBD beam modes including swath width (70 km) and spatial resolution. Both ALOS satellites use an L-band (24 cm wavelength) sensor which is significantly longer than wavelengths of other satellites in this study (C-band, 5.6 cm wavelength). However, one main advantage of using a sensor with longer wavelength is that the temporal decorrelation of the interferometric phase is lower, especially in vegetated, low coherence regions (Hanssen, 2001).

	FBS	*FBD*
Center Frequency	L-Band (1.27 GHz)	
Polarization	HH or VV	HH+HV or VV+VH
Spatial Resolution	10 m	20 m
Swath Width	70 km	70 km
Off-Nadir Angle (°)	34.3	

Table 3-4 ALOS PALSAR fine beam mode characteristics that were used in this study, fine beam single (FBS) and fine beam double (FBD).

In this study, three separate, overlapping, ascending ALOS frames were acquired over the region as shown in Figure 3-1. Two of these sets of images are different frames on the same orbital track, number 172 (620_172 and 630_172). For each of the three frames, FBS and FBD data were collected, which can then be simultaneously processed as a single dataset through oversampling. This process is discussed in Chapter 3.2.

Furthermore, these ALOS images were acquired much earlier in time, 2007 to 2011, so an older time period of surface deformation can be compared to that of Sentinel-1A and RADARSAT-2.

ALOS 2 launched in 2014 and is currently operational. In this study, three level 1.1 FBD images were acquired between 2 October 2014 and 29 September 2016. These three images were processed in HH polarization, as discussed in Chapter 3.2.

3.2   DInSAR Data Processing

In this study, I processed all interferograms, from raw data to final differential interferograms and displacement maps using Gamma software, a product of GAMMA Remote Sensing (Wegmuller & Werner, 1997).

The following sections (Chapters 3.2.1 to 3.2.8) discuss the general procedure for processing strip-map mode data such as, RADARSAT-2, ALOS PALSAR and ALOS-2 interferograms. However, Sentinel-1, has a novel Terrain Observation by Progressive Scans (TOPS) mode which is significantly different to strip-map mode processing (Yague-Martinez et al., 2016). Therefore, Sentinel-1 TOPS mode processing is discussed separately in Chapter 3.2.8.

The entire differential interferogram generation procedure is outlined in Figure 3-3, for the case of an interferometric pair. In this pair, one image is selected to be the reference image for which all other images are resampled to. The reference image is referred to as the *master* and the resampled image as the *slave* for the remainder of this study. The script I created to processes differential interferograms for RADARSAT-2, ALOS and ALOS-2 can be seen in Appendices A and B.
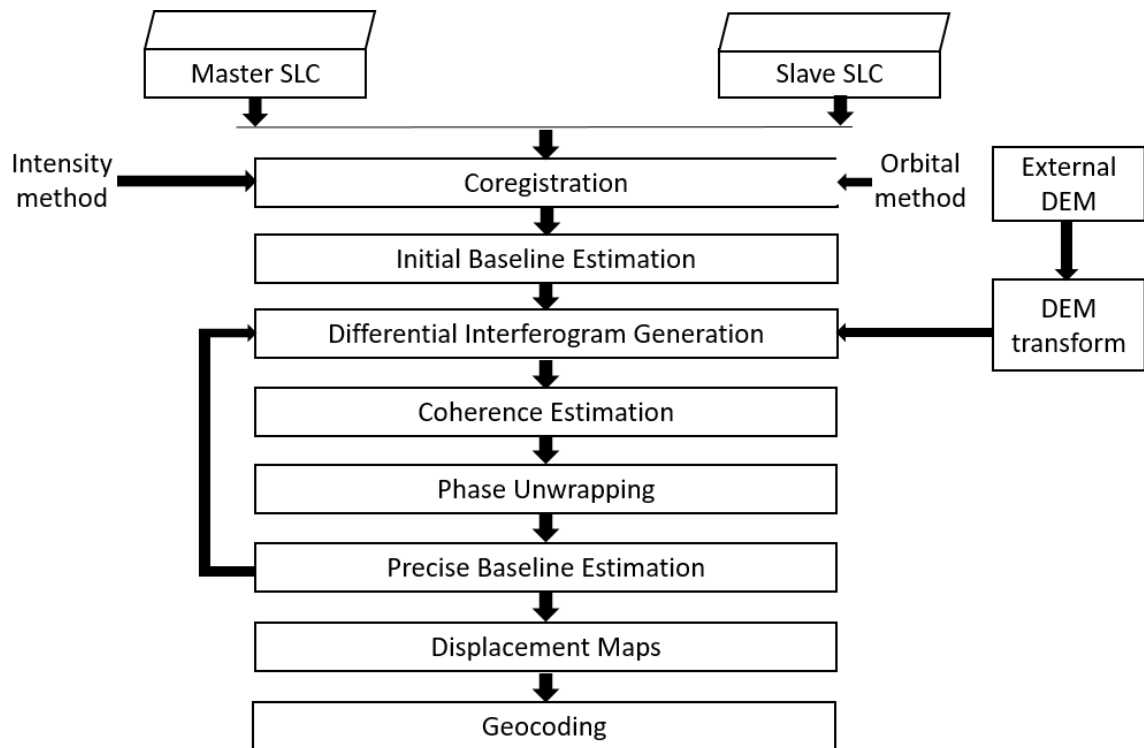
Figure 3-3 Processing flow chart for generating geocoded differential interferograms and displacement maps for strip-map mode data from a stack of coregistered images.

Firstly, before images can be processed using the GAMMA software, some pre-processing steps are required. Images are first transformed from raw data into Single Look Complex (SLC) format, an image that has been focused and the phase has been preserved (Hanssen, 2001). This process can vary depending on the satellite that is being processed and the processing facility. For example, RADARSAT-2 data must first be converted from GEOTIFF and XML format to SLC. This includes generation of SLC parameter file which contains all information concerning sensor and acquisition mode, geographical coordinates and acquisition time.

Another pre-processing step that is required for the case of ALOS PALSAR data, is the oversampling of FBD SLCs to match the resolution of FBS SLCs. As discussed in Chapter 3.1.3, FBS (10 m) has twice the resolution of FBD (20m), so an oversampling factor of two is applied to all FBD images to match this resolution. This pre-processing step is performed using the program *SLC_ovr_all* (Appendix B).

Also in the case of ALOS data in this study, frames along the same track can be mosaicked and cropped to create a single SLC over the region of interest. This can be seen in Figure 3-4, where a single set of SLCs can now be processed to generate differential interferograms.
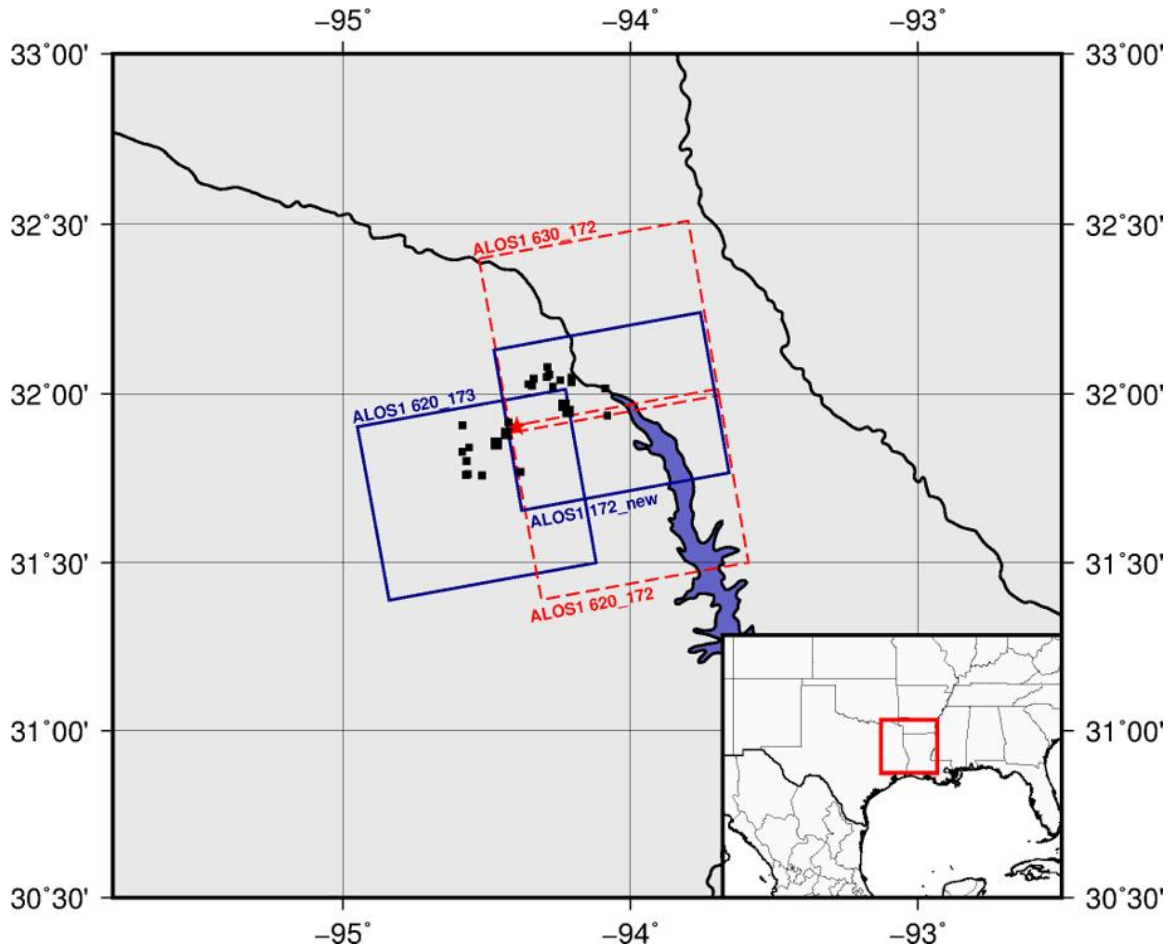
Figure 3-4 ALOS frames used in this study, including the mosaicking and cropping of two sets of ALOS frames along the same path, 172. Original frames (red dashed outline) that were mosaicked and cut to region of interest (ALOS1 172_new). Major and minor injection wells are shown (black squares), as well as location of M4.8 2012 Timpson earthquake (red star).

3.2.1   Coregistration

Once the SAR images are in SLC format, they can be processed with GAMMA software (Wegmuller & Werner, 1997). Differential interferometric processing of complex SAR data combines two SLC images into an interferogram. This requires coregistration of the offsets between the slave and master SLC image forming the interferometric pair, and resampling of the slave to perfectly match the master image.

In order to resample a set of SLCs to a common master SLC, I used the GAMMA script *SLC_resamp_all* (GAMMA, 2009). First, this script reads in a stack of SLC images and generates an offset parameter file, which provides an initial estimate of the offset between images to be coregistered. Coregistration is the pixel-to-pixel match between common features in SAR image pairs. It ensures that two SAR images are near perfectly aligned and phase differencing can be accurately performed (Li & Bethel, 2008). Initial offsets are generated which match the images with one or two pixel accuracy, also known as *coarse coregistration*. However, after this pixel level coregistration an interferogram may be generated but it is not adequate for DInSAR processing (Li & Bethel, 2008). The initial range and azimuth offsets then can be measured using orbital state vectors, obtained by *init_offset_orbit*, or cross-correlation values using *init_offset.*

Once the initial offsets have been computed, a subpixel-to-subpixel match between images can be calculated, called *fine coregistration*. This process involves predicting a field of estimates of the offsets, based on the cross-correlation of image intensities, also known as intensity tracking. In this process, I defined a window size in which the offsets in range and azimuth are estimated for, by crosscorrelating the images to find the maximum intensity. After these steps are completed, the slave SLCs are resampled to the master's geometry using these precise offset models.

3.2.2   Initial Baseline Estimation

The next step in DInSAR processing is to estimate the initial baselines. These baselines are used in future steps, such as interferogram flattening, filtering and phase unwrapping. As mentioned in Chapter 1.4.2, a baseline is the spatial distance between SAR acquisitions and relies on knowing precise satellite orbits. In this processing step, I used *base_calc*, a program that uses a satellites orbital information (useful for when an interferogram has not yet been calculated). This program generates an initial baseline parameter file, providing the perpendicular baseline between slave and master images, that then can be used later for precise estimation of interferometric baselines.

3.2.3   Differential Interferogram Generation

The first step in differential interferometry is to simulate the unwrapped topographic phase including the curved earth component using a DEM that has been transformed into radar coordinates (GAMMA, 2008). Once a stack of SLCs have been coregistered and resampled to a common master and the baselines estimated, a complex interferogram can be generated. This calculated interferogram will include a phase contribution known as the *curved Earth* phase, due to the curvature of the Earth which is defined in Equation 1-5. When generating an interferogram it is assumed that the surface is flat, however the Earth's surface is in fact curved. This curvature causes a linear variation in range distance across the image which can be removed with a process known as interferogram "flattening".

However, in differential interferometry the curved Earth phase is removed along with other phase components, such as topography, when a simulated interferogram is subtracted from the calculated interferogram. After these phase components have been removed, all that should remain in the interferogram is the phase component of surface deformation. A simulated interferogram is generated in two-pass differential interferometry using an external DEM which must be transformed from map to coordinates (GAMMA, 2008). For this study I acquired an external DEM that covered the satellite footprints for all the datasets, an NGA SRTM 1 arc-second" (30 m resolution) DEM from Global Data Explorer (USGS, 2017). The DEM is transformed to radar coordinates using the GAMMA program *mk_geo*. This program generates a lookup table using a simulated SAR image, generated from the external DEM, to measure offsets between a simulated and master SLC image. Figure 3-5 shows the final transformed master SAR image in map geometry using the DEM geocoded lookup table and simulated DEM, that is now suitable to simulate the unwrapped topographic and curved Earth phase trend.
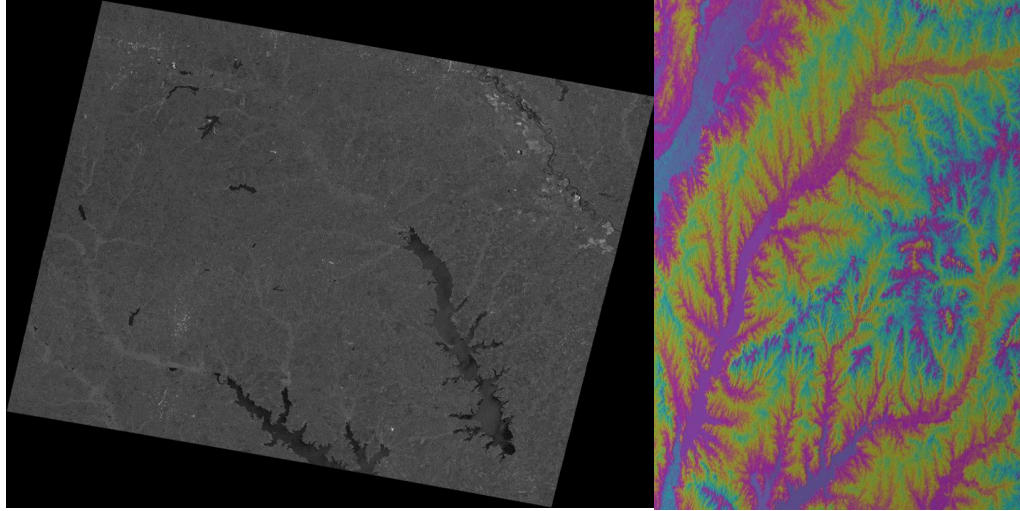
Figure 3-5 Terrain geocoded SAR intensity image (left) alongside simulated DEM in radar geometry (right) for RADARSAT-2.

I generated a parameter file for the differential interferogram to be computed using *create_diff_par*. I then simulated the unwrapped topographic phase from my DEM using *phase_sim*, which is subtracted from the original interferogram using *SLC_diff_intf*.

However, since the orbital baseline information was only an initial estimate, this process is not sufficiently accurate, thus refinement of the baseline is needed (Wegmüller et al., 2004). This is achieved by applying *base_init*, by recalculating the initial baseline using the calculated interferometric phase. The refined baseline model can then be iterated and re-applied to simulate for topographic phase to generate the final wrapped differential interferogram. This phase image is wrapped since it represents a measure of phase differences that are only known modulo 2π (Chirico & Schirinzi, 2012).
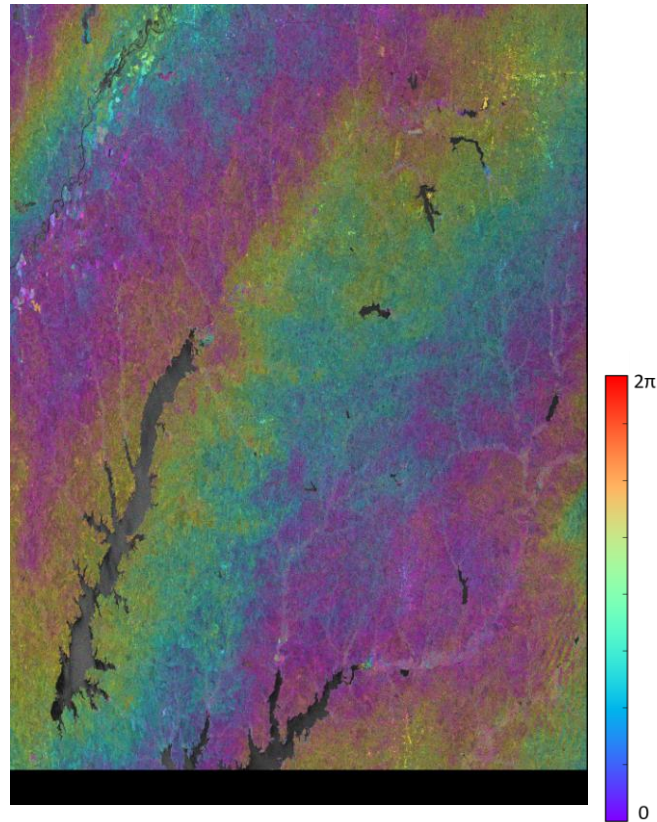
Figure 3-6 Wrapped differential interferogram for RADARSAT-2 between 18/02/2017 – 14/03/2017. A single fringe is shown as a complete colour cycle from red to purple.

An example of a generated wrapped differential interferogram is shown in Figure 3-6, where phase values are wrapped in the interval between 0 and 2π. The only phase component remaining in this image should be that of surface deformation, as well as nuisance terms such as atmospheric noise and residual orbital ramps. A long wavelength signal can be seen in Figure 3-6, indicating that orbital errors are still present in the phase which can later be removed using precise baseline estimation (Chapter 3.2.7).

For each dataset, I generated differential interferograms using the associated script shown in Appendix A for RADARSAT-2 and Appendix B for ALOS and ALOS-2.

3.2.4   Coherence Estimation

Once a differential interferogram is generated, the coherence can be estimated. This is calculated from the cross-product of two coregistered SLCs and represents how much

these images are correlated with each other. The correlation δ, measures the similarity between two images Z_1 and Z_2,

$$\delta = \frac{\sum_{i=1}^{L} Z_1 Z_{2_i}^*}{\sqrt{\sum_{i=1}^{L}|z_{1_i}|^2}\sqrt{\sum_{i=1}^{L}|z_{2_i}|^2}}$$ (Equation 3-1)

after Touzi et al., (1999), where L is the total number of measurements and i is the sample number. The absolute coherence d can then be calculated whereby,

$$d = |\delta|$$ (Equation 3-2)

Cross-correlation is performed through estimating a value for d, for a two-dimensional window that crosses the entire SAR image. The size of this coherence window is an important factor in estimating coherence. In regions of low coherence, it is recommended to use larger estimation windows. For increasing window size, the estimation bias and uncertainty decreases, however the spatial resolution also decreases (GAMMA, 2007). In this study, I used an estimation window of seven whilst using the program *cc_wave*, with the resulting coherence image shown in Figure 3-7. Low coherence (blue colours) signifies areas that have undergone significant changes in phase characteristics between acquisitions, due to vegetation for example. However, high coherence (magenta colours) represent regions where the phase characteristics have remained relatively stable between acquisitions. Furthermore, yellow regions represent urban areas with very high coherence as these areas remained stable over the study period.
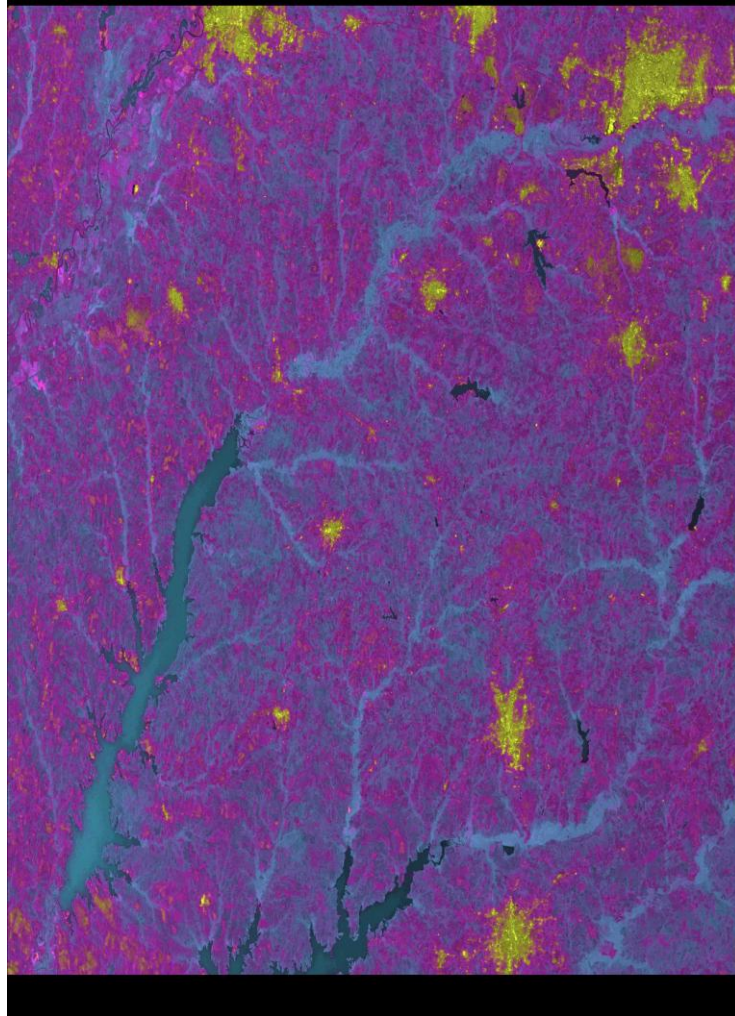
Figure 3-7 Average coherence image from stack of RADARSAT-2 interferograms, with average backscatter intensity image as background. Magenta represents high coherence and blue represents low coherence. Urban areas are represented as very high coherence and intensity (yellow).

3.2.5   Interferogram Filtering

Once the final differential interferogram has been created, filtering and phase unwrapping can be performed. Filtering aims to reduce phase noise in an interferogram, thus making phase unwrapping more efficient and robust. There are two methods to filter an interferogram, multilooking and an adaptive filtering technique.

Multilooking can be performed on the differential interferogram itself, or prior to interferogram generation by multilooking the coregistered images. Using a weighted average over a number of resolution cells with a specified window size, dominant scatterers will constructively sum, whereas noisy pixels will destructively interfere. This will effectively improve the phase statistic and probability density function (PDF) of the interferometric phase. This multilook interferometric phase PDF characterizes the cross-correlation and is a function of interferometric phase and multilooking factor (Haynes, 2017). As a result of multilooking, spatial resolution is decreased by the factor of looks in the azimuth and range direction. In this study, I performed multilooking for all coregistered SLC images using the program *mk_mli_all*, varying the multilooking factor in range and azimuth based on the sensor being processed. The multilook factor used for each of my sensors can be seen in Table 3-5.

Satellite	Pixel Size (Range:Azimuth) (m)	Multilooking factor (Range : Azimuth)	Multilooked Pixel Size (Range:Azimuth) (m)
RADARSAT-2	11.8:5.2	3:10	35.5:52.2
ALOS PALSAR	4.7:3.2	6:10	28.1:31.6
ALOS-2	4.3:3.8	7:8	30.0:30.3
Sentinel-1A	2.3:14.0	12:2	28.0:28.0

Table 3-5 Multilooking factor used for each satellite and resulting spatial pixel size for the differential interferogram.

Another method of filtering differential interferograms is using the adaptive filtering technique after Goldstein and Werner (1998). This technique dramatically reduces phase noise whilst maintaining spatial resolution in the complex interferogram. I applied the adaptive filtering program *adf* for each differential interferogram, which filters based on the local fringe spectrum.
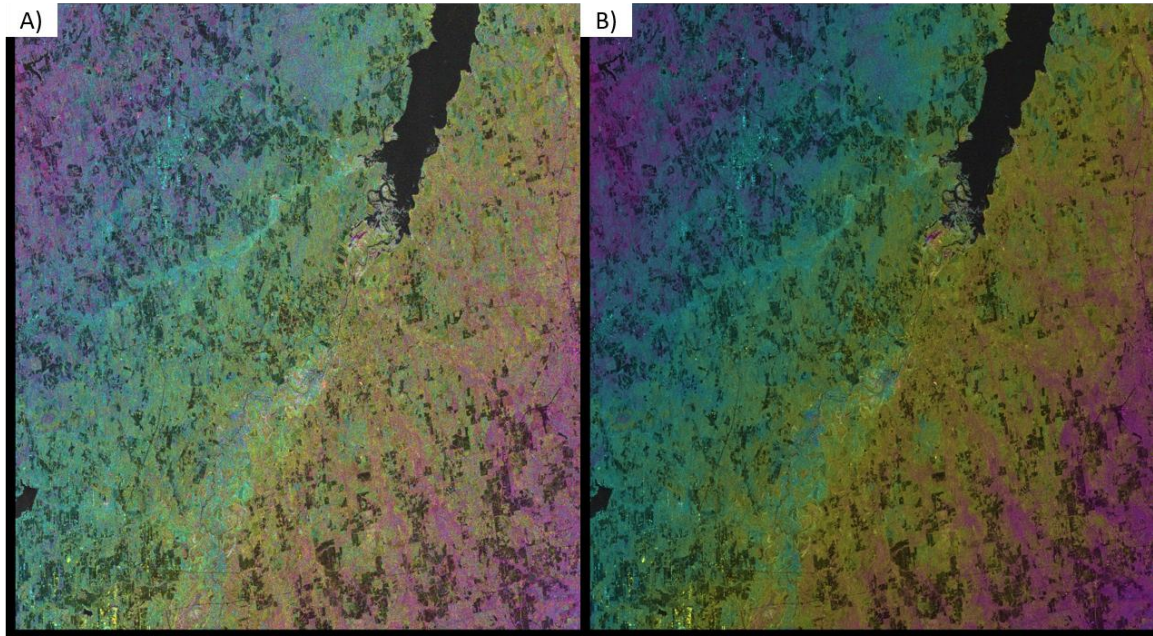
Figure 3-8 Filtered ALOS PALSAR differential interferograms spanning 29/03/2010 – 14/11/2010 with intensity image as background, A) unfiltered and B) filtered using adaptive filtering technique.

This program calculates the local power spectrum over a small window of the complex interferogram, designs a filter based on this spectrum, filters the interferogram, estimates the phase noise coherence and computes the filtered interferogram and coherence map (GAMMA, 2009). Results of applying this filtering technique to an ALOS PALSAR differential interferogram can be seen in Figure 3-8, with images before (A) and after (B) filtering showing an increase in phase signal strength due to filtering.

3.2.6　Phase Unwrapping

From the complex differential interferogram calculated above, the interferometric phase is only known from 0 to 2π. To relate the interferometric phase to the interferometric imaging geometry, resulting in displacement information, this phase must be unwrapped (Hooper & Zebker, 2007). For this conversion, an integer of 2π must be added to obtain

the absolute, unambiguous phase difference for sequential phase values across the image, a process known as *phase unwrapping*. Figure 3-9 shows a simple representation of the phase unwrapping process in order to match the elevation profile from the wrapped phase.
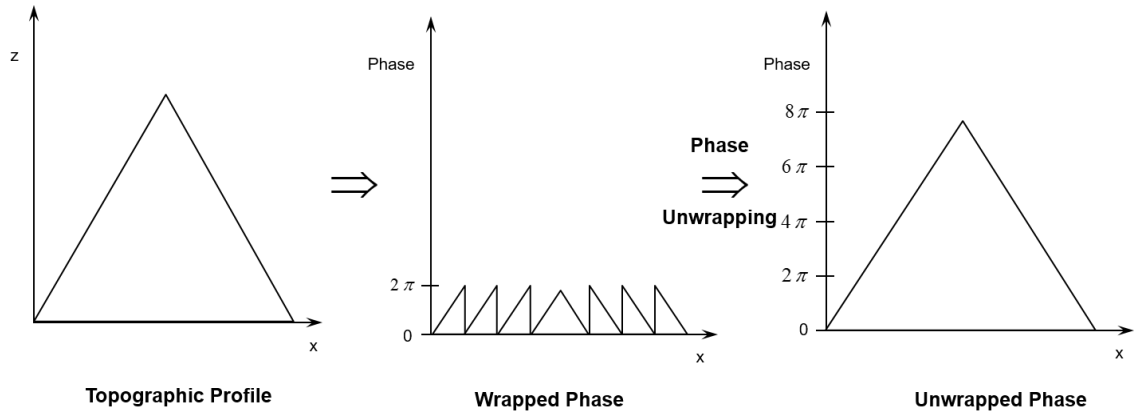
Figure 3-9 Simple representation of the phase unwrapping procedure from elevation profile (left), to the wrapped phase (middle) to unwrapped phase (right). Modified after van Zyle, (2016).

Phase unwrapping is a key problem in all applications of SAR interferometry (Costantini, 1998). There are many issues that unwrapping must overcome, for example unwrapping is impossible when noise exceeds one fringe threshold (2.8 cm for C-band) (Samsonov et al., 2015). Discontinuities in the phase, due to noise that was not filtered or masked, will also limit unwrapping and therefore requires relatively smooth surfaces. The flatter the interferogram to be unwrapped, the better the unwrapping performance.

There are two methods of phase unwrapping supported in the GAMMA software, the branch cut (BC) region growing algorithm and minimum cost flow (MCF) (Costantini, 1998). In this study, I used the MCF method, which is a global optimization technique for solving the phase unwrapping problem. The advantage of this technique is that it considers gaps in the input data (or low coherence regions within the wrapped interferograms), so it is efficient and robust at unwrapping very large interferograms (GAMMA, 2009). There are five steps to this procedure: generation of a phase unwrapping validity mask (based on a chosen threshold value), adaptive sampling

reduction for the validity mask, unwrapping of the phase, weighted interpolation to fill in missing gaps in the unwrapped phase and finally using the interpolated unwrapped phase as a model for unwrapping the differential interferogram (GAMMA, 2009; Refice et al., 1999; Werner et al., 2002). In Gamma, I performed these steps for unwrapping using the script *mk_unw_all*, which uses the programs *rascc_mask*, *rascc_mask_thinning* and then *mcf*. An example of the resulting unwrapped, filtered differential interferogram can be seen in Figure 3-10.
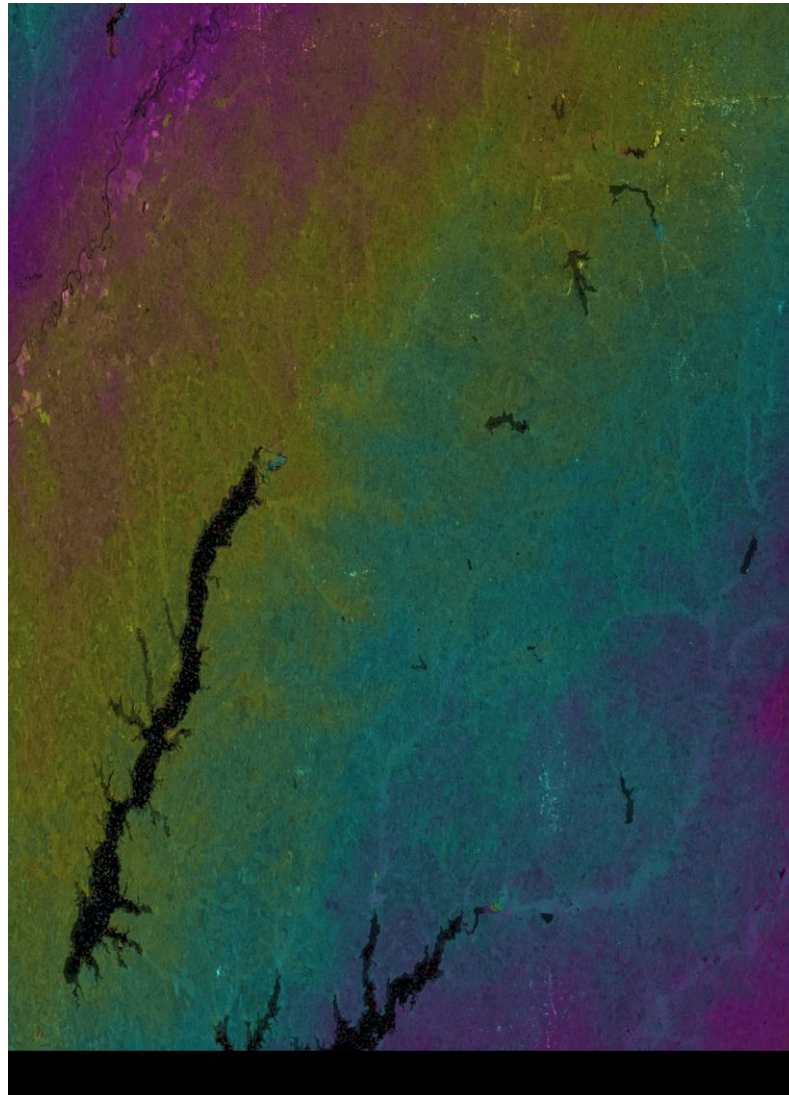
Figure 3-10 Unwrapped phase for the filtered RADARSAT-2 differential interferogram spanning 18/02/2017 – 14/03/2017 with amplitude image as background.

3.2.7   Precision Baseline Estimation

Once a differential interferogram has been unwrapped, there may be some remaining residual phase components such as baseline orbital ramps that were not completely removed during interferogram generation. An initial estimate of the baseline was calculated from the orbital data (Chapter 3.2.2), which was precise enough for the removal of the curved Earth phase and interferogram filtering. However, this estimate is not accurate enough for the inversion of unwrapped interferometric to topographic heights (Chapter 3.2.8). Therefore, an improved estimate of the interferometric baseline can be done using least squares fit, for a set of ground control points (gcp) of known topographic height, which are selected using the program *gcp_ras* (GAMMA, 2007). Once ground control points have been selected, a least squares estimation of the interferometric baseline can then be obtained, using the program *base_ls*. In my processing script, these programs are performed using the GAMMA program *mk_base_2d*.

3.2.8   Displacement Maps and Geocoding

After the precision baseline has been calculated, the unwrapped interferometric phase can be converted to elevation. This is performed based on Equation 1-4, knowing the precise baseline leaves only the contribution to surface displacement in the final interferogram. Finally, the unwrapped interferogram and displacement maps can be geocoded from radar to map coordinates using the lookup table described in Chapter 3.2.3. An example is shown in Figure 3-11, noting that areas of low coherence, below a chosen threshold of 0.4, are masked and shown in black.
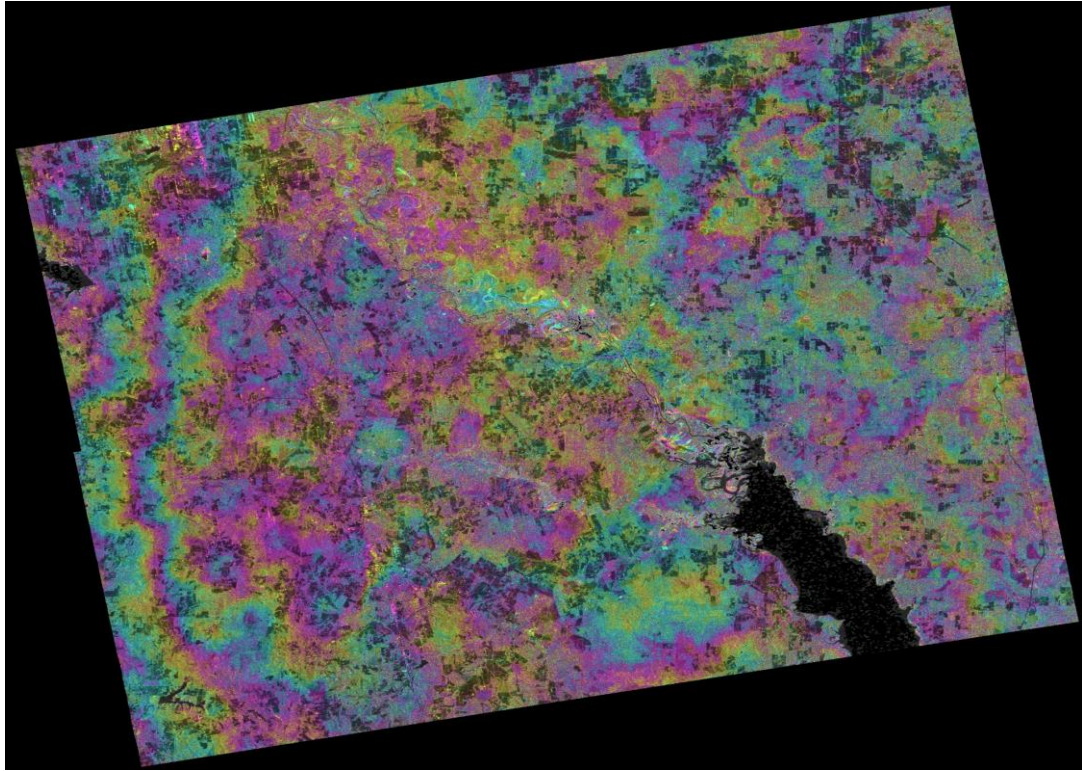
Figure 3-11 Geocoded displacement map of ALOS PALSAR image spanning 06/05/2007 – 21/06/2007. Each fringe represents 3 cm displacement.

The final displacement map shown in Figure 3-11 should include only ground displacement motions. However, other factors such as atmospheric effects, imperfect baseline estimation and inaccuracies in the DEM also may be present in the final displacement map and lead to misinterpretation of fringes.

3.2.9   S1 TOPS-Mode Processing

Sentinel-1 TOPS acquisition mode, which is similar to ScanSAR, acquires images by recording subsets of echoes of the SAR aperture, known as *bursts* (Yague-Martinez et al., 2016). The 5.4 GHz SAR sensor is capable of providing different resolution data in four different modes: Interferometric Wide Swath (IW), Extra Wide Swath (EW), StripMap

(SM) and Wave (WV). In this section, I will discuss IW processing using the Terrain Observation by Progressive Scans (TOPS) mode.

Level-1 IW SLC data is provided by ASF agency as three separate sub-swaths, each containing a series of bursts which have already been individually pre-processed as a separate SLC image. There are 10 bursts within a single sub-swath and adjacent sub-swaths overlap. The configuration of which is shown in Figure 3-12 for the case of 3 bursts per sub-swath.
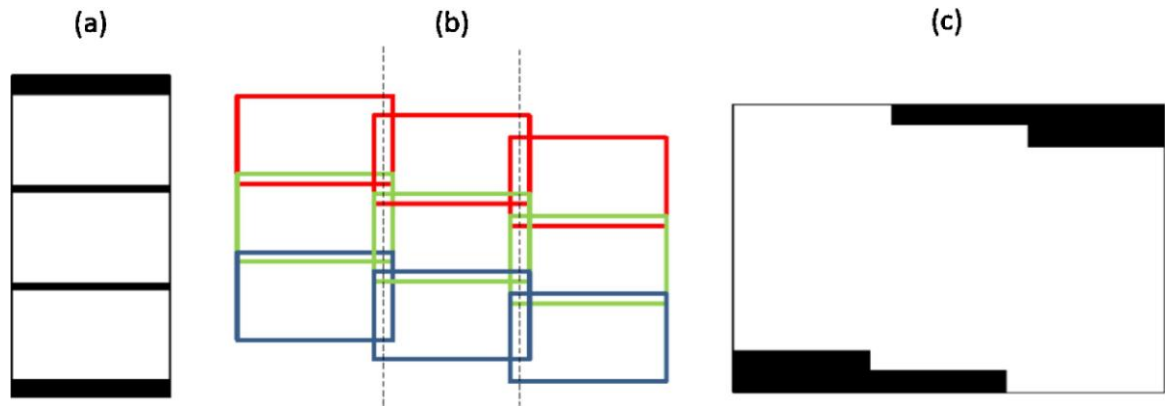
Figure 3-12 a) Sentinel-1 burst arrangement within an individual IW sub-swath, b) burst structure within adjacent sub-swaths showing region of overlap, c) mosaic of 3 sub-swaths of IW mode, with 3 bursts within each sub-swath. After Sowter et al. (2016) and Wegmüller et al. (2015)

Upon downloading the IW TOPS mode raw-data, pre-processing can be performed to generate a set of SLCs that cover the target region. This includes generating SLCs for each sub-swath, deramping of each sub-swath, multilooking and mosaicking of bursts or sub-swaths. These steps are all performed using my pre-processing script (Appendix C).

Due to the large spatial coverage and high resolution of S1 TOPS mode data, mosaicking an entire frame (all three sub-swaths) will lead to very large image files. Therefore, to optimize processing, it is recommended that individual sub-swaths or bursts are selected which cover the target region. For this investigation, I processed only sub-swath-1 since this covered my entire area of study (as shown in Figure 3-1).

First, raw data must be converted to SLC format which GAMMA software can process. This is generated using the program *par_S1_SLC* for each individual sub-swath. The first key difference in TOPS mode processing, from that of traditional strip map mode data, is deramping. For each TOPS mode burst, the Doppler Centroid, runs through a steep spectral ramp from the start to end of each burst (Wegmüller et al., 2015). The Doppler Centroid is the Doppler frequency received from a given point scatterer on the surface when it is centered in the azimuth antenna beam pattern (Kavanagh, 1985). TOPS mode employs a rotation of the antenna in the azimuth direction, known as beam sweeping, which causes variations in the Doppler Centroid frequency of 5.5kHz (ESA, 2017b). The azimuthal phase ramp must be considered for some processing steps, such as interpolating SLC data. However, since a phase ramp is being subtracted, this will influence interferometry, because phases have changed, it is not considered in my processing steps.

The second important difference between TOPS and traditional strip map mode processing is the coregistration procedure. In TOPS processing, images must be resampled at one thousandth of a single SLC pixel (equivalent to 2 cm azimuthal offset) to avoid phase jumps between burst interfaces. To achieve very high resampling accuracy between SLC pairs, two coregistration methods are iteratively used, intensity matching and spectral diversity methods (Scheiber & Moreira, 2000). Firstly, a coregistration lookup table between the master and slave is generated using the program *rdc_trans*. Then the refinement of this lookup table can be determined using an intensity matching procedure, resampling the slave to master geometry.

Once the intensity matching method has been iterated until the azimuth correction is < 0.01 pixel, further refinement can be performed using the spectral diversity technique. This unique method considers the double difference phase in the burst overlap regions (Wegmüller et al., 2015). The double difference phase is computed by differencing an interferogram calculated in a forward viewing geometry, and that in a backward viewing geometry (Grandin et al., 2016).

Due to the large Doppler variation, even the smallest coregistration error can cause significant phase effects, which can then be used to determine residual coregistration errors. Using the burst overlap regions, if coregistration is perfect, no phase errors will be observed. However, in the case of a small mis-registration, a constant phase offset can be measured. This offset relates linearly to the azimuth coregistration error (Scheiber & Moreira, 2000). Therefore, we can determine this phase offset in the burst overlap region and convert it to an azimuth offset correction, vastly improving refinement of the coregistration lookup table to <0.0005 pixel. To efficiently iterate this process, GAMMA has a script that automates this process using both these techniques, *S1_coreg_TOPS*.

The main challenge in Sentinel TOPS interferometry is the coregistration and resampling of data. Once these master and slave images have been perfectly coregistered, the normal procedure for differential interferometry can be used. For example, a simulated phase using an external DEM can be subtracted from the interferometric phase to produce a differential interferogram. Phase filtering (Chapter 3.2.5) and unwrapping (Chapter 3.2.6) can also be performed as for traditional interferogram processing.

3.3   MSBAS Processing

The previous section describes how DInSAR processing produces unwrapped, geocoded interferograms and displacement maps. These maps can be analyzed individually, or can be used to form time series at individual points in the interferograms. Historically, these techniques can only use data from one satellite to create these time series (Berardino et al., 2002; Ferretti et al., 2001; Hooper et al., 2004). The MSBAS method (Samsonov et al., 2017) uses interferograms from different satellites, look-angles, resolutions and wavelengths to produce integrated time series over different coverage periods. Here I employed MSBAS processing because of the variety of data sets available in Timpson, TX over the time period of interest. While a detailed manual for MSBAS can be found by Samsonov and D'Oreye (2017), here I present an overview of the algorithm and the processing steps used in this study.

MSBAS software is written in *C++* programming language and can be simply recompiled on any standard operational system such as Windows or Linux. In order to run the software, a header file must be provided on the command line in order to set the control parameters for the MSBAS algorithm (Chapter 3.3.1).

The processing flowchart for the MSBAS algorithm can be seen in Figure 3-13. Prior to running the MSBAS code there are a few steps that need to be performed (processing steps with dashed outline in Figure 3-13). First, ascending and/or descending SAR datasets must be selected before DInSAR processing can be performed to generate unwrapped and geocoded interferograms. As discussed in 1.4.3, these images should only contain information on surface displacements, after every other phase component has been corrected for. Second, a common region is selected that is covered by each of the datasets to be processed. Input interferograms can then be resampled to this common grid and interpolated to the same defined spatial resolution. Third, using an average coherence threshold, only highly coherent interferograms are resampled to this common grid. In this study, interferograms that fit the criteria (average coherence > 0.6) were resampled using Generic Mapping Tools (GMT) (Wessel et al., 2013) scripts (Appendix E), to a common latitude/longitude grid with a uniform spatial sampling of ~30 meters. Although dramatically reducing the number of interferograms available to process, this ensured only the most coherent, thus reliable deformations are processed with MSBAS. Finally, if there is any remaining noise within these resampled images, such as residual orbital ramps or atmospheric noise, these must be removed prior to MSBAS processing.
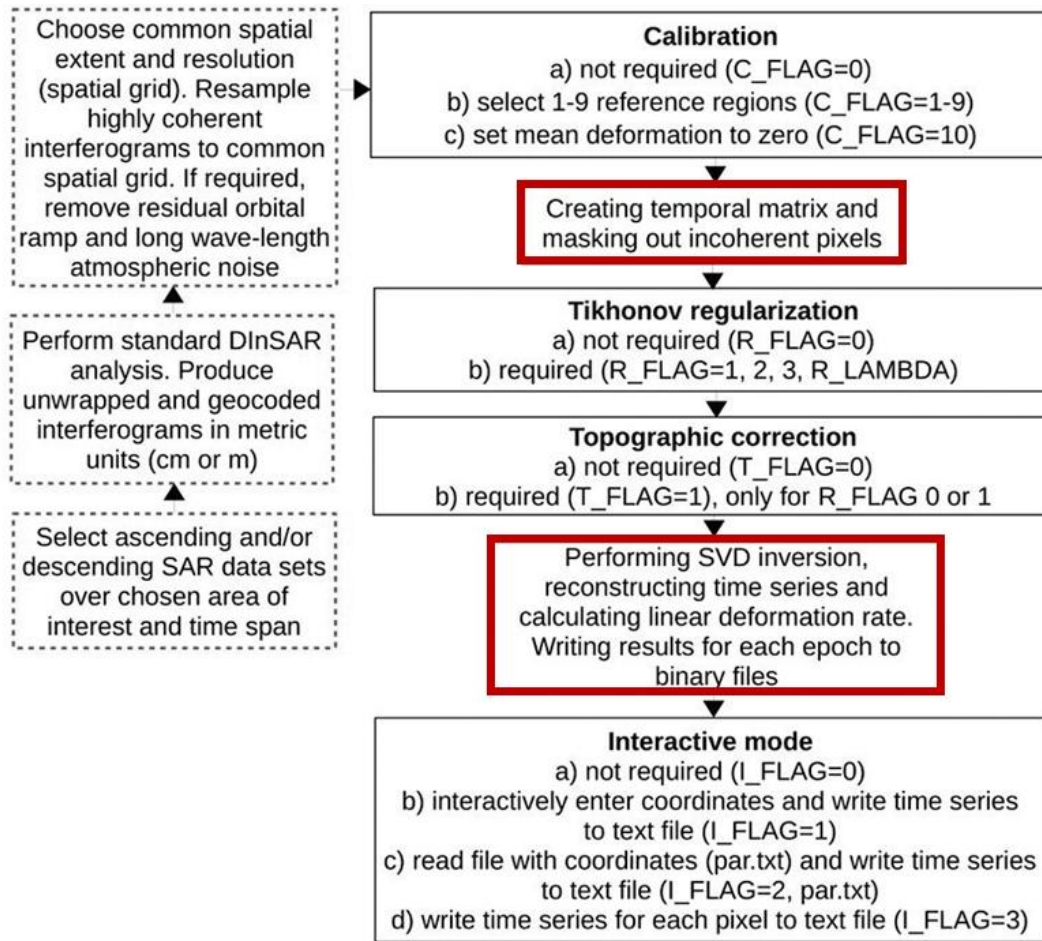
Figure 3-13 MSBAS processing algorithm flowchart. The first three steps in dashed are processing steps performed prior to MSBAS. Processing steps highlighted in red are compulsory and cannot be changed by the user. The remaining steps with thin black outline are optional processing parameters that may be manipulated, modified after Samsonov and D'Oreye (2017)

3.3.1   MSBAS Control Parameters

Once a set of highly coherent interferograms, which have been resampled to a common grid, have been produced, only then can the MSBAS algorithm be applied. Figure 3-13 highlights MSBAS processing steps, some of which can be manipulated by the user, i.e. setting parameter flags within a header file. There are two major steps in this algorithm that are compulsory 1) generating a temporal matrix and mask for coherent pixels, and 2) run SVD inversion (defined in Chapter 1.5.2) on the dataset to reconstruct the time series

of deformation and write these to output files. The temporal matrix consists of a series of surface displacements for each dataset at each common time step. Once a coherence mask has been generated, for pixels that remain coherent for each interferogram, SVD inversion is run to compute the deformation time series.

There are multiple parameters that are designed to control the processing flow of the MSBAS algorithm. These control parameters can be seen in Figure 3-13 and Table 3-6, with an example of the header file shown in Table 3-7. All the control parameters mentioned in this section must be sequentially ordered in a header text file that is run with the MSBAS code.

Firstly, the *FORMAT* parameter controls the format of the input data, depending on whether it is four bytes float, big endian or small endian. The *FILE_SIZE* parameter controls the number or rows and columns in the input resampled interferograms. Likewise, *WINDOW_SIZE* controls the size and location of the sub-region to be processed. This parameter improves processing efficiency, saving memory and processing time, when an entire region is not needed. *C_FLAG* is the calibration parameter that controls how each interferogram is calibrated. A region is selected on the interferogram which acts as a reference point for all interferograms. Setting C_FLAG = 10 sets the average of each interferogram to zero and is usually a good starting guess to get an idea of the deformation. However, most commonly a single reference region is selected that is stable throughout but close to the area of deformation, since the DInSAR precision is inversely proportional to the distance between reference and measured regions (Samsonov et al., 2017). *R_FLAG* controls the order of regularization, zero, first or second order, and the value of the regularization parameter λ. The regularization parameter can be found by computing L-curve analysis. *T_FLAG* is the topography control parameter that can be set equal to one to solve for residual topography. However, with the use of modern, high-resolution DEMs, the topographic residual is usually very small and does not need to be corrected for. This correction can also only be used for problems that are non-regularized (R_FLAG=0) or zero-order regularized (R_FLAG=1). *I_FLAG* is an interactive parameter that controls what is written to file. In this study, par.txt is provided which provides a list of points for which the deformation time series is

generated. Finally, *SET* provides information on the time of acquisition of each dataset (hhmmss), the azimuth (θ) and incidence angle (φ) measured in degrees and a file containing a list of interferograms to be processed (set.txt). This file also contains the perpendicular baseline for each interferogram and master and slave acquisition dates.

Parameter	Value	Parameter Description
FORMAT	*0*	*4 bytes float, small endian*
FORMAT	*1*	*4 bytes float, big endian*
FILE_SIZE	*x, y*	*Size of input file, 1000, 1000 for example*
WINDOW_SIZE	*x_a, x_b, y_a, y_b*	*Size to be processed, default: 0, x-1, 0, y-1*
C_FLAG	*0*	*No calibration*
C_FLAG	*$1,x_1,y_1,\Delta x,\Delta y$*	*1 reference region, location, x1,y1 size $\Delta x,\Delta y$*
C_FLAG	*$2,x_1,y_1,x_2,y_2,\Delta x,\Delta y$*	*2 reference regions, locations, x1,y1,x2,y2 size $\Delta x,\Delta y$*
C_FLAG	*10*	*Average set to zero*
R_FLAG	*0*	*No regularization*
R_FLAG	*$1,\lambda$*	*Zero order regularization*
R_FLAG	*$2,\lambda$*	*First order regularization*
R_FLAG	*$3,\lambda$*	*Second order regularization*
T_FLAG	*0*	*No topographic correction*
T_FLAG	*1*	*Topographic correction*
I_FLAG	*0*	*No interactive mode*
I_FLAG	*1*	*Interactive mode*
I_FLAG	*2, par.txt*	*Process par.txt file*
I_FLAG	*3*	*Save everything in text file*
SET	*hhmmss, θ, φ, set.txt*	*Time of acquisition, azimuth and incidence angle, file containing data for each dataset*

Table 3-6 MSBAS parameters defined within the header.txt file. x and y are width and length of input interferograms, x_a, x_b, y_a, y_b are first and last columns and rows of input data to be processed. x_i and y_i are column and row number for each number of *i* reference regions, Δx and Δy are half-width/length of reference region/s, λ is regularization parameter, hhmmss is acquisition time for each dataset, θ is azimuth angle, φ is incidence angle in degrees, modified after (Samsonov & D'Oreye, 2017)

```
FORMAT = 1
FILE_SIZE = 2458, 2115
WINDOW_SIZE = 0, 2457, 0, 2114
R_FLAG = 1, 0.04
C_FLAG = 10
T_FLAG = 0
I_FLAG = 2, par.txt
SET = 122454, -168.8102258, 26.1456, dsc.txt
SET = 001844, -12.7560756, 39.2765, asc.txt
```

Table 3-7 Example MSBAS header.txt file used in this study

The discussion above provides a detailed description for each parameter used in the MSBAS software. If a pair of ascending and descending datasets are used, following the guidelines above, two-dimensional surface deformation will be generated. However, if a single descending or ascending dataset is used, then the two-dimensional deformation can no longer be computed. Instead, a modified SBAS approach is applied and only the line-of-sight deformation results are calculated. This methodology is discussed in Samsonov et al. (2011), whereby a linear least squares inversion is used to calculate deformation time series as well as mean and linear deformation rates.

3.3.2   MSBAS Outputs

Outputs of the MSBAS software consists of individual files of two-dimensional (east-west and vertical) cumulative surface deformation rate maps for each acquisition epoch. Due to the polar orbit of space-borne satellites, ground motion in the north-south direction is not well resolved, and therefore not considered in the MSBAS algorithm. Also output are two-dimensional annual linear deformation rates, which are found by fitting a line to the time series. However, for some applications, linear deformation rates may be misleading so should be interpreted with caution (Samsonov & D'Oreye, 2017). Time series for selected points within the *par.txt* are also generated with MSBAS, providing two-dimensional cumulative deformation values.

Chapter 4

4 DInSAR and Time Series Results

4.1 DInSAR Interferograms

In order to produce spatially and temporally accurate MSBAS time series analysis results, highly coherent differential interferograms are required. This section presents differential interferograms that were generated using the procedure described in Chapter 3.2 for each satellite used in this dataset: RADARSAT-2, ALOS PALSAR, Sentinel-1A and ALOS-2.

4.1.1 RADARSAT-2

Using 29 descending RADARSAT-2 SAR frames over the region shown in Figure 4-1, 407 differential interferograms were generated.

Figure 4-1 Outline of RADARSAT-2 wide frames (black outline) used in this study, in relation to injection disposal wells (black squares) and 2012 Timpson earthquake (red star).

Figure 4-2 Wrapped, geocoded differential interferograms for successive acquisitions of RADARSAT-2 spanning 6 March 2014 to 20 November 2015. Background intensity map is exposed for incoherent regions. Interferograms have been multilooked (3 in range, 10 in azimuth) and filtered. Dates in YYYYMMDD format. Colour scale represents the wrapped interval between 0 and 2π, with each full cycle equivalent to 28 mm deformation (half the RADARSAT-2 wavelength).

Figure 4-3 Wrapped, geocoded differential interferograms for successive acquisitions of RADARSAT-2 spanning 20 November 2015 to 14 March 2017. Background intensity map is exposed for incoherent regions. Interferograms have been multilooked (3 in range, 10 in azimuth) and filtered. Dates in YYYYMMDD format. Colour scale represents the wrapped interval between 0 and 2π, with each full cycle equivalent to 28 mm deformation (half the RADARSAT-2 wavelength).

Figure 4-2 and Figure 4-3 presents selected RADARSAT-2 differential interferograms for subsequent time steps from March 2014 to March 2017. Most of the interferograms shown here are highly coherent due to the small temporal baseline (the amount of time between acquisitions), whereby most pixels have consistent scattering properties between acquisitions. However, as the temporal baseline increases, coherence decreases. For example, the interferogram *20140821 - 20150512* is highly decorrelated due to the large time period between acquisitions, and the scattering properties of the surface have significantly changed, causing decorrelation. On the other hand, the interferogram *20150629 – 20150723* is highly decorrelated despite having a temporal baseline of only a few weeks. This decorrelation could be explained by other decorrelation factors as discussed in Chapter 1.4.4, for example atmospheric or thermal effects, affecting the phase contribution to interferometric phase.

All interferograms were masked by removing incoherent pixels that did not meet a coherence threshold. In Figure 4-2 and Figure 4-3 pixels with coherence less than 0.2 were removed, exposing the background intensity image. This exposes large incoherent regions in the interferogram, highlighting two major lake features, which remain decorrelated in all interferograms. Masking these pixels is essential when unwrapping the interferometric phase, to ensure unwrapping is done as accurately as possible. However, this causes discontinuities in the interferometric phase, which can also cause problems during unwrapping, affecting surface deformation interpretations (Hooper & Zebker, 2007).

However, from Figure 4-2 and Figure 4-3 it is also clear there are some features in the interferometric wrapped phase that may cause problems when interpreting surface deformation. First, atmospheric artefacts are a large source of errors in DInSAR analysis and this is evident in interferograms used in this study. For example, the interferogram *20140704 – 20140728* shows a broad region of phase change over the study area, at least three interference fringes corresponding to ~8 cm surface deformation. However, upon further inspection this large signal represents atmospheric signal (S. Samsonov, personal communication, July 2017). This atmospheric effect will alter surface deformation measurements, affecting any interferogram that covers the time period when this

atmospheric effect took place. Second, residual orbital errors can cause problems when interpreting surface deformation. In Figure 4-2 and Figure 4-3 residual orbital errors can be seen in some interferograms. For example, a large vertical, linear feature can be seen in pairs 20140517 – 20140610 (Figure 4-2) and 20170125 – 20170218 (Figure 4-3), a product of orbital errors that propagate directly into interferometric phase errors within the differential interferogram (Hanssen, 2001). These errors in interferometric phase affect surface deformation interpretations and must be accounted for prior to MSBAS processing, often through the removal of obviously affected interferograms.

Overall, most of the RADARSAT-2 differential interferograms with small temporal baselines (less than a couple of months) remain coherent. Therefore, a large stack of high quality differential interferograms are available for MSBAS time series processing.

4.1.2   ALOS PALSAR

After mosaicking ALOS track 172, as discussed in Chapter 3.2, differential interferograms were generated for two sets of overlapping frames over the study area shown in Figure 4-4.
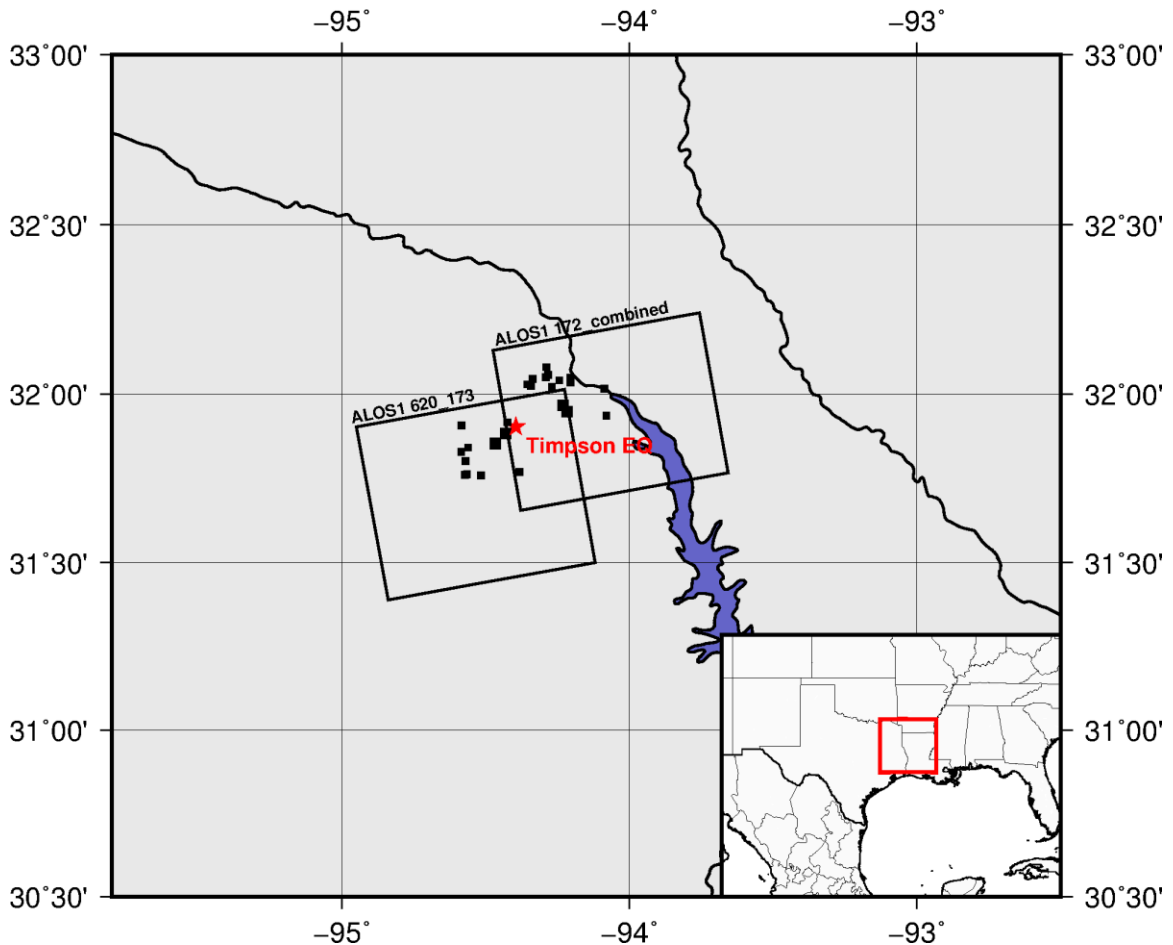
Figure 4-4 Outline of two ALOS PALSAR tracks (black outlines) used in this study (ALOS 620_173 and ALOS 172_combined), in relation to injection disposal wells (black squares) and 2012 Timpson earthquake (red star).

In total, 118 differential interferograms were generated for combined track 172 and 89 differential interferograms for the 620_173 track. Figure 4-5 shows a set of differential interferograms for the combined track_172 and Figure 4-6 shows a set of differential interferograms for track 620_173.
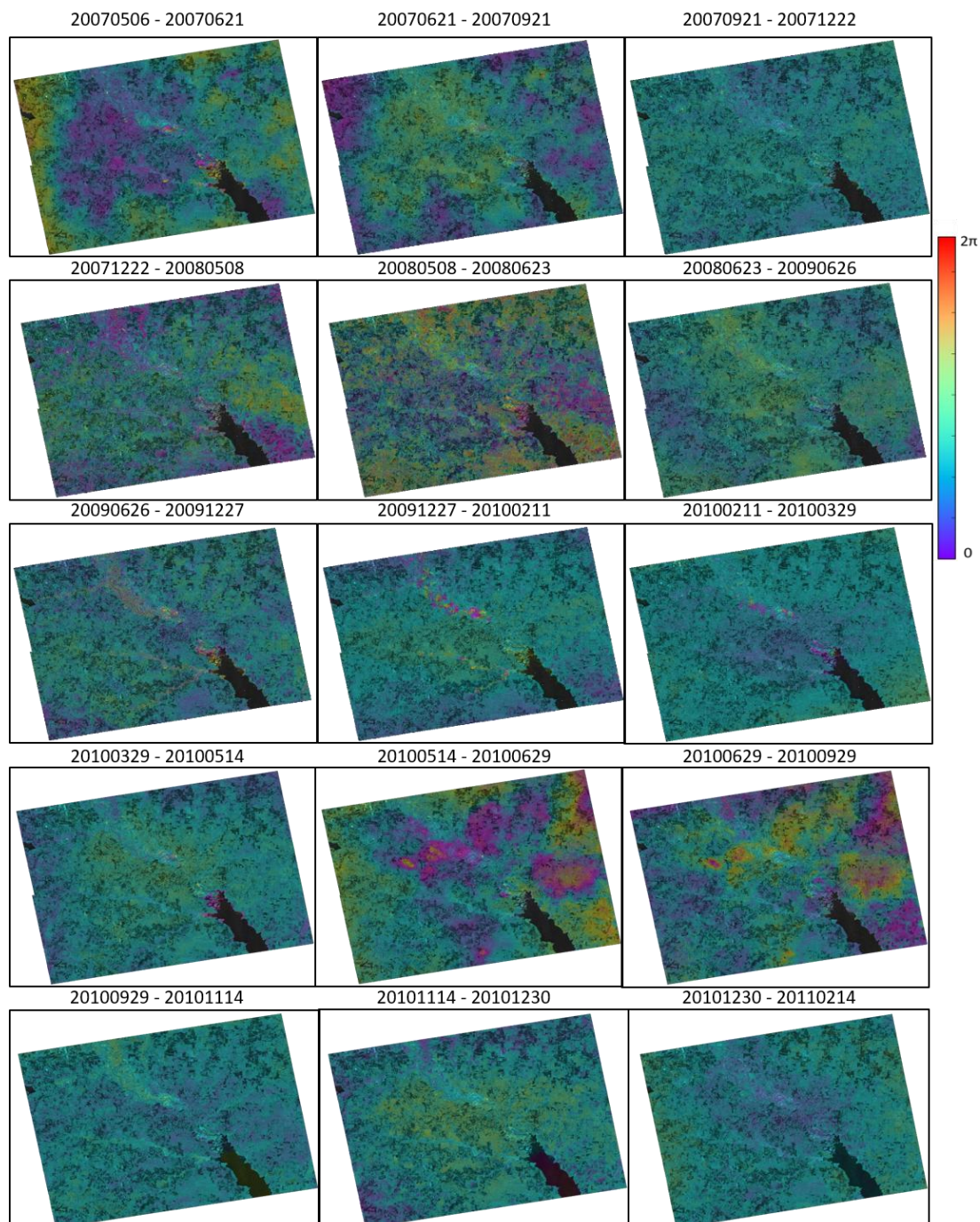
Figure 4-5 Wrapped, geocoded differential interferograms for successive acquisitions of ALOS combined track 172 combined from 6 May 2007 to 14 February 2011. Background intensity map is exposed for incoherent regions. Interferograms have been multilooked (6 in range, 10 in azimuth) and filtered. Dates in YYYYMMDD format. Colour scale represents the wrapped interval between 0 and 2π, with each full cycle equivalent to 120 mm deformation (half the ALOS wavelength).
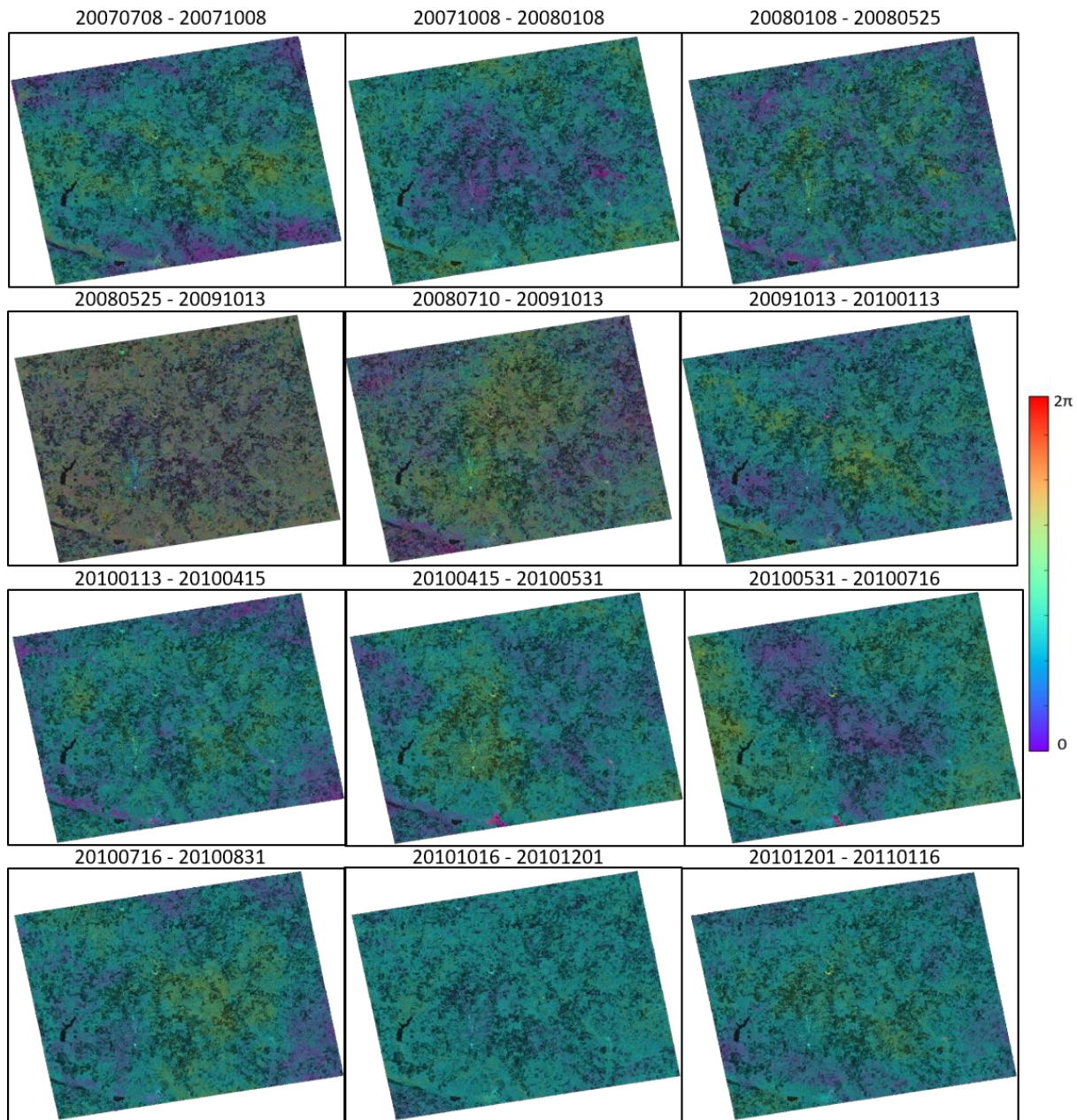
Figure 4-6 Wrapped, geocoded differential interferograms for successive acquisitions of ALOS track 620_173 from 8 July 2007 to 16 January 2011. Background intensity map is exposed for incoherent regions. Interferograms have been multilooked (6 in range, 10 in azimuth) and filtered. Dates in YYYYMMDD format. Colour scale represents the wrapped interval between 0 and 2π, with each full cycle equivalent to 120 mm deformation (half the ALOS wavelength).

Both ALOS tracks cover separate regions of the study area, track 172 covering the eastern half and track 620_173 covering the western half. Although both tracks cover the same time period, mid-2007 to 2011, they only spatially overlap in a small region over the study area. This limits the amount of interpretation that can be performed using these satellite tracks compared to RADARSAT-2, which covers the entire region.

From Figure 4-5 and Figure 4-6, there is less decorrelation within the ALOS differential interferograms compared to RADARSAT-2, shown in Figure 4-3. This is due to the longer wavelength used by the ALOS sensor, 24 cm compared to 6 cm for RADARSAT-2. Longer wavelengths are able to penetrate vegetation and are less sensitive to changes in surface conditions over time (Wempen & McCarter, 2017). Therefore, in ALOS differential interferograms we can see good coherence in interferograms despite a longer repeat orbit than RADARSAT-2 (Table 3-1). However, longer sensor wavelengths used by ALOS are less sensitive to deformation per pixel compared to shorter wavelengths, like the C-band RADARSAT-2 sensor. This must also be considered when interpreting surface deformation by comparing differential interferograms from these satellites.

Figure 4-5 and Figure 4-6 also show that ALOS interferograms cover an older time period compared to RADARSAT-2. ALOS covers the time period mid-2007 to 2011, whereas RADARSAT-2 covers 2014 to 2017. Therefore, ALOS satellite provides additional information on the temporal evolution of surface deformation at Timpson.

Despite good phase coherence in the ALOS differential interferograms, the presence of orbital and atmospheric errors is evident. ALOS interferograms are significantly affected by orbital errors due to large perpendicular baselines (Figure 3-2 C-E), causing long wavelength linear features within interferograms. These orbital errors are corrected for during processing (Chapter 3.2.7), but similar to RADARSAT-2 interferograms, residual errors can remain and propagate through to the differential interferograms.

4.1.3   Sentinel-1A

Using 19 Sentinel-1A frames acquired over the study area, shown in Figure 4-7, 138 differential interferograms were generated following the TOPS mode processing steps discussed in Chapter 3.2.9. A sample of 16 of these differential interferograms are shown in Figure 4-8 and Figure 4-9.
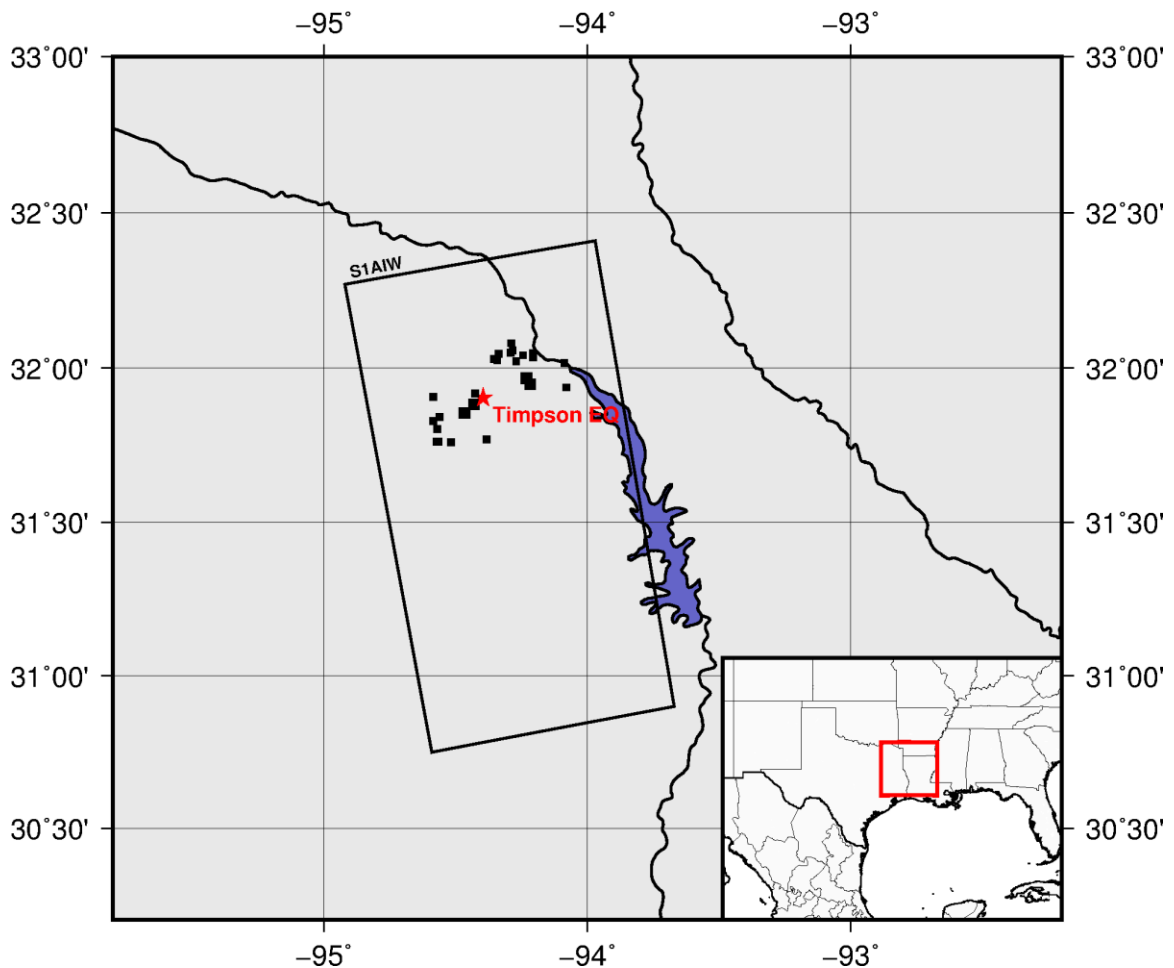
Figure 4-7 Outline of Sentinel-1A IW frames (black outline) used in this study, in relation to injection disposal wells (black squares) and 2012 Timpson earthquake (red star).
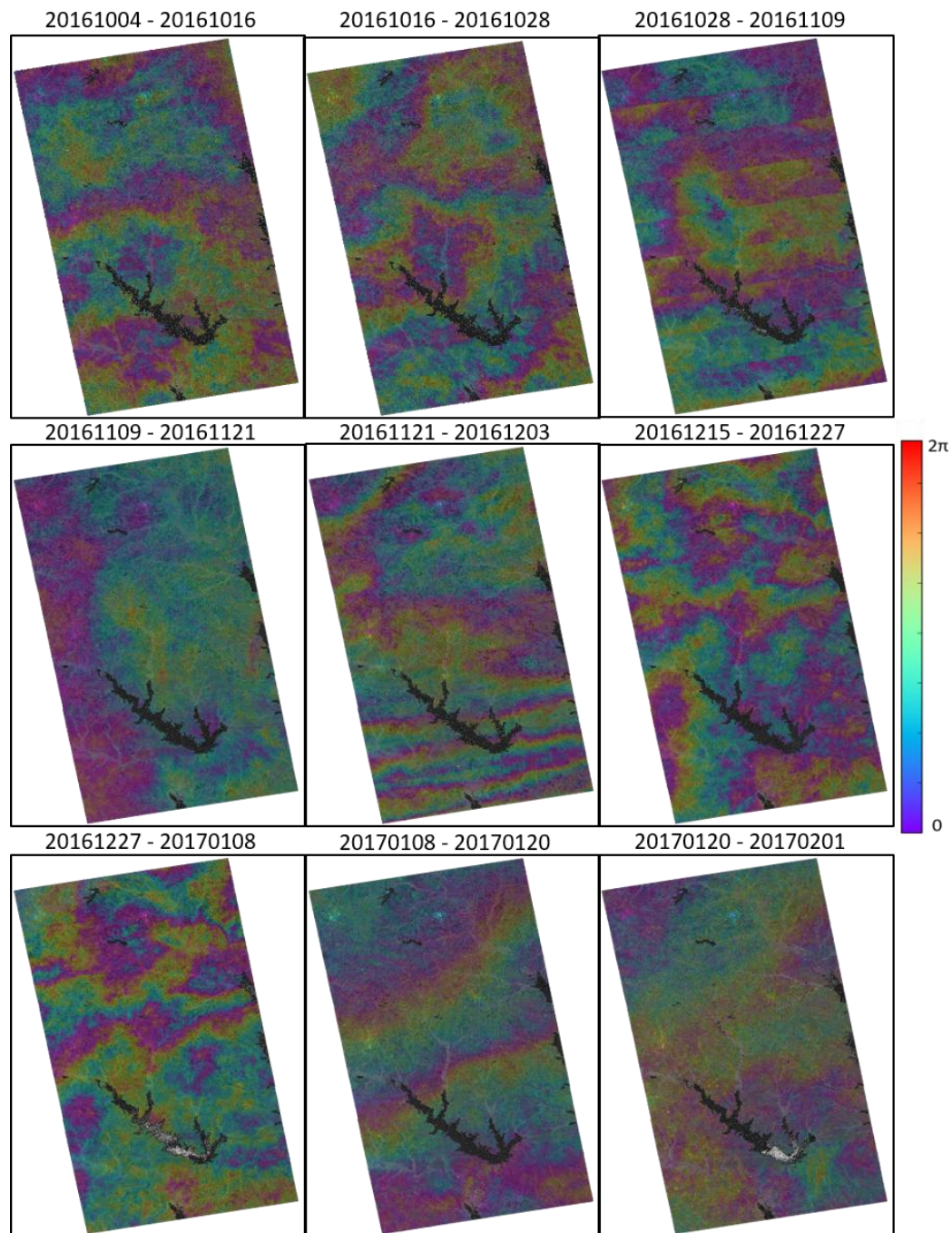
Figure 4-8 Wrapped, geocoded differential interferograms for successive acquisitions of Sentinel-1A from 4 October 2016 to 1 February 2017. Background intensity map is exposed for incoherent regions. Interferograms have been multilooked (12 in range, 2 in azimuth) and filtered. Dates in YYYYMMDD format. Colour scale represents the wrapped interval between 0 and 2π, with each full cycle equivalent to 28 mm deformation (half the Sentinel-1 wavelength).
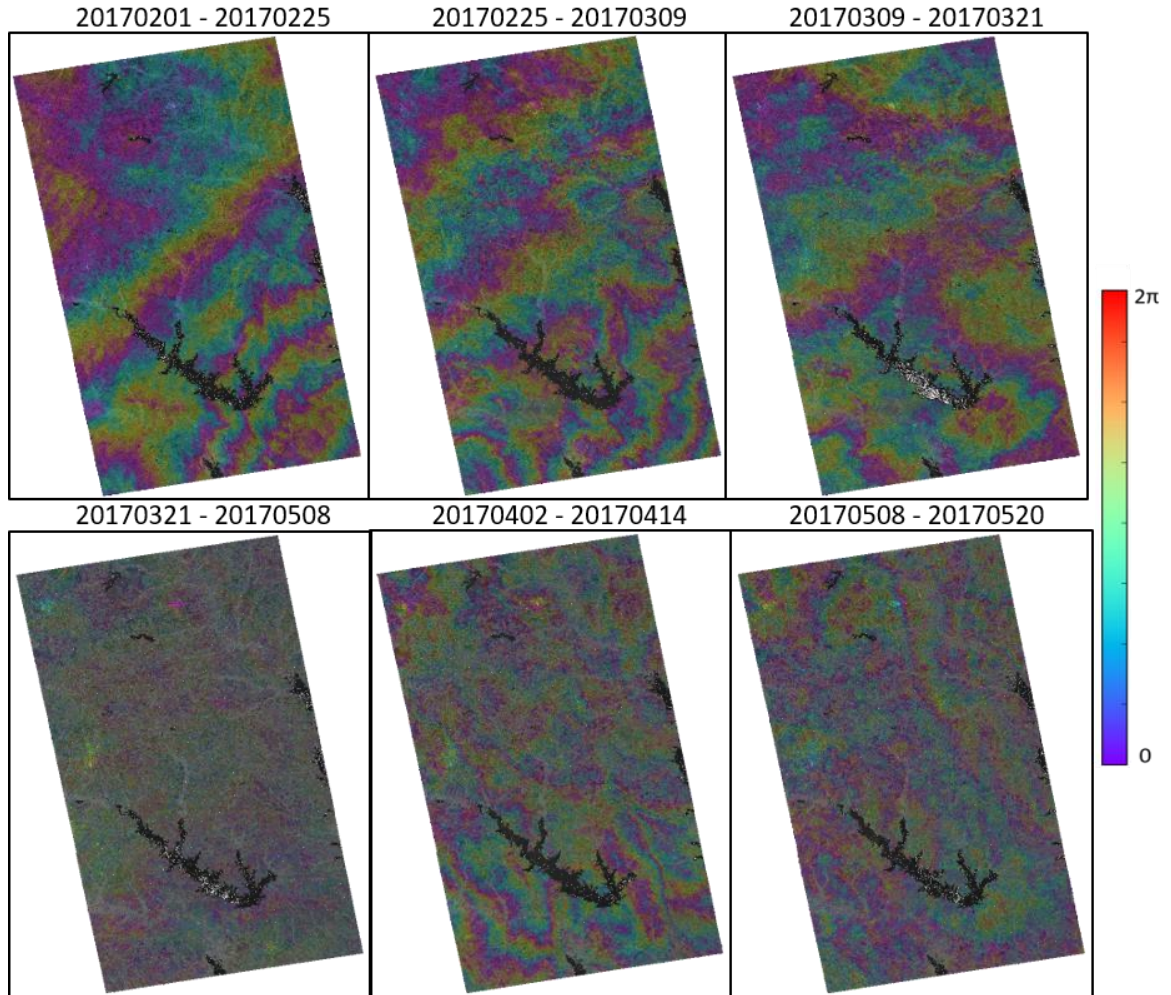
Figure 4-9 Wrapped, geocoded differential interferograms for successive acquisitions of Sentinel-1A from 1 February 2017 to 20 May 2017. Background intensity map is exposed for incoherent regions. Interferograms have been multilooked (12 in range, 2 in azimuth) and filtered. Dates in YYYYMMDD format. Colour scale represents the wrapped interval between 0 and 2π, with each full cycle equivalent to 28 mm deformation (half the Sentinel-1 wavelength).

Wrapped differential interferograms shown in Figure 4-8 and Figure 4-9 provide surface deformation information from late 2016 to mid-2017. For interferograms with small temporal baselines, coherence is good whereby the only decorrelated features are the lake bodies. However, for periods spanning around one month, for example in the interferogram 20170321 – 20170508, decorrelation increases and interferometric fringes

are less visible. Shorter wavelength sensors, such as the Sentinel-1A C-band decorrelate more rapidly over longer time periods compared to longer wavelength sensors such as the ALOS L-band sensor (Hanssen, 2001).

Also, similar to RADARSAT-2 and ALOS differential interferograms, residual orbital errors are evident within some Sentinel-1A images shown in Figure 4-8 and Figure 4-9. These long wavelength orbital ramps can be seen in the interferograms 20170201 – 20170225 and 20170108 – 20170120, and must be considered when interpreting surface deformation.

Unlike errors seen in RADARSAT-2 and ALOS interferograms, Sentinel-1A images are affected by phase jumps at burst boundaries due to processing errors during coregistration. An example of these phase jumps can be seen in the interferogram 20161028 – 20161109. These phase jumps are due to the mis-coregistration of two SAR images, which are not resampled at one thousandth of a single SLC pixel (equivalent to 2 cm azimuthal offset). These phase jumps cause problems during unwrapping, misrepresenting surface deformation.

4.1.4 ALOS-2

An additional three descending ALOS-2 images were acquired to compliment the current satellite dataset, over the study region shown in Figure 4-10. In total, three differential interferograms were generated from these SAR images and are shown in Figure 4-11.
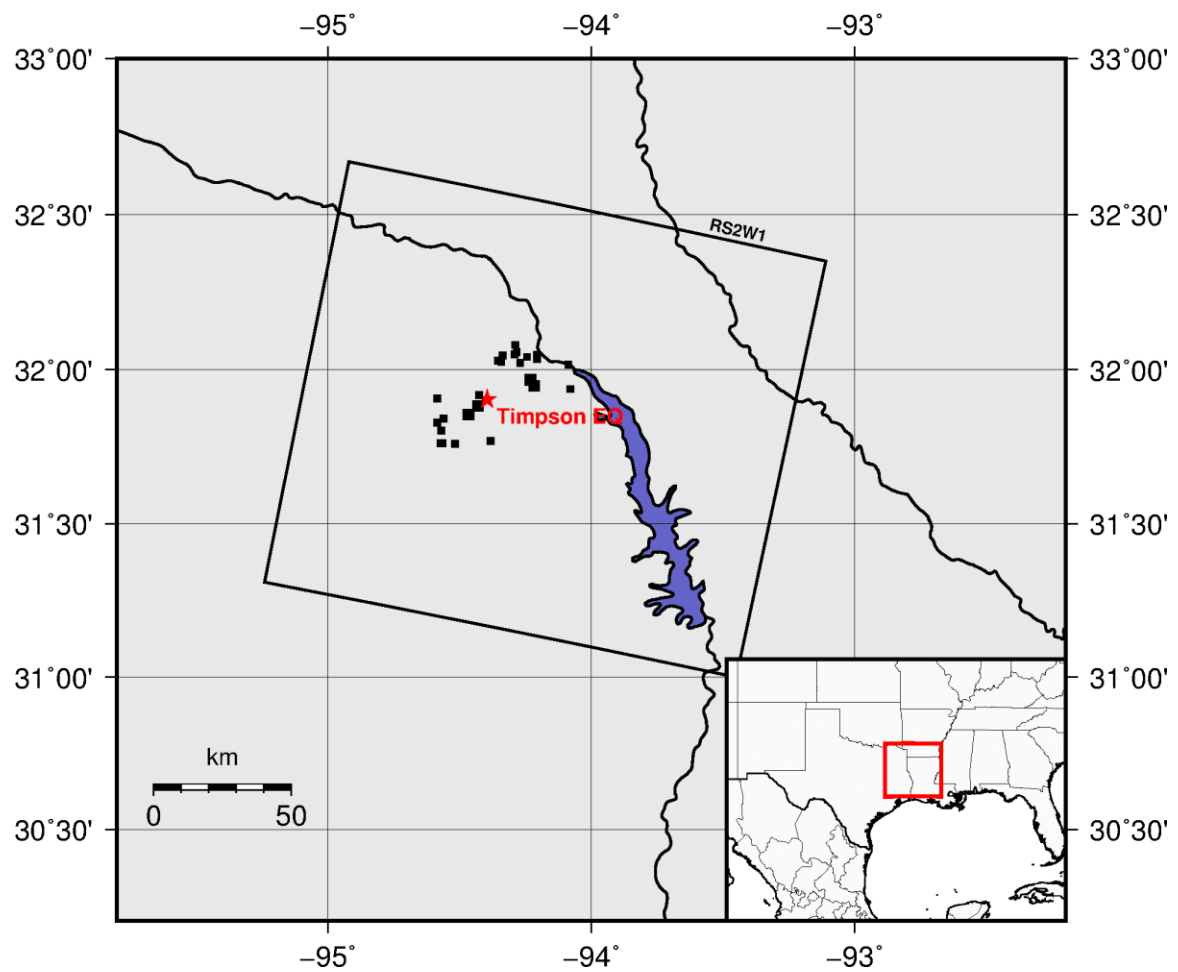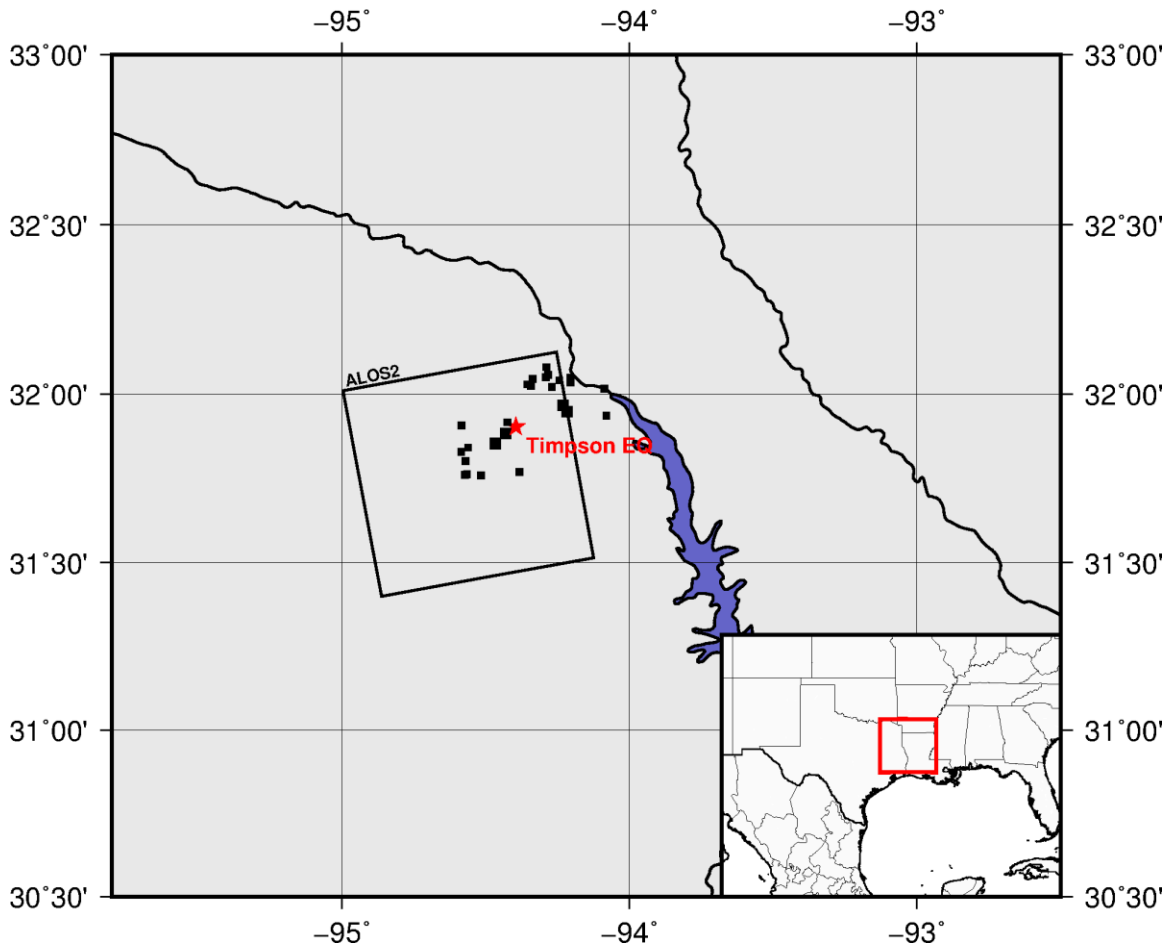

Figure 4-10 Outline of ALOS-2 FBD frames (black outline) used in this study, in relation to injection disposal wells (black squares) and 2012 Timpson earthquake (red star).
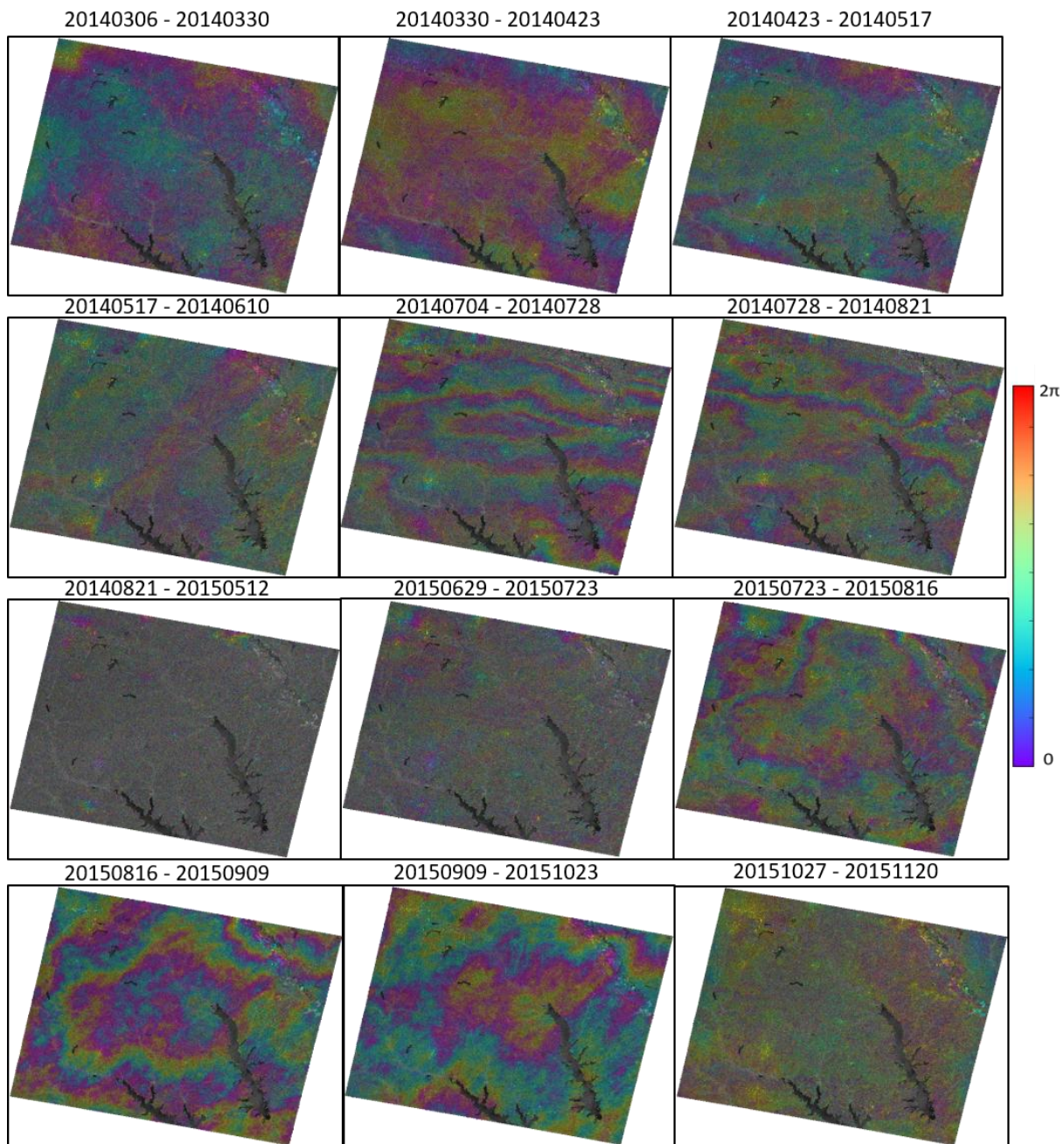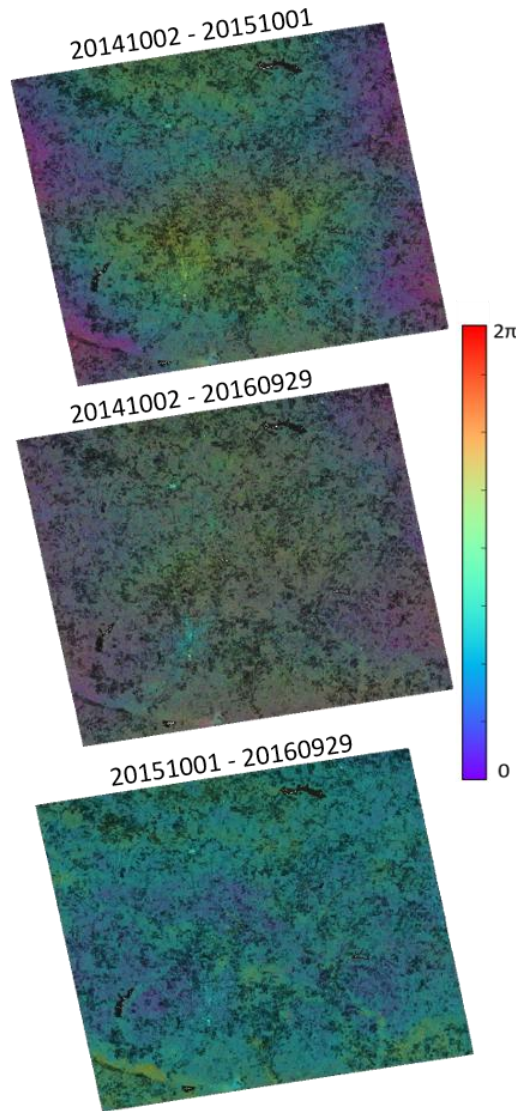
Figure 4-11 Wrapped, geocoded differential interferograms for successive acquisitions of ALOS-2 between 2 October 2014 to 29 September 2016. Background intensity map is exposed for incoherent regions. Interferograms have been multilooked (7 in range, 8 in azimuth) and filtered. Dates in YYYYMMDD format. Colour scale represents the wrapped interval between 0 and 2π, with each full cycle equivalent to 120 mm deformation (half the ALOS-2 wavelength).
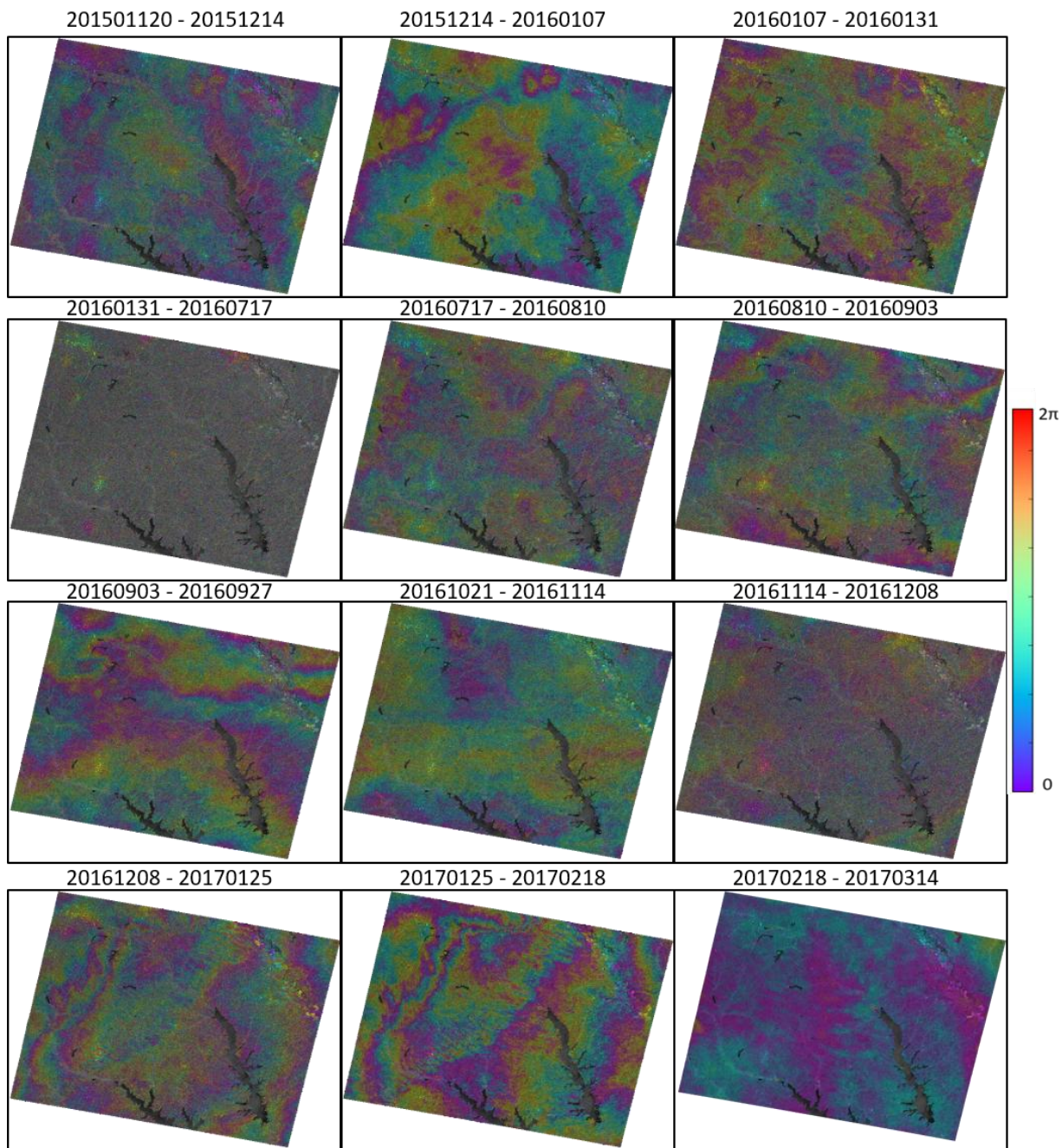
The wrapped differential interferograms shown in Figure 4-11 were geocoded from radar to map coordinates using the lookup table described in Chapter 3.2.8, with the colour scale representing surface motion in the wrapped interval between zero and 2π. It is clear

from these interferograms that coherence remains good even over long time periods, similar to ALOS-1 interferograms. This is due to the longer wavelength used by the ALOS-2 sensor (L-band) compared to the shorter wavelength used by RADARSAT-2 and Sentinel-1 (C-band). Longer wavelength sensors are less sensitive to temporal decorrelation and surface changes such as vegetation and are therefore useful for analysis of long time series. However, the small number of interferograms available limits analysis using ALOS-2 data. There are not enough data points to constrain an accurate time series of surface deformation using ALOS-2 interferograms alone.

4.2   SBAS RADARSAT-2

In order to provide a rough estimate of the scale and spatial distribution of surface deformation over our study area, SBAS time series analysis was first applied using RADARSAT-2 differential interferograms. RADARSAT-2 data was chosen because it covers the entire study area and provides deformation data from 2014 to present, with data collected at frequent (~24 day) intervals.

SBAS processing was performed using MSBAS software (Samsonov & D'Oreye, 2017), to compute LOS deformation rates over the selected study region covering the injection wells and seismicity at Timpson, TX.

Figure 4-12 shows the outline of the study area overlaying an example RADARSAT-2 differential interferogram indicating surface deformation spanning over one month.
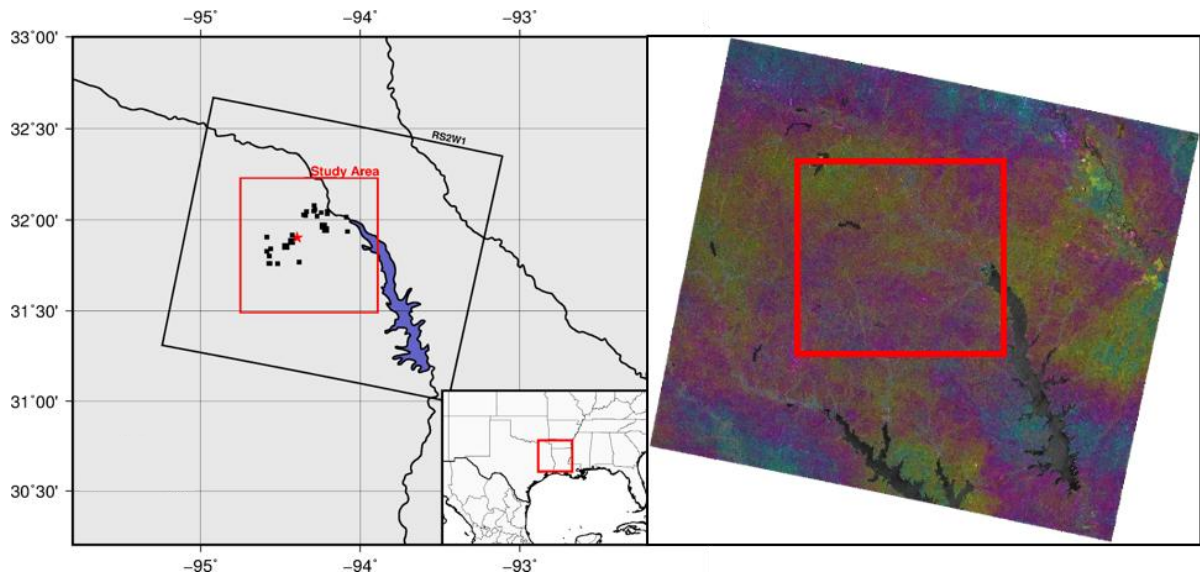
Figure 4-12 Left, study area investigated using SBAS analysis for the RADARSAT-2 descending path. The study area encompasses all the major and minor injection wells (black squares) and 2012 M4.8 earthquake (red star) at Timpson, TX. Right, example RADARSAT-2 differential interferogram *20140330 – 20140423* in relation to the study area (red square).

Prior to running MSBAS software, only high quality interferograms were selected based on a coherence threshold. In order to choose only high quality interferograms, I calculated the average coherence for a selected region on each interferogram. I selected this region in the center of the study area with a radius of 50 pixels. If the average coherence of these pixels was above 0.6, the interferogram was accepted for MSBAS processing, if it was below 0.6 it was removed.

Interferograms that also contained significant atmospheric or orbital signals were also removed. Each interferogram was individually analyzed to ensure no significant atmospheric or orbital errors were visible. As discussed in Chapter 1.4.4, many localized fringes represent atmospheric signal and long wavelength signals across the interferogram represents orbital errors.

Eighty-one RADARSAT-2 differential interferograms met the coherence criteria, which were then resampled to a common grid in map coordinates with 20 m by 20 m grid spacing.

Table 4-1 shows the header file used in the MSBAS software containing the parameters used to compute the time series for RADARSAT-2. Using a window size of 4779 by 4112 pixels, the calibration (C_FLAG) of each interferogram was set to zero, in order to gain an estimate on the scale and distribution of deformation. No topographic correction and zero order regularization were applied to this descending dataset.

```
FORMAT = 1
FILE_SIZE = 4779, 4112
WINDOW_SIZE = 0, 4778, 0, 4111
R_FLAG = 1, 0.15
C_FLAG = 10
T_FLAG = 0
I_FLAG = 2, par.txt
SET = 122454, -168.8102258, 26.1456, dsc.txt
```

Table 4-1 SBAS header file containing the parameters used for the RADARSAT-2 descending track. See Table 3-6 for definition of each parameter

SBAS cumulative LOS displacements for RADARSAT-2 are shown in Figure 4-13 for nine selected time steps from April 2014 to March 2017. Ground deformations above 3 cm were clipped to better represent ground deformation and remove anomalous points. Images were also masked using an average coherence image (Figure 3-7). Background intensity image is exposed where the coherence of a pixel is less than 0.3 on the average coherence image, exposing incoherent features such as lakes and riverbeds.

Red colours in Figure 4-13 indicate motion towards the satellite, which can be interpreted as surface uplift, whereas blue indicates motion away, or surface subsidence. Also, Figure 4-14 shows the LOS linear deformation rate from March 2014 to March 2017 computed by fitting a linear trend to the surface deformation time series. Deformation rate is presented in cm per year and the error associated with the linear LOS displacement rate map is shown in Figure 4-15. Four points were also selected across the study area,

highlighted *P1*, *P2*, *P3* and *P4* in Figure 4-13, with each deformation time series shown in Figure 4-16.
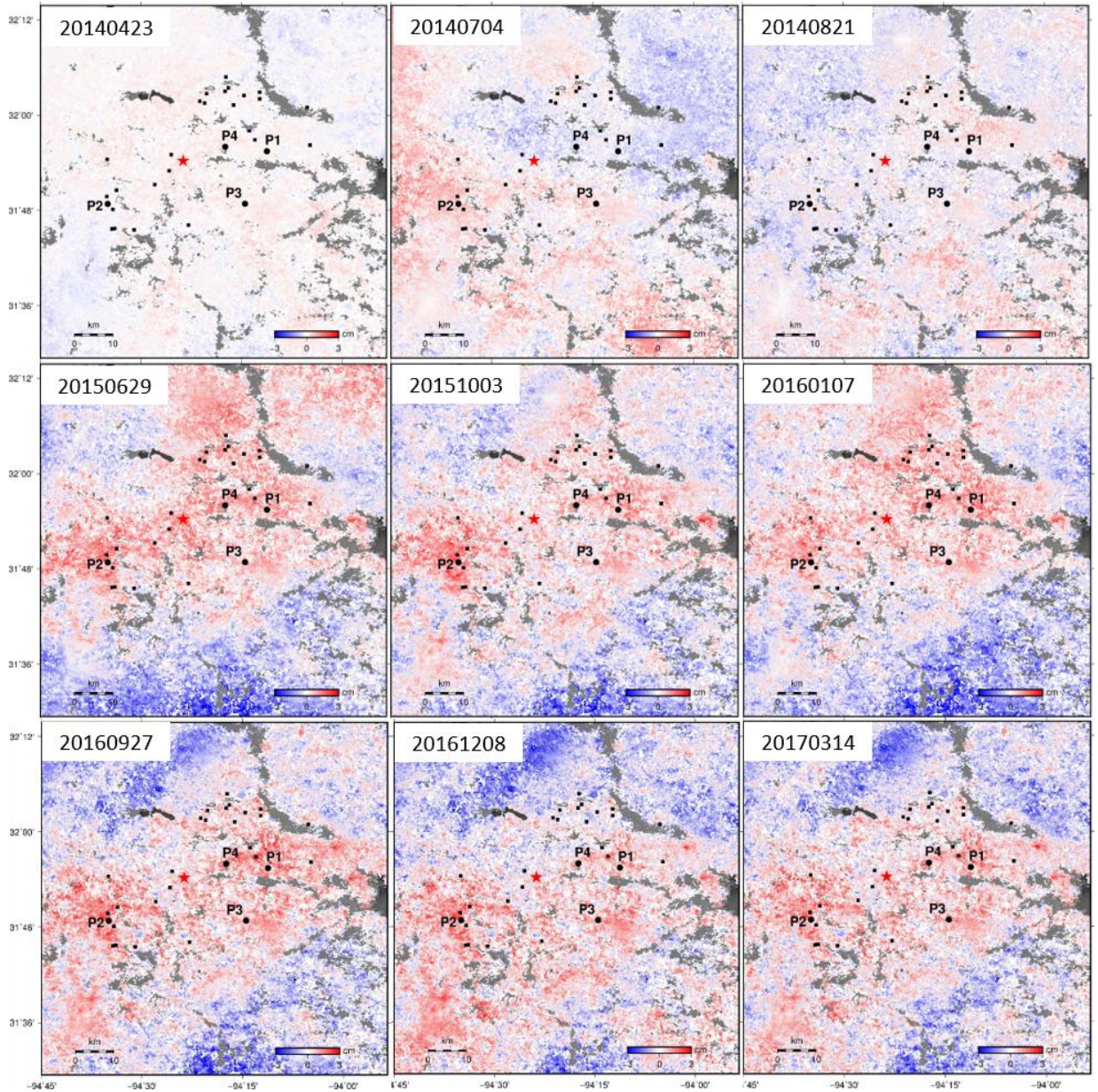
Figure 4-13 RADARSAT-2 modified SBAS cumulative LOS displacements at Timpson, TX between April 2014 and March 2017. Injection wells (black squares) and 2012 M4.8 EQ (red star) are labelled for reference. Also shown are four time series points, *P1*, *P2*, *P3* and *P4* (black circles). Displacements in cm.

Figure 4-13 shows the cumulative LOS deformation over a three-year period, with a large region of uplift centered in the middle of the study area. This area of uplift, encompasses all the injection wells and seismicity surrounding Timpson. Time series points *P1* to *P4* (Figure 4-16) indicate maximum LOS deformation up to 1.5 cm. Between April and July 2014, uplift is focussed towards the west wells before September 2014 where uplift begins in the east. However, during the large temporal jump between 21 October 2014 and 29 June 2015, uplift significantly increases across the entire study area surrounding the well injection locations. From June 2015 onwards, cumulative surface deformation does not change significantly up until the last period of deformation in March 2017.
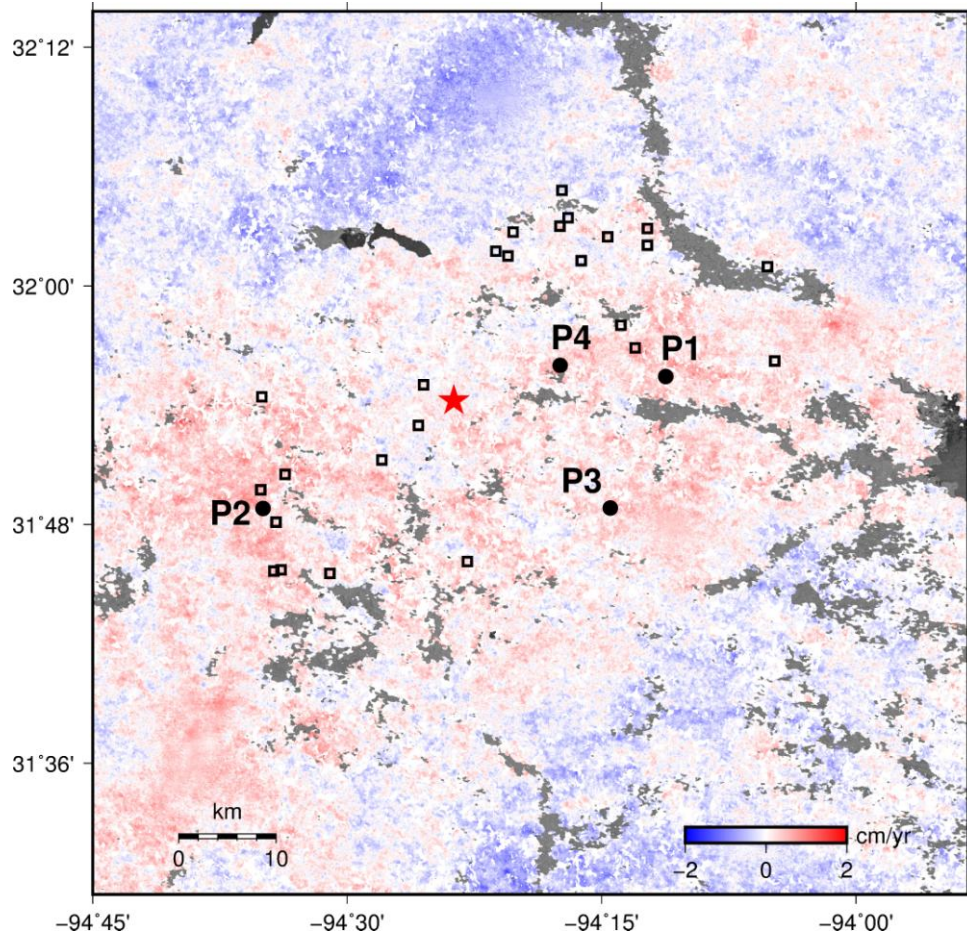
Figure 4-14 Linear LOS displacement rates calculated by fitting a linear trend to time series for RADARSAT-2 descending track at Timpson, TX. Injection wells (squares) and 2012 M4.8 EQ (red star) are labelled for reference. Also shown are four time series points, *P1*, *P2*, *P3* and *P4*. Displacement rates in cm/yr.

96

The linear LOS displacement rates shown in Figure 4-14 confirm that the fastest rates of surface uplift are located in the center of the study area. Combined, the area of uplift indicated from Figure 4-13 and Figure 4-14 is around ~300 km^2. However, Figure 4-14 suggests there are two separate regions of uplift, one surrounding the eastern and one surrounding the western injection wells. The red shade indicates around 1 to 1.5 cm/year linear uplift rate computed for the three years of the RADARSAT-2 dataset. There are also regions represented in blue surrounding the area of uplift, suggesting subsidence.
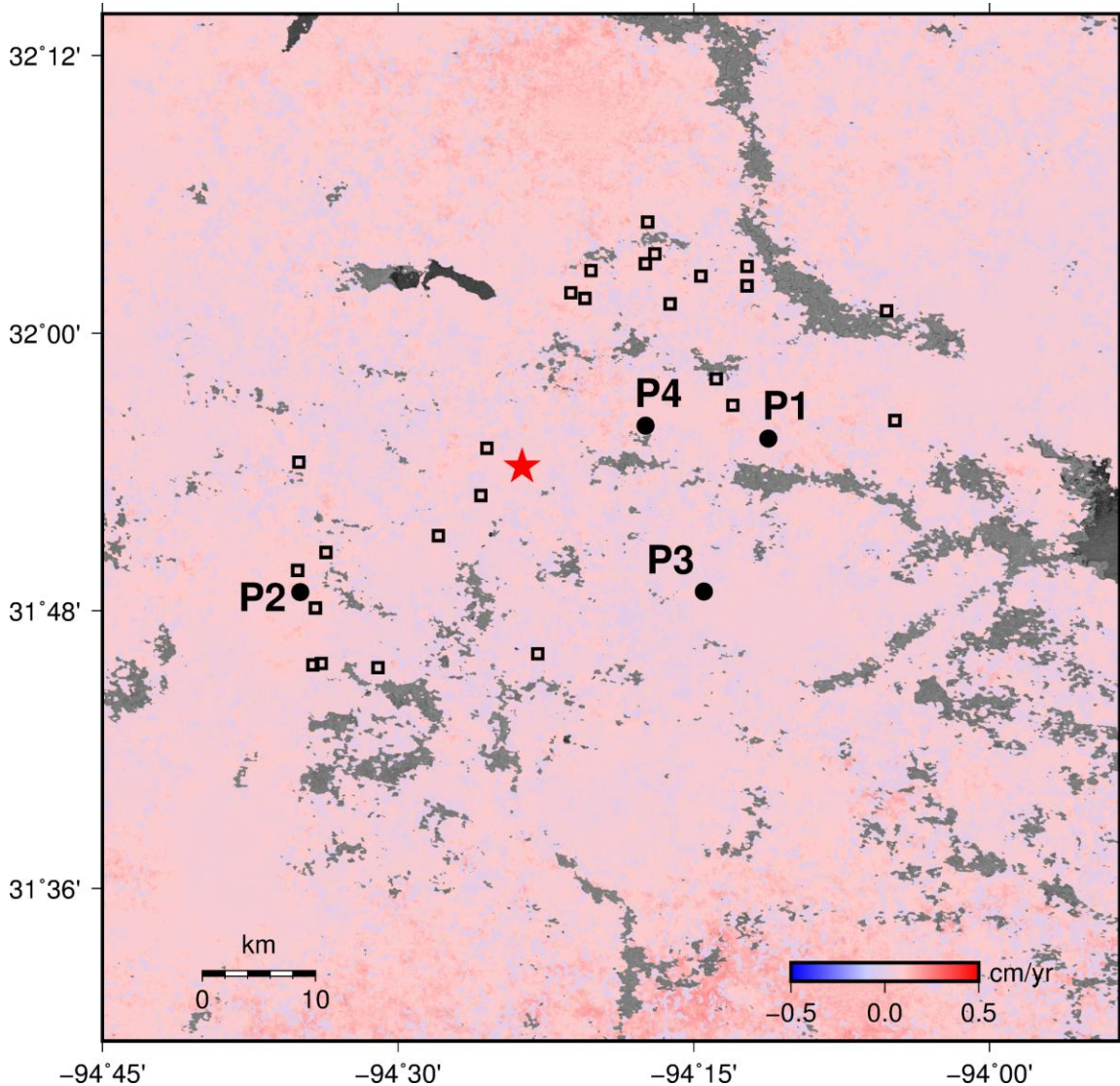
Figure 4-15 Error map**,** linear LOS displacement rates. Scale between -0.5 and 0.5 cm/yr. Injection wells (squares) and 2012 M4.8 EQ (red star) are labelled for reference. Also shown are four time series points, *P1*, *P2*, *P3* and *P4*.

The linear deformation rate error map shown in Figure 4-15 shows that the error is around ±0.1 to 0.2 cm/year (or 1-2 mm/year).
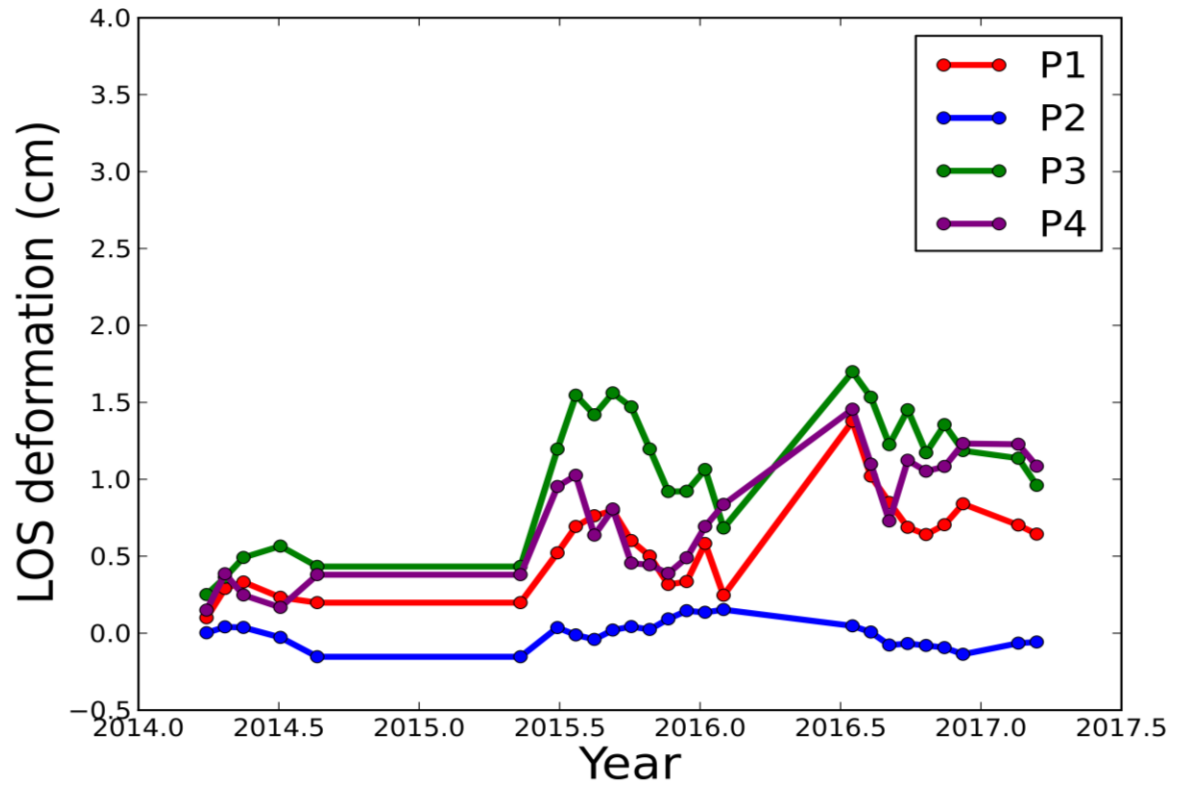
Figure 4-16 Time series of LOS displacements for selected pixels *P1*, *P2*, *P3* and *P4*, labelled in Figure 4-13.

Four time series points, *P1*, *P2*, *P3* and *P4* were selected in regions of uplift over the study area shown in Figure 4-16. The locations of these points can be seen in Figure 4-13 Figure 4-14. Points *P1*, *P2* and *P3* show similar patterns of deformation, with uplift up to 1.5 cm during similar time periods. Large jumps in displacement occur between observations with gaps within the dataset, shown by horizontal segments between October 2014 and May 2015. This is because there are no high quality differential interferograms, which span this period. For example, Figure 4-2 shows the interferogram *20140821-20150512* which has the smallest temporal baseline over this period and is completely decorrelated due to the nine month interval between RADARSAT-2 acquisitions. Also, point *P2* indicates uplift with lower magnitude compared to *P1*, *P2*

and *P3. P2* is located at the western edge of the study area, whereas the other three points are located around the eastern wells.

4.3　SBAS ALOS PALSAR

Similar to the RADARSAT-2 dataset, SBAS processing was performed using MSBAS software to create LOS surface deformation time series using ALOS PALSAR satellite. I performed SBAS on ALOS track 172_combined, which covers the majority of the injection wells and seismicity at Timpson, TX shown in Figure 4-17.
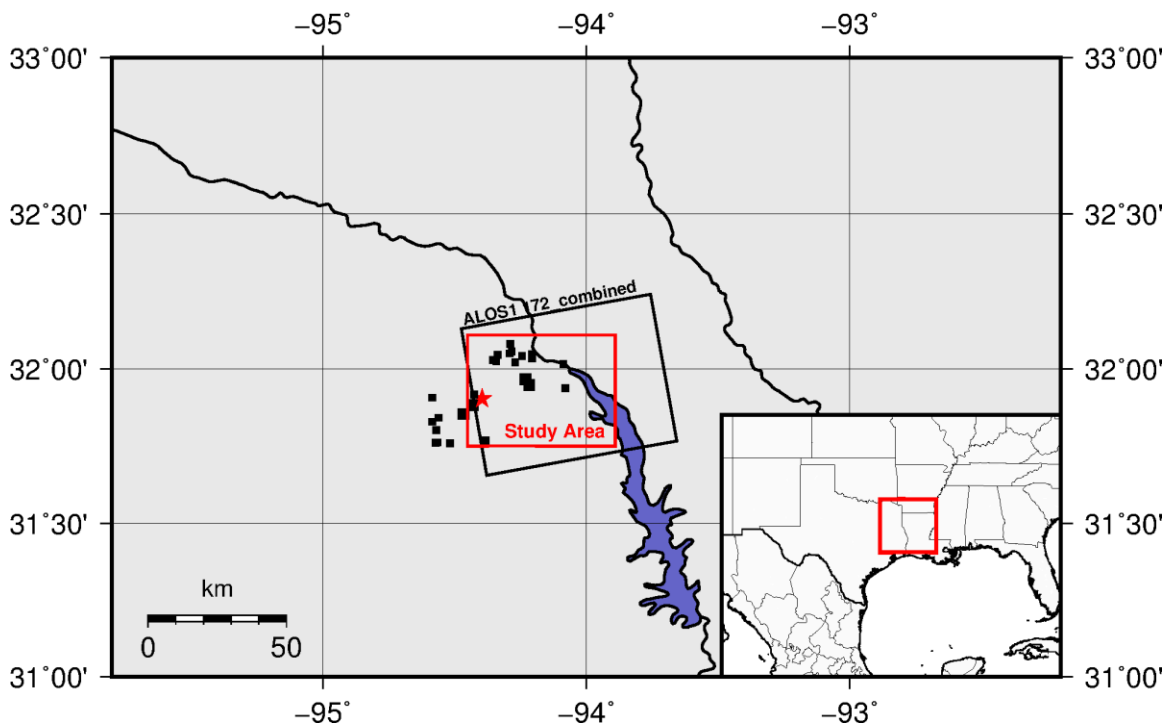
Figure 4-17 Study area investigated using SBAS analysis for the ascending ALOS PALSAR 172_combined track. These frames cover most of the study area, encompassing the major and minor injection wells (black squares) and 2012 M4.8 earthquake (red star) at Timpson, TX.

Similar to SBAS processing for RADARSAT-2, prior to running MSBAS software only high quality ALOS interferograms were selected based on a coherence threshold (above 0.6 for a selected region on each 172_combined interferogram). Also similar to SBAS processing for RADARSAT-2, individual interferograms were analyzed to remove

significant atmospheric and orbital signals. These differential interferograms were resampled to a common grid, 20 m by 20 m grid spacing and processed using MSBAS software. Table 4-2 shows the header file used in the MSBAS software containing the parameters used to compute the time series for ALOS. A window size of 3118 by 1995 pixels was processed over the study area, calibration of each interferogram was set to zero and no topographic correction was applied.

```
FORMAT = 1
FILE_SIZE = 3118, 1995
WINDOW_SIZE = 0, 3117, 0, 1994
R_FLAG = 1, 0.15
C_FLAG = 10
T_FLAG = 0
I_FLAG = 2, par.txt
SET = 120000, -10.2396352, 38.7115, asc.txt
```

Table 4-2 SBAS header file containing the parameters used for the ALOS 172_combined ascending track. See Table 3-6 for definition of each parameter.

SBAS cumulative LOS displacements for ALOS track 172_combined are shown in Figure 4-18 for six time steps between December 2007 and February 2011. Similar to RADARSAT-2, motions were clipped above 3 cm and masked using the average coherence, derived from the stack of ALOS 172_combined interferograms. The background ALOS intensity image is exposed in regions where coherence of a pixel is less than 0.5, typically around river systems. Red colours represent upwards motion towards the satellite, whereas blue represents motion away from the satellite.

The largest surface displacements are located around two time series points, *P1* and *P2,* located next to the two main eastern well E1 and E2. By November 2011, a region located near the site of the 2012 M4.8 earthquake has uplifted in addition to the region next to the main eastern wells.
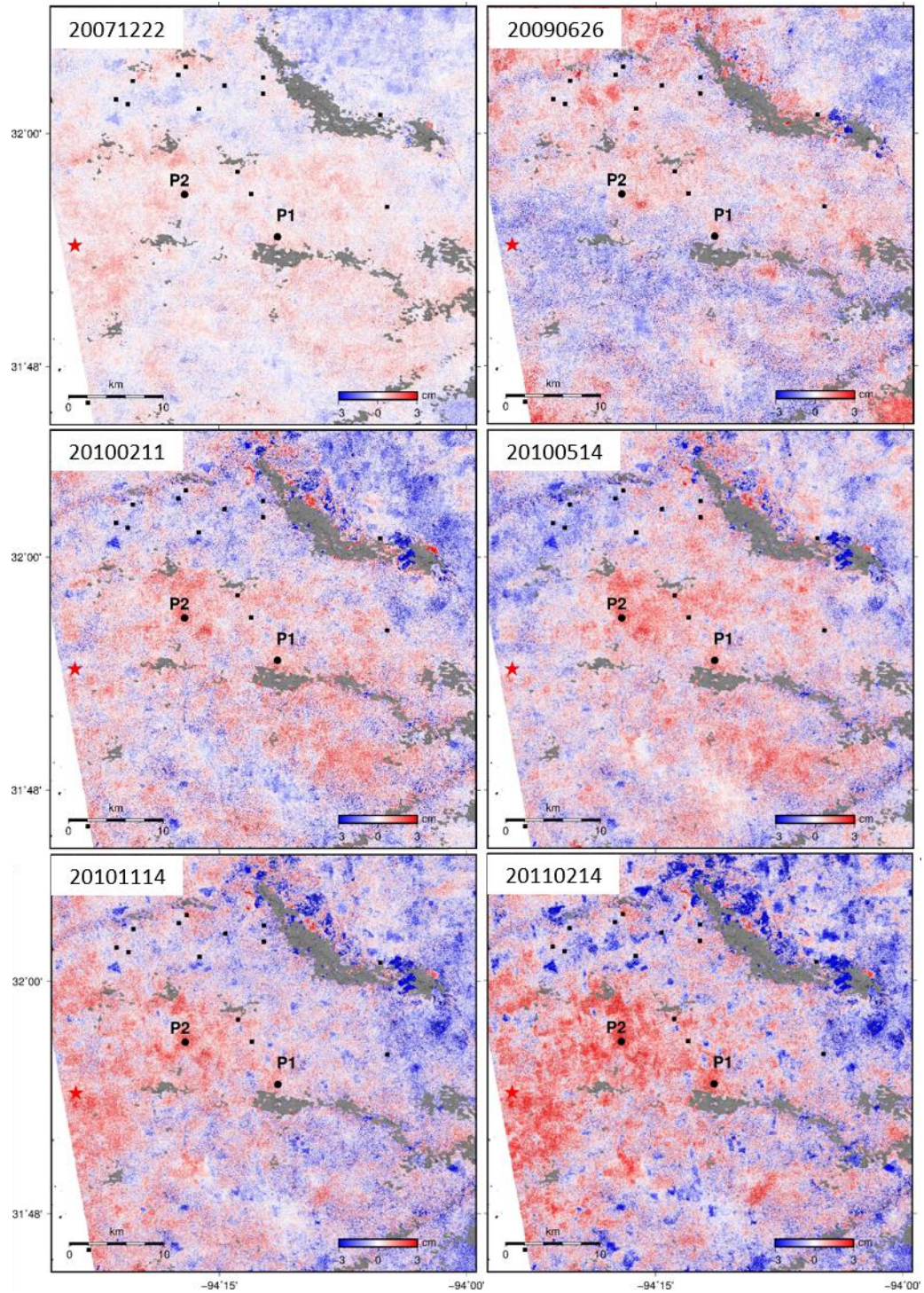
Figure 4-18 ALOS track 172_combined modified SBAS cumulative LOS displacements at Timpson, TX for selected time steps. Injection wells (black squares) and 2012 M4.8 EQ (red star) are labelled for reference. Also shown are two time series points, *P1* and *P2* (black circles). Displacements in cm.

Linear LOS displacement rates are shown in Figure 4-19 confirming the major regions of uplift are located near the two eastern wells E1 and E2. Surface displacement rates up to 1.5 cm/year can be seen around these regions.
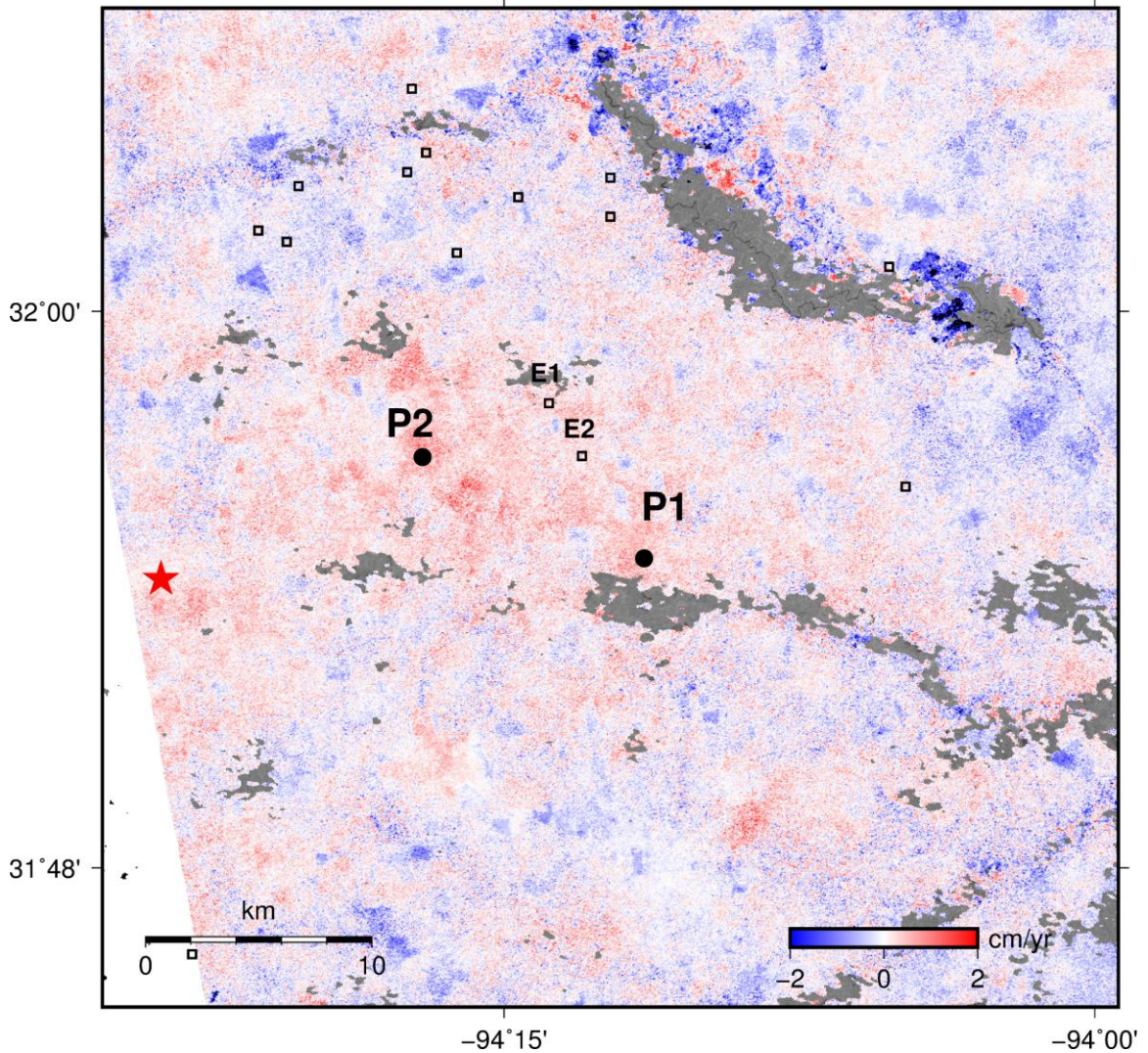
Figure 4-19 Linear LOS displacement rates calculated by fitting a linear trend to time series for ALOS track 172_combined descending track at Timpson, TX. Injection wells (squares) and 2012 M4.8 EQ (red star) are labelled for reference. Also shown are two time series points, *P1* and *P2*. Displacement rates in cm/yr.

The linear deformation rate error map shown in Figure 4-20 shows that the error is between 0 and 0.2 cm/year (or 1-2 mm/year). Regions with large amplitudes of uplift and subsidence surrounding the decorrelated regions in the north show large error, whereas errors in the center of the study region by wells E1 and E2 are low.
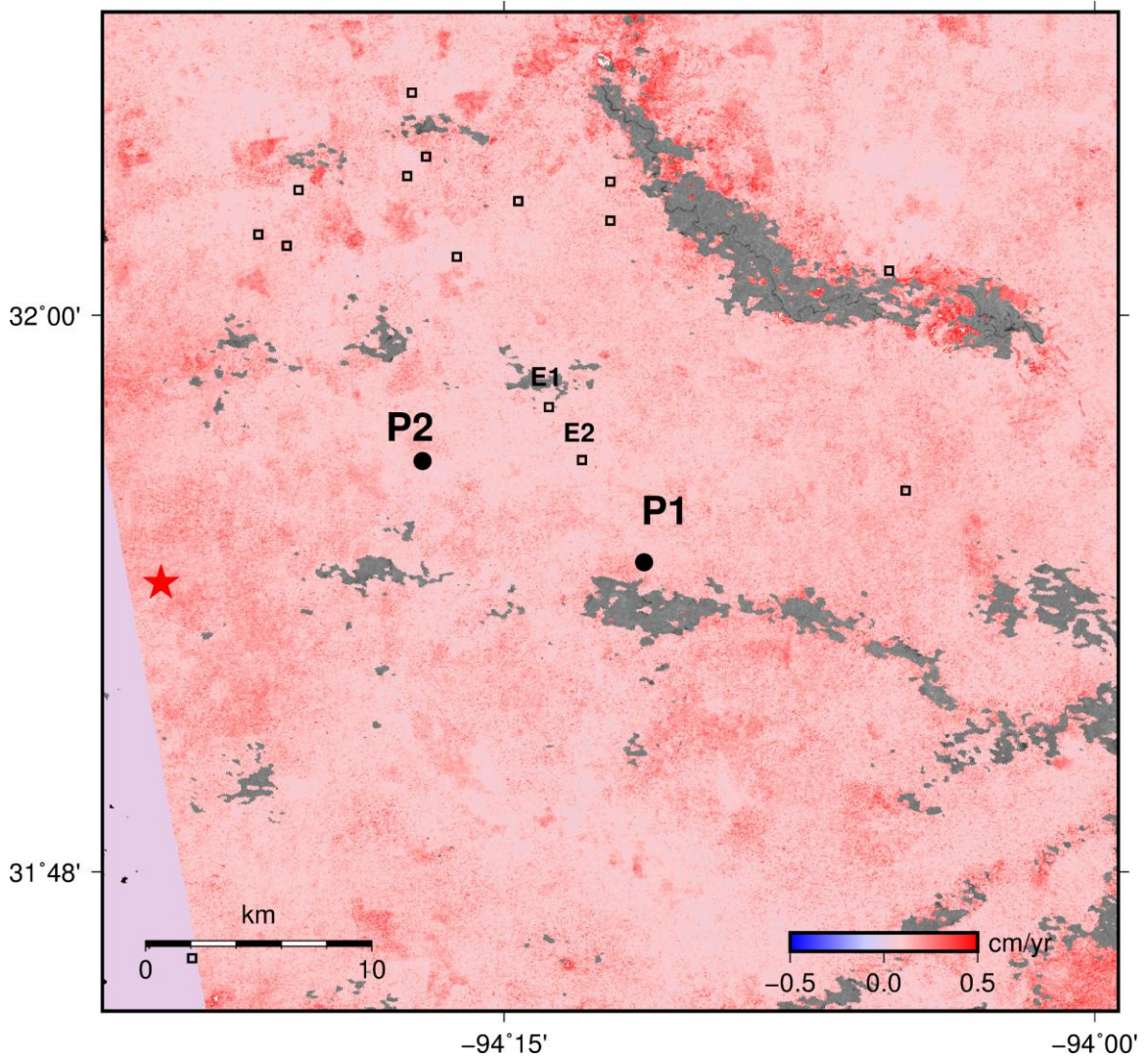
Figure 4-20 Error map, linear LOS displacement rates. Scale between -0.5 and 0.5 cm/yr. Injection wells (squares) and 2012 M4.8 EQ (red star) are labelled for reference. Also shown are two time series points, *P1* and *P2*.
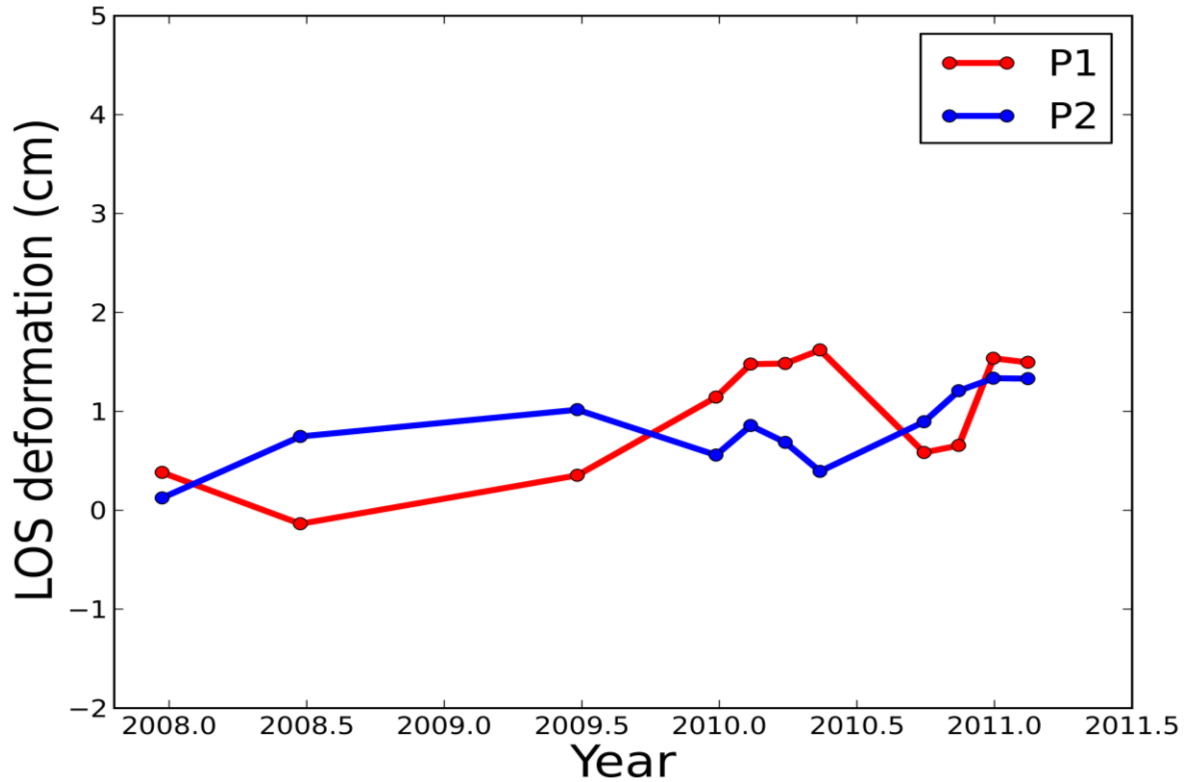
Figure 4-21 Time series of LOS displacements for selected pixels *P1* and *P2*, labelled in Figure 4-18.

Two time series points, *P1* and *P2* were selected close to the eastern wells E1 and E2 in regions of greatest uplift indicated by the ALOS SBAS results. Figure 4-21 shows the evolution of surface uplift from 2007 to 2011, with up to 1.5 cm maximum upwards LOS displacement at these points.

4.4   MSBAS RADARSAT-2 and Sentinel-1A

Previously in this chapter, only the one-dimensional LOS deformation time series were computed for a single dataset using SBAS processing. However, MSBAS utilizes overlapping, in time and space, ascending and descending DInSAR data to compute two-dimensional deformation time series.

MSBAS processing was performed using ascending Sentinel-1A and descending RADARSAT-2 datasets. These are the only two overlapping ascending and descending datasets which cover the entire study area and provide information on the most recent period of deformation. Figure 4-22 shows the outline of the Sentinel-1A and RADARSAT-2 frames and the study area used for MSBAS processing which encompasses all wells and seismicity.
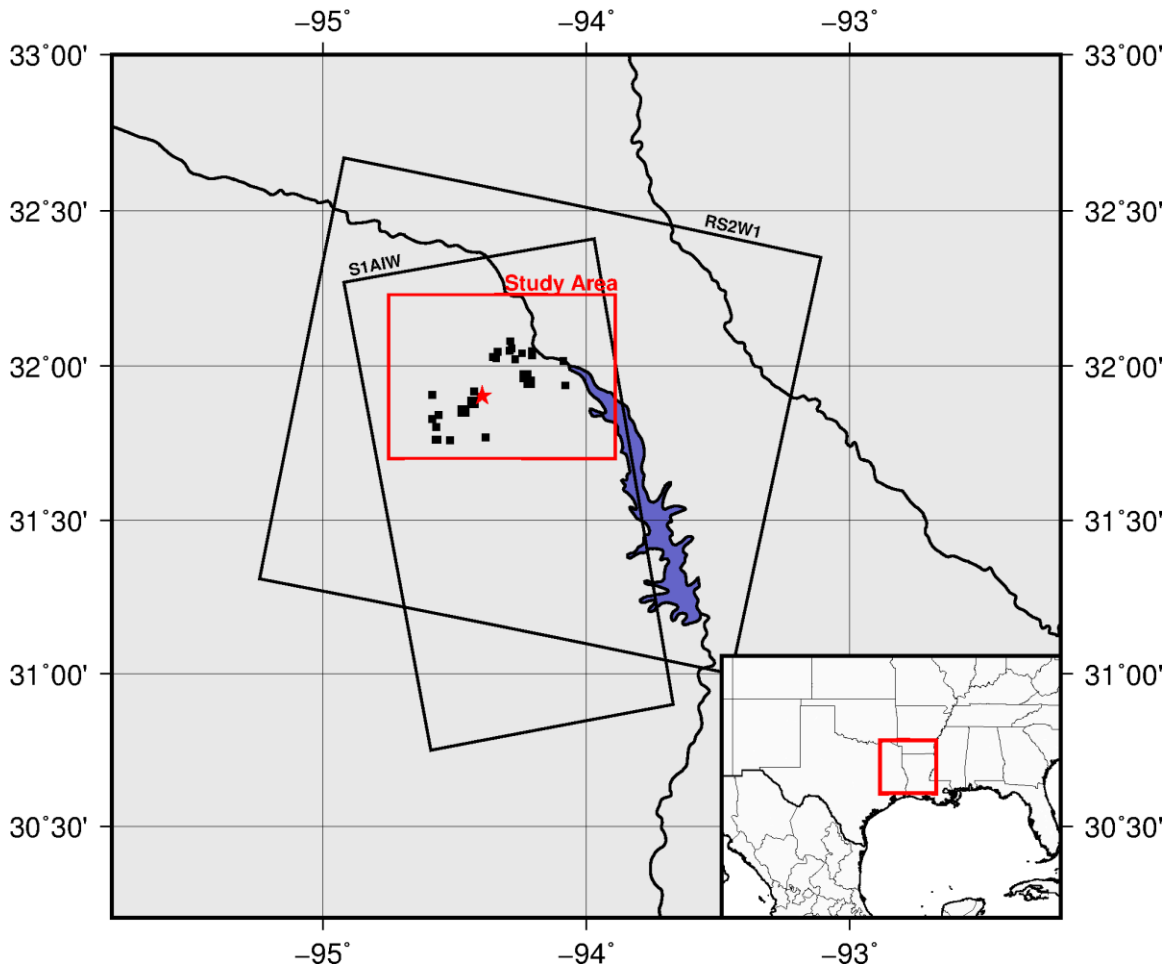
Figure 4-22 Study area investigated using MSBAS analysis for the RADARSAT-2 descending and Sentinel-1A ascending paths. The study area encompasses all the major and minor injection wells (black squares) and 2012 M4.8 earthquake (red star) at Timpson, TX.

Similar to SBAS processing discussed previously, prior to running the MSBAS software, I performed a quality check whereby only high quality Sentinel-1 and RADARSAT-2

differential interferograms were selected. For RADARSAT-2, the same interferograms were used as the SBAS processing. For Sentinel-1A, I performed a similar quality check. The coherence was measured over   a region of 40 pixels, and if it was higher than 0.6 then the interferogram was used for processing, if it was lower it was discarded. MSBAS also masks pixels through processing which do not remain coherent throughout all of the interferograms that are input into the algorithm. Sentinel-1A interferograms were also individually analyzed to remove significant atmospheric or orbital errors which can be seen in Chapter 4.1.3. In addition, these differential interferograms were resampled to a common grid, 20 m by 20 m spacing and interpolated to fill in missing data gaps. In total, eighty-one RADARSAT-2 and fourteen Sentinel-1A differential interferograms were processed using MSBAS software. Table 4-3 shows the header file containing the parameters used for MSBAS processing. Using a window size of 4779 by 4112 pixels, two reference regions were selected (C_FLAG) as calibration points close to the study are in a stable region. Also, zero order regularization (R_FLAG) and no topographic correction (T_FLAG) were applied.

```
FORMAT = 1
FILE_SIZE = 4779, 4112
WINDOW_SIZE = 0, 4778, 0, 4111
R_FLAG = 1, 0.15
C_FLAG = 2, 3167, 1444, 3444, 1889, 64, 64
T_FLAG = 0
I_FLAG = 2, par.txt
SET = 122454, -168.8102258, 26.1456, dsc.txt
SET = 001844, -12.7560756, 39.2765, asc.txt
```

Table 4-3 MSBAS header file. See Table 3-6 for definition of each parameter.

MSBAS cumulative displacements for vertical surface displacements are shown in Figure 4-23 and horizontal east-west displacements in Figure 4-24 between October 2016 and March 2017. RADARSAT-2 background intensity image is exposed in low coherence regions such as rivers and lakes.
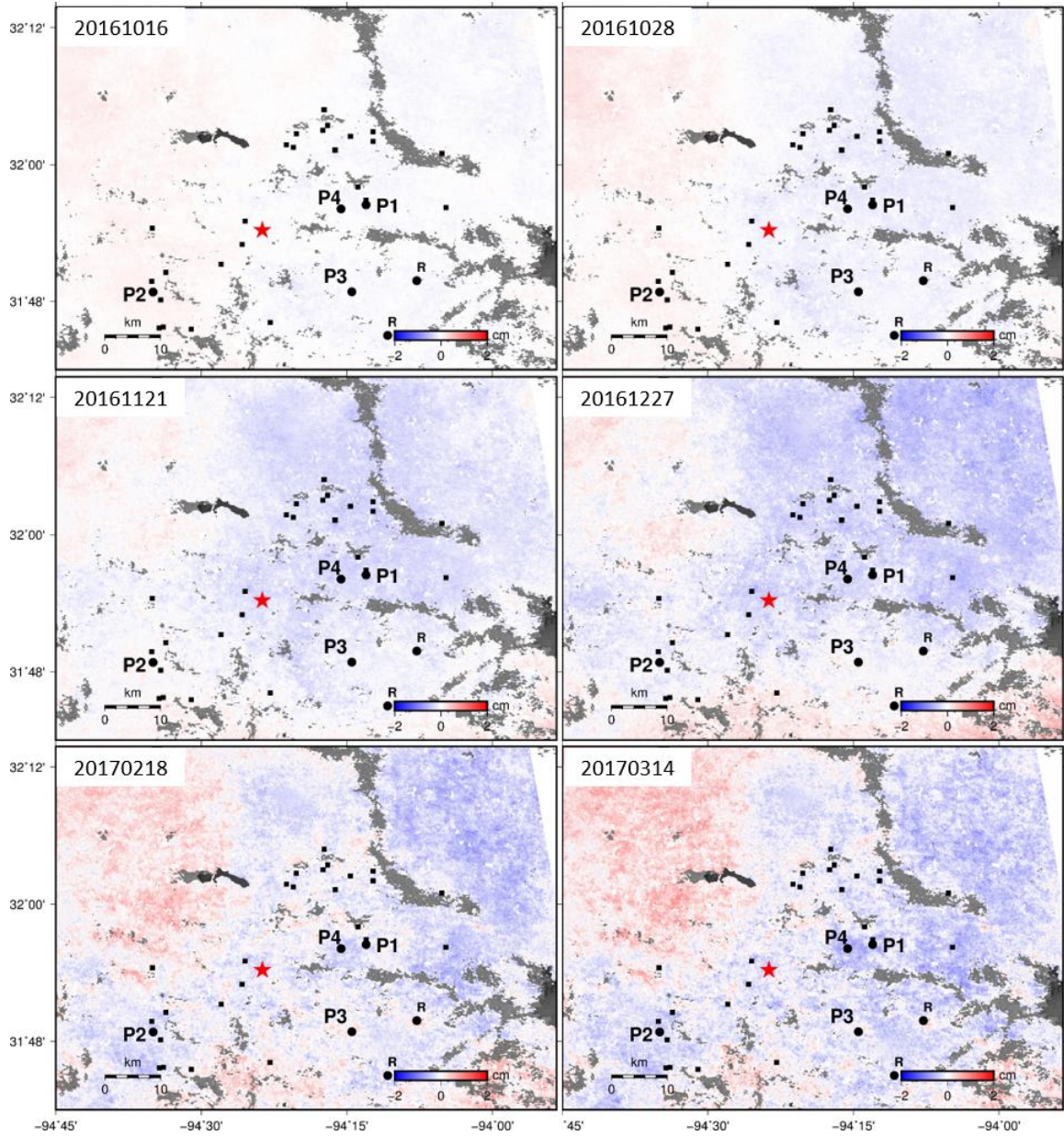
Figure 4-23 MSBAS cumulative vertical surface displacements at Timpson, TX. Injection wells (black squares) and 2012 M4.8 EQ (red star) are labelled for reference. Also shown are four time series points, *P1*, *P2*, *P3* and *P4* (black circles) and reference points labelled *R*. Displacements in cm.
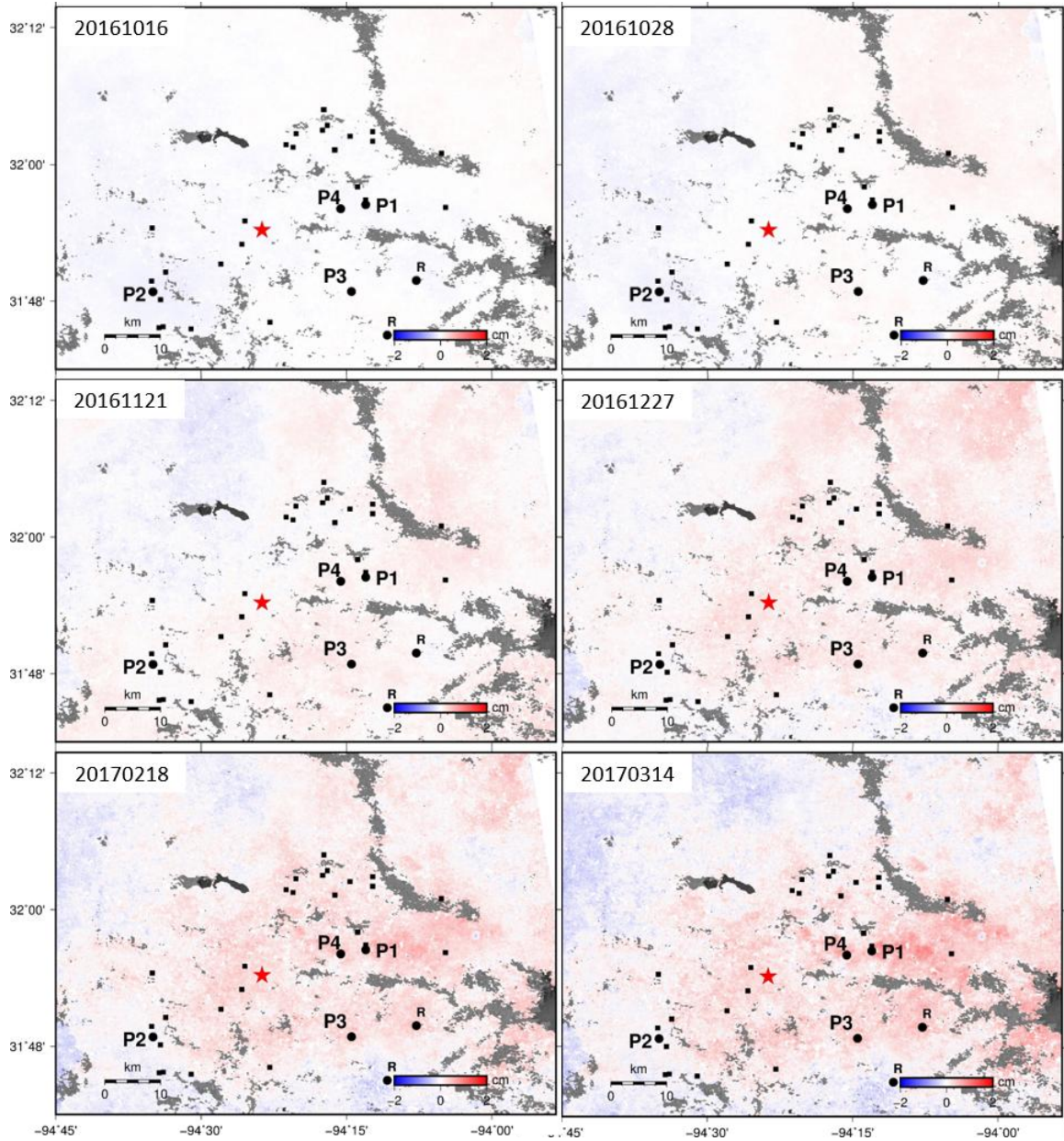
Figure 4-24 MSBAS cumulative east-west surface displacements at Timpson, TX. Injection wells (black squares) and 2012 M4.8 EQ (red star) are labelled for reference. Also shown are four time series points, *P1*, *P2*, *P3* and *P4* (black circles) and reference points labelled *R*. Displacements in cm

These cumulative deformation plots show that there is a general trend of subsidence (negative values in Figure 4-23) across the study area. Broad subsidence is evident to the east of the study area, including the eastern wells E1 and E2 and main western well W1 and W2. A region with up to 1 mm cumulative subsidence can be seen surrounding wells E1 and E2, located next to time series point P1 and P4. For comparison these time series points are the same points that were selected for SBAS processing in Chapter 4.2.

By March 2017, the east-west cumulative displacements indicates that motion in the center of the study area is focussed towards the east (red colours) whereas westward motion is located to the west side of the study area. The magnitude of the east-west horizontal motion is lower than vertical deformation, as shown in the time series in Figure 4-28. Also output from MSBAS are linear vertical and east-west displacement rate maps shown in Figure 4-25 and Figure 4-26.
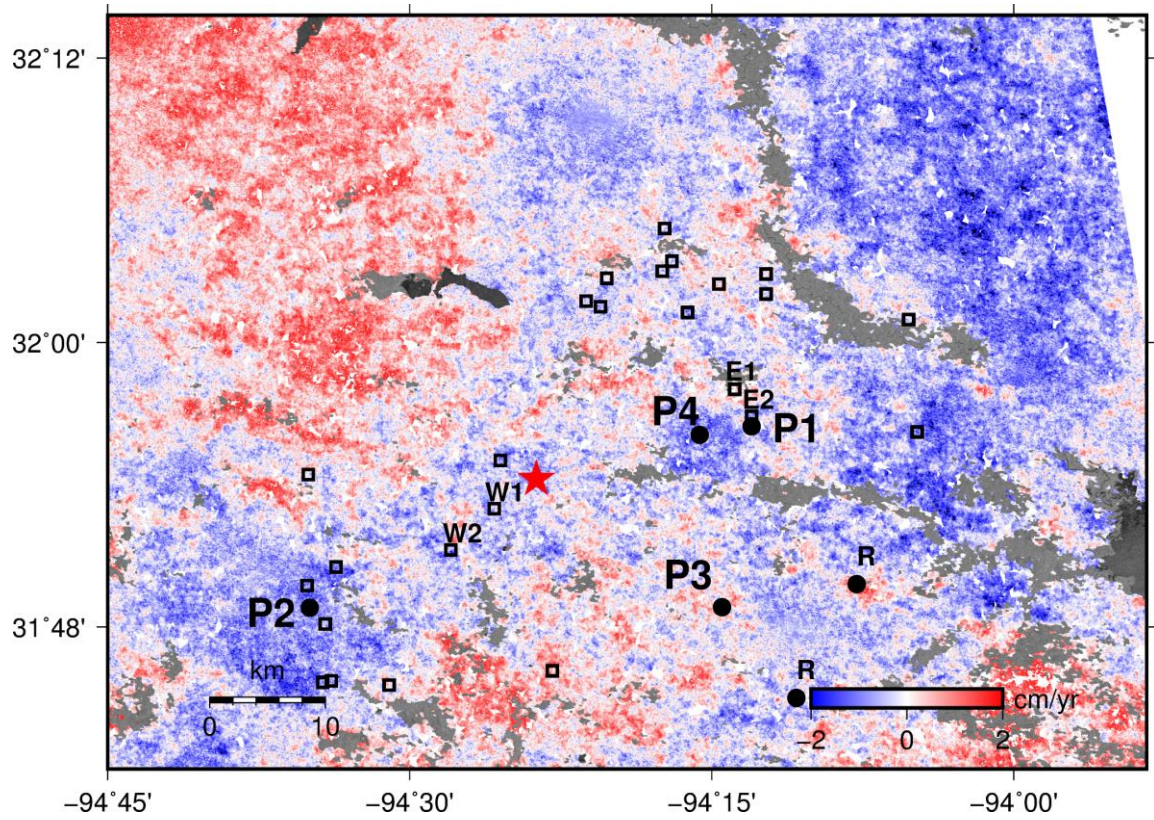
Figure 4-25 Linear vertical surface displacement rates calculated by fitting a linear trend to the MSBAS time series. Injection wells (squares) and 2012 M4.8 EQ (red star) are labelled for reference. Also shown are four time series points, *P1*, *P2*, *P3* and *P4*. Displacement rates in cm/yr.
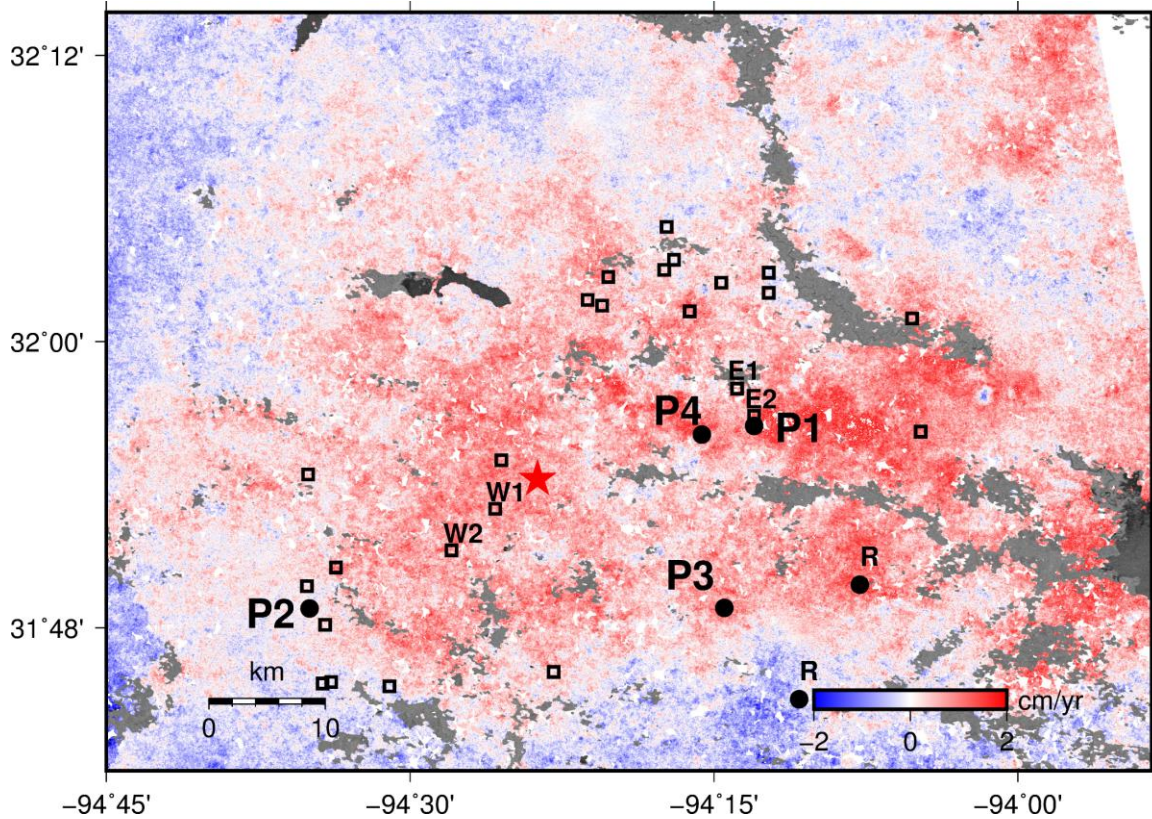
Figure 4-26 Linear east-west surface displacement rates calculated by fitting a linear trend to the MSBAS time series. Injection wells (squares) and 2012 M4.8 EQ (red star) are labelled for reference. Also shown are four time series points, *P1*, *P2*, *P3* and *P4*. Displacement rates in cm/yr.

The error associated with the displacement rates for each component are shown in Figure 4-27. The error in the vertical and horizontal components is on average 0.3 cm/year. The error is also lower in the center of the study area compared to the outer edges of the study area.

The four time series points shown in Figure 4-28 show the comparison between horizontal east-west and vertical deformation between October 2016 and March 2017. These time series indicate subsidence over this time period up to 0.4 mm.
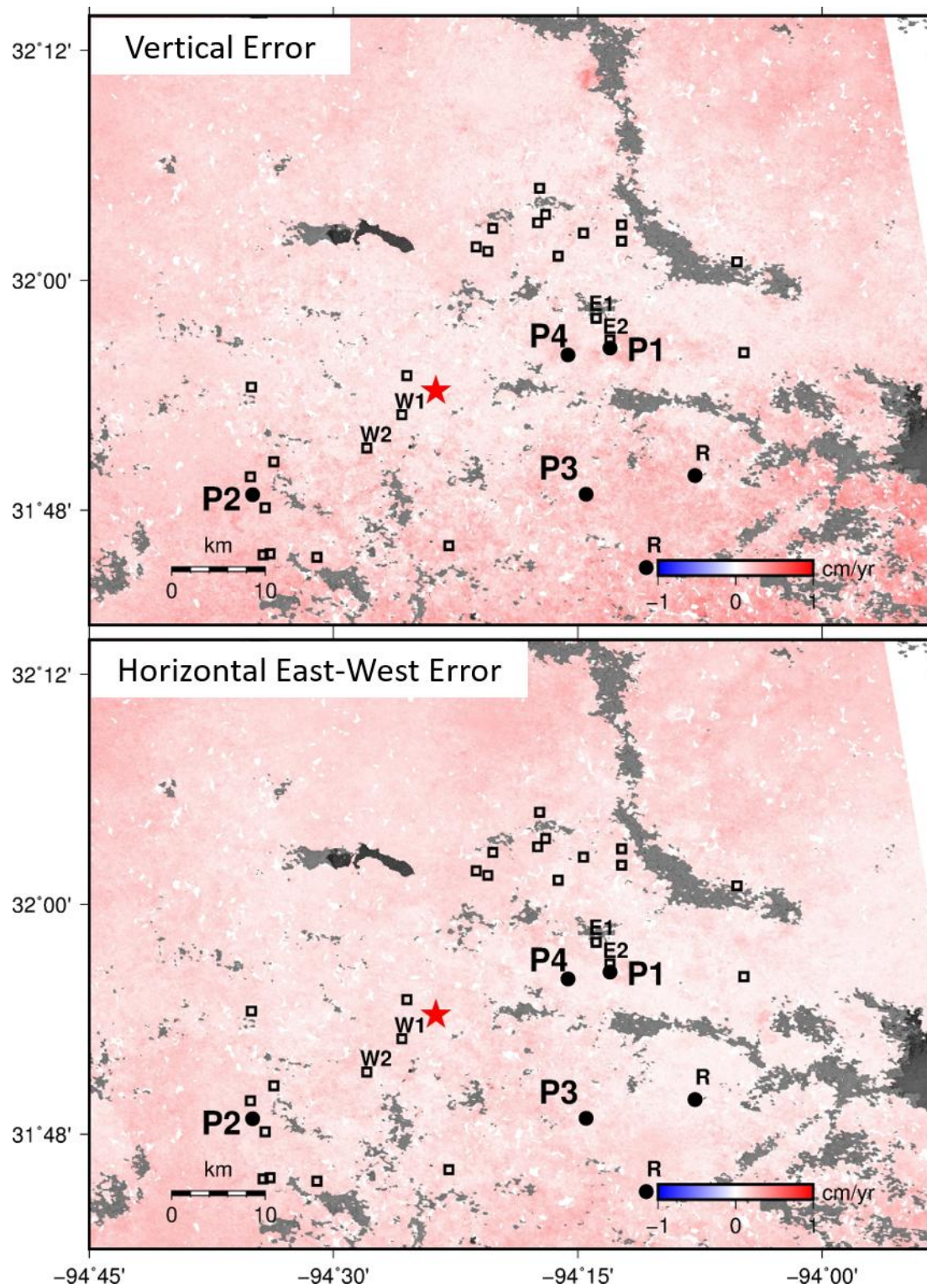
Figure 4-27 Linear vertical and horizontal east-west displacement rates error. Scale between -1 and 1 cm/yr.
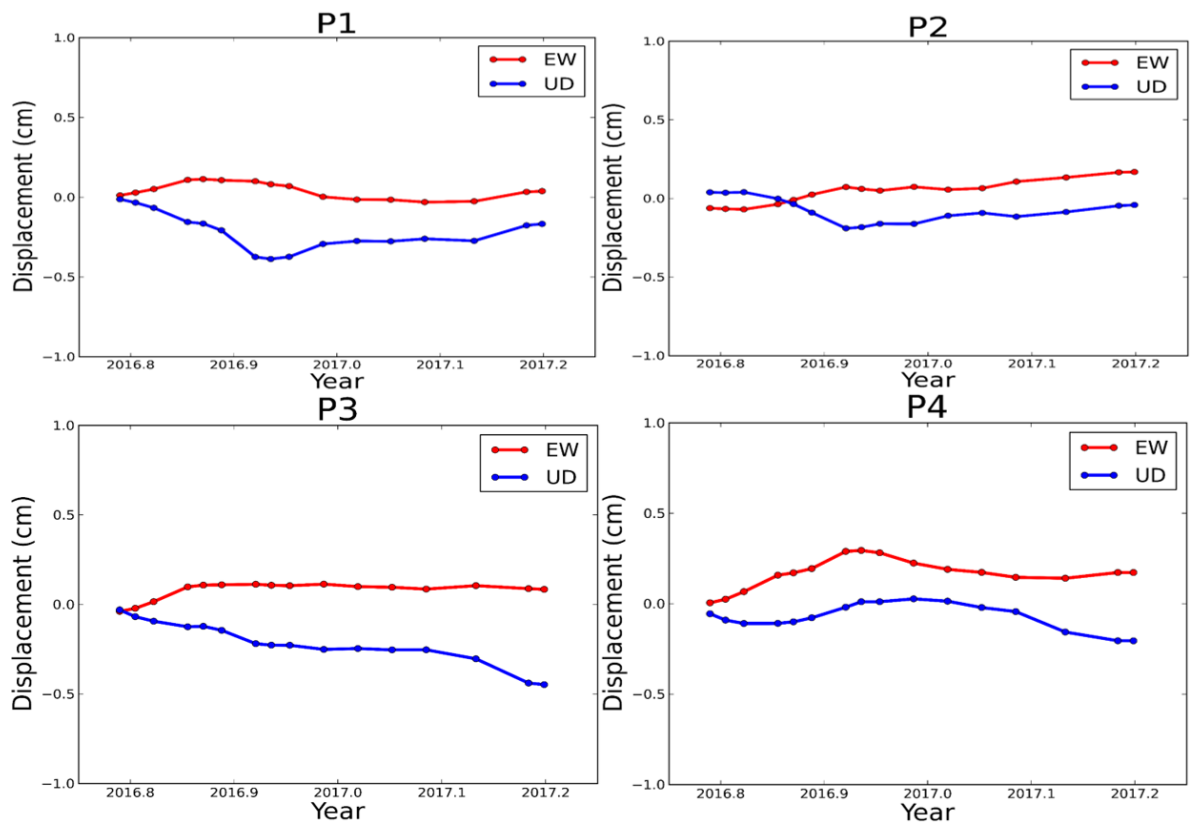
Figure 4-28 Time series of vertical (blue line) and east-west (red line) displacements for selected pixels *P1*, *P2*, *P3* and *P4*.

Chapter 5

5   General Discussion and Conclusions

This chapter discusses the differential interferograms, SBAS, and MSBAS time series analysis results presented in Chapter 4. Also, a simple elastic deformation theoretical model is proposed to match the deformation measured in the time series analysis. Finally, the limitations of the techniques used in this investigation is described, along with suggestions for future work and conclusions.

5.1   Discussions

5.1.1   SBAS Time Series

To provide an initial estimate on surface deformation at Timpson, SBAS was applied on two datasets, ALOS PALSAR and RADARSAT-2. These datasets cover two different periods of deformation, ALOS between 2007 and 2011, whereas RADARSAT-2 covers 2014 – 2017.

Between these two SBAS results, spanning 2007 to 2011 and 2014 to 2017, we can identify a spatial relationship between seismicity and wastewater disposal activity at Timpson in both time periods. Due to the large volumes of fluid injected into the subsurface at these disposal wells, uplift is detected during both of these time periods. Also, linear displacement rates suggest that uplift over this period has remained around 1 cm/year.

Firstly, RADARSAT-2 SBAS results can be compared to a previous study, which investigates fluid injection at Timpson. Shirzaei et al. (2016) primarily used interferograms acquired by the ALOS satellite to measure surface uplift over the same well injection sites studied in this thesis. However, to validate their results, RADARSAT-2 images were also acquired between 6 March and 21 August 2014. An example of a RADARSAT-2 differential interferogram calculated by Shirzaei et al. (2016) spanning around 1 month alongside estimated LOS cumulative displacement is shown in Figure

5-1. This figure shows a broad region of uplift that spans the entire study region, with LOS deformation rates around ~5mm over a ~6-month interval.

Compared to time series results found in this study, the areal extent of uplift in Figure 5-1 is similar to that shown in Figure 4-13 for the corresponding time-period. Differences in this area could be due to processing. For example, different methods of unwrapping or different time scales of measured deformation between the two studies can result in variability in the results. However, both areas of uplift cover the entire study area, including the main wells, E1, E2, W1 and W2. In addition, a similar magnitude of deformation was found in this investigation (Figure 4-14), 10 – 15 mm per year, which agrees with ~5 mm over a 6-month interval found by Shirzaei et al. (2016). However, in this investigation, there are more images collected over a greater period of time, producing a denser time series.
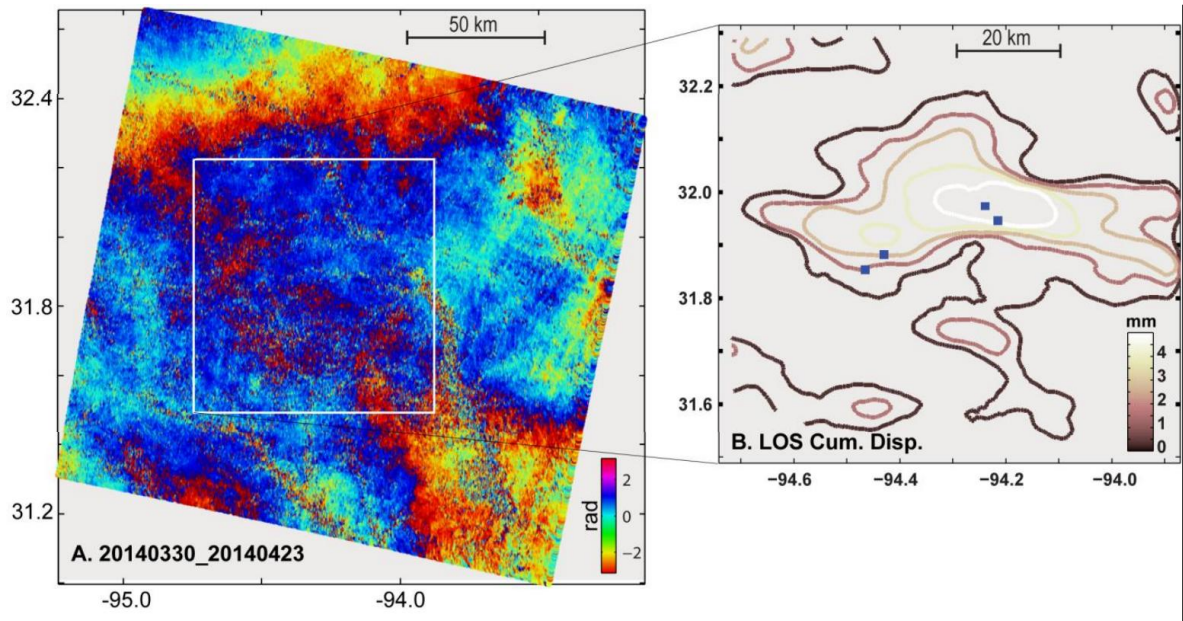
Figure 5-1 Left) RADARSAT-2 differential interferogram between 30 March and 21 April 2014 and right) estimated LOS cumulative displacement over a period of 6 months. Blue squares represent the four major injection wells, from Shirzaei et al. (2016).

ALOS SBAS results also can be compared to the past study by Shirzaei et al. (2016). Cumulative LOS deformation from July 2007 to December 2010 is presented in Figure

5-2, as computed by Shirzaei et al. (2016). These images span the same time-period as the deformation maps generated in this study, shown in Figure 4-18. Figure 5-2 shows cumulative surface uplift up to 10 mm and is concentrated over the eastern wells between 2007 and 2010. Large uplift between ~6-8 mm begins in May 2008 and cumulatively increases to ~10 mm deformation by May 2010.
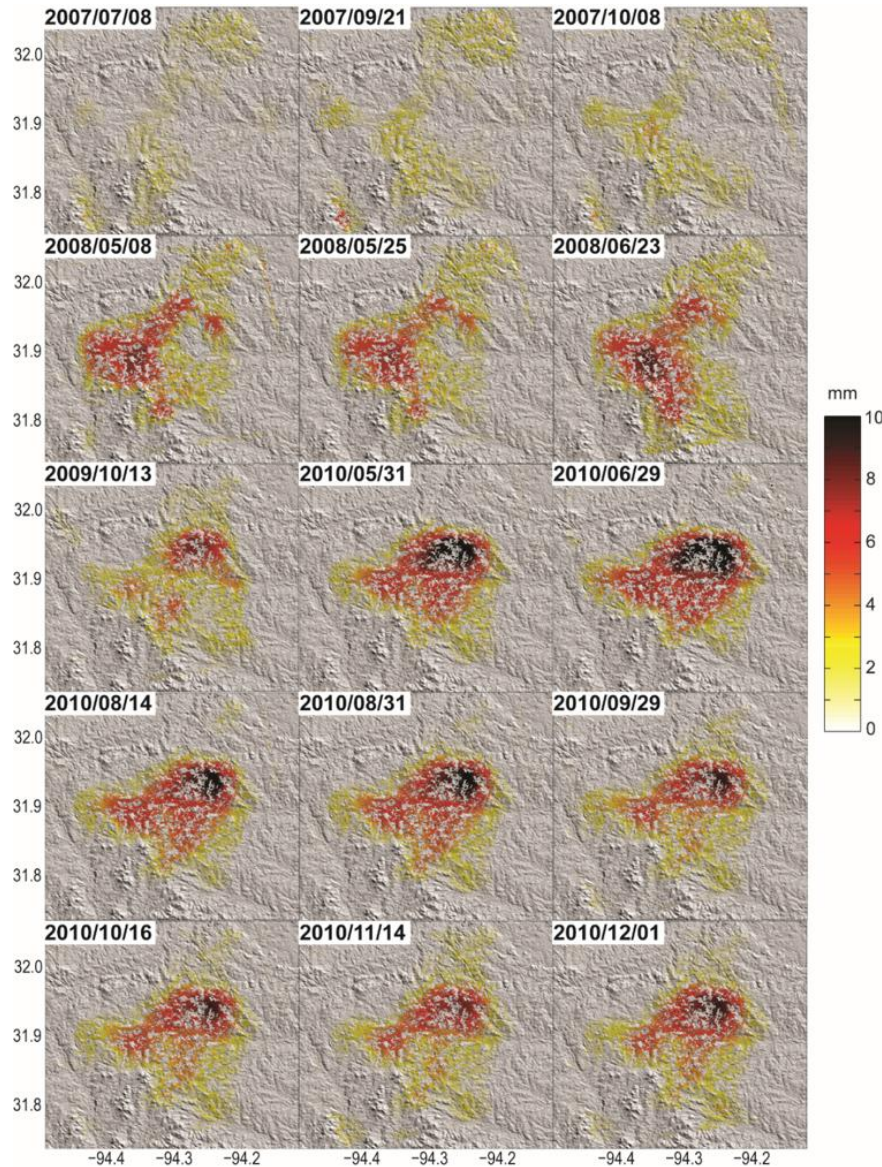
Figure 5-2 Cumulative surface deformation for 15 individual time steps, with respect to initial acquisition in July 2007. Motion is in satellites LOS, positive values indicate motion toward the satellite, courtesy of M. Shirzaei.

Comparing these results to those found in this study (Figure 4-18), there is a similar pattern of uplift concentrated over the eastern wells and extending to the west. However, the scale of deformation varies between studies. In this study, a cumulative uplift of ~2 cm was measured (Figure 4-18), whereas Shirzaei et al. (2016) measured 1 cm cumulative uplift (Figure 5-2). Differences in this magnitude may be due to the different datasets used by the studies. Shirzaei et al. (2016) combined three sets of overlapping ALOS tracks, whereas only one ALOS track was used in this study. Therefore, Shirzaei et al. (2016) had three times greater temporal sampling compared to this study. An increase in temporal sampling produces a denser time series of deformation, avoiding large time gaps where there is little or no data. As shown in Figure 4-21, due to the sparsity of data between 2008 and 2010, there are only three time series points measuring up to 1 cm uplift. If there was more data, thus a denser time series, this jump in deformation may be reduced and begin to match displacements similar to Shirzaei et al. (2016).

Differences in the order of magnitude between the studies may also be due to the presence of orbital errors or atmospheric artefacts remaining in the differential interferograms. To effectively remove these artefacts, additional processing is required. For example, as discussed in Chapter 1.4.4, atmospheric data is required to model for these phase delays (Bekaert et al., 2015) to remove atmospheric artefacts, and is beyond the scope of this study.

In addition, the main region of uplift present in the SBAS LOS results shown in this study, there are other regions of uplift and subsidence surrounding this region. An example of these can be seen in the northern and southern half of Figure 4-14, where subsidence (blue) can be seen bordering the main region of uplift. These negative motions are a function of the reference system that is used in the SBAS processing. Therefore, these negative motions are just motions relative to the zero reference point used in processing and not interpreted as ground deformation.

Another source of error in the SBAS results shown in Chapters 4.2 and 4.3 may arise from unwrapping errors surround incoherent features, such as lakes, that are propagated

through to SBAS analysis. An example of these errors are shown in Figure 4-18 and Figure 4-19, surrounding the lake to the north in the study area. These high amplitude, small regions of uplift and subsidence remained coherent, so they were not masked during processing but do not accurately represent ground motion. This is confirmed in Figure 4-20, where the largest error in ALOS SBAS results is in these regions on the edge of the decorrelated river system.

Uplift detected towards the eastern wells comes as no surprise as large volumes of wastewater were injected at a shallow depth around ~860 m deep (Table 2-2) at the two major injection wells E1 and E2.

5.1.2   MSBAS RADARSAT-2 and Sentinel-1A

Previously in this chapter, I discussed one-dimensional surface displacements using SBAS time series analysis. In order to provide a more detailed description of ground motion, MSBAS decomposes the LOS displacements into two components, east-west and vertical motions. RADARSAT-2 and Sentinel-1A provided the greatest spatial coverage over the study region with a large volume of differential interferograms available for processing. A combined total of 95 images were available, spanning five months from October 2016 to March 2017. Sentinel-1A limits the time range for which MSBAS can be applied since it only started acquiring images over Timpson from October 2016 onwards, despite being operational since April 2014.

MSBAS results shown in Figure 4-23 and Figure 4-28 present the ground displacements over the study region, separated into east-west and vertical motions. For the vertical time series results (Figure 4-28), a large region of subsidence is present over the study area. In this study, we investigate wastewater injection, and subsidence of the surface is not normally expected. However, the injection rate for the four main wells shown in Figure 2-3 show that injection has stopped in both western wells (W1 since 2016 and W2 since 2014) and injection has significantly decreased at E1 since 2014 (injection volume rate for well E2 is not currently available). As a result, there has been an overall decrease in the volume of fluid injected into the subsurface, relative to that in the past. It was found from SBAS results that the surface had been uplifting since 2007 due to large rates of

fluid injected into the subsurface. Since then, the rate of fluid injection has significantly decreased, which we can interpret as a decrease in pore pressure within the underlying reservoir. The surface responds to this relative pressure decrease by subsiding, evident in our vertical MSBAS results.

We also can compare the MSBAS vertical time series (Figure 4-28) to RADARSAT-2 SBAS time series (Figure 4-16) over the same period, October 2016 to March 2017. RADARSAT-2 time series results indicate a similar pattern of subsidence. In fact, RADARSAT-2 time series shown in Figure 4-16 suggest subsidence has been ongoing since around June 2016.

Horizontal east-west surface displacements indicate eastward motion towards the eastern side of the study area, whereas western motion is located to the west side of the study area. For a region of subsidence in the center of the study area, east-west displacement maps should be symmetric, but opposite, in the surrounding region. For example, one side of the area of subsidence should move eastward, and the other side move westward. Also, although the magnitudes of east-west motion are less than vertical, it remains higher than anticipated. For example, a simple elastic model applied for an area of subsidence by Samsonov et al. (2016), shows the magnitude of the east-west component is approximately half the magnitude of vertical. MSBAS results shown in this study show a similar relationship between the two components. This can be explained by the other horizontal component that is not modelled with MSBAS, the north-south component. MSBAS neglects this component since DInSAR is insensitive to motion along track, but still may exist within the differential interferograms. We suggest that aliasing of the north-south motion into the east-west component of motion explains the large horizontal magnitudes modelled by MSBAS in this study.

MSBAS analysis heavily relies upon using a highly coherent stack of interferograms. Any errors within the input interferograms, such as orbital or atmospheric are carried into the velocity inversions and propagate to future time steps through integration. Some Sentinel-1A differential interferograms presented in Figure 4-8 and Figure 4-9 remain highly coherent, but contain significant residual orbital or atmospheric errors. Therefore,

these sources of noise contribute to the variations in horizontal signal as previously discussed.

Overall, our MSBAS results suggest a broad region of subsidence, centered on the eastern wells, E1 and E2, where uplift was previously measured from SBAS results. Although east-west surface displacements do not suggest subsidence, this may be explained by north-south aliasing or propagation of orbital errors. Further work is needed in order to confirm the results found by MSBAS in this study.

5.2   Elastic Deformation Model

To model the surface displacements found in this investigation, I applied a simple analytical model that describes the surface deformation in an elastic medium due to the pressure change within an underlying reservoir (Geertsma, 1973; Le Mouélic et al., 2002).

This model assumes the reservoir is a flattened disk with radius R, thickness h, buried at a depth D and height variation due to pressure change given by Δh. In this model, the subsurface is treated as an elastic half space with a Poisson's ratio v. The vertical (u_z) and horizontal (u_r) surface displacements at a radial distance r (origin located on the surface) are given by

$$u_z(r) = (2v - 2)\Delta h R \int_0^\infty e^{-D\alpha} J_1(\alpha R) J_0(\alpha r) d\alpha \qquad \text{(Equation 5-1)}$$

$$u_r(r) = (2v - 2)\Delta h R \int_0^\infty e^{-D\alpha} J_1(\alpha R) J_1(\alpha r) d\alpha \qquad \text{(Equation 5-2)}$$

where J_0 and J_1 are Bessel functions of zero and first order respectively. Δh is also related to the change in pressure ΔP, Young's modulus E and h by $\Delta h = h\Delta P/E$.

This simple model has been successfully applied in past studies, modelling regions of both uplift and subsidence. For example Samsonov et al. (2016) measured rapid

subsidence in the downtown of Seattle, WA, and Le Mouélic et al. (2002) modelled surface uplift in Paris, France, due to fluid injection. In this study, a simple elastic model is presented for uplift measured using ALOS SBAS time series results.

ALOS SBAS time series results (Chapter 4.3) were used to model cumulative uplift between December 2007 and December 2010. Figure 5-3 shows the cross section *A-B* for which uplift is modelled, which is orientated north-south across a region of rapid uplift next to the eastern wells.
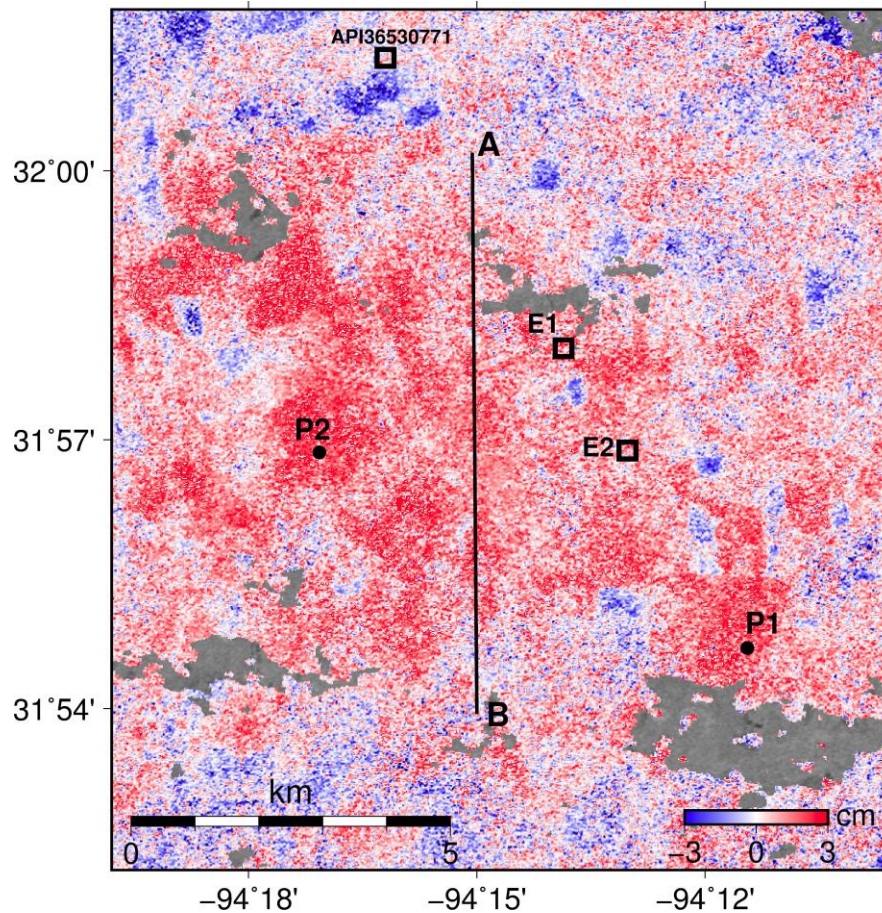
Figure 5-3 Map of cumulative ALOS LOS displacements between 2007 and 2010, highlighting the cross section *A-B* used for the elastic model. Also labelled are the location of time series point *P1* and *P2*, major injection wells *E1* and *E2* and the closest other well *API36530771*.

Since ALOS SBAS results only produced one dimensional time series in the satellites LOS, the first step was to calculate the vertical component of deformation. I converted LOS displacements to vertical using the relationship (Hanssen, 2001),

$$d_{vert} = \frac{d_{LOS}}{\cos(\theta)}$$

(Equation 5-3)

where d_{vert} is the vertical component of displacement, d_{LOS} is LOS displacement and θ is the satellite incidence angle. In this case, the incidence angle for ALOS of 38.7 degrees was used to convert LOS to vertical displacements.

Model Parameter	Parameter Value
Poisson's Ratio, ν	0.4
Head change, Δh (m)	0.02 – 0.05
Radius of pumping zone, R (m)	3600
Depth of aquifer, D (m)	875
Thickness of aquifer, h (m)	100

Table 5-1 Table of parameters used for the elastic deformation model for the period of uplift between 2007 and 2010.

Input parameters were inferred through modelling and prior studies over this region and are shown in Table 5-1. In this model, I describe a reservoir formed through wastewater injection into the Washita Group Limestone at a depth of 875 m. This depth is known from injection data shown in Table 2-2 and is assumed to be the center of the reservoir. Unfortunately, no well logs are available for wells in the eastern half of the study area to further constrain this depth. It also is assumed that the reservoir is contained entirely within the Washita Limestone, with a thickness of 100 m (Granata, 1963). This reservoir is unconfined, however below the Washita Limestone is a confining unit, the Ferry Lake

Anhydrite which acts as a barrier to the downwards motion of fluid. The radius of the reservoir was constrained by the areal extent of total spatial displacement that can be seen in MSBAS. For example, a diameter of around ~8 km total uplift is identified along the cross section, therefore a radius of 3600 m was used. Also, an undrained Poisson's ratio $v=0.4$ was used assuming a fully saturated reservoir (Shirzaei et al., 2016). Once these parameters were constrained, the change in head, Δh was varied in order to find the closest match to maximum height change for the cross section.
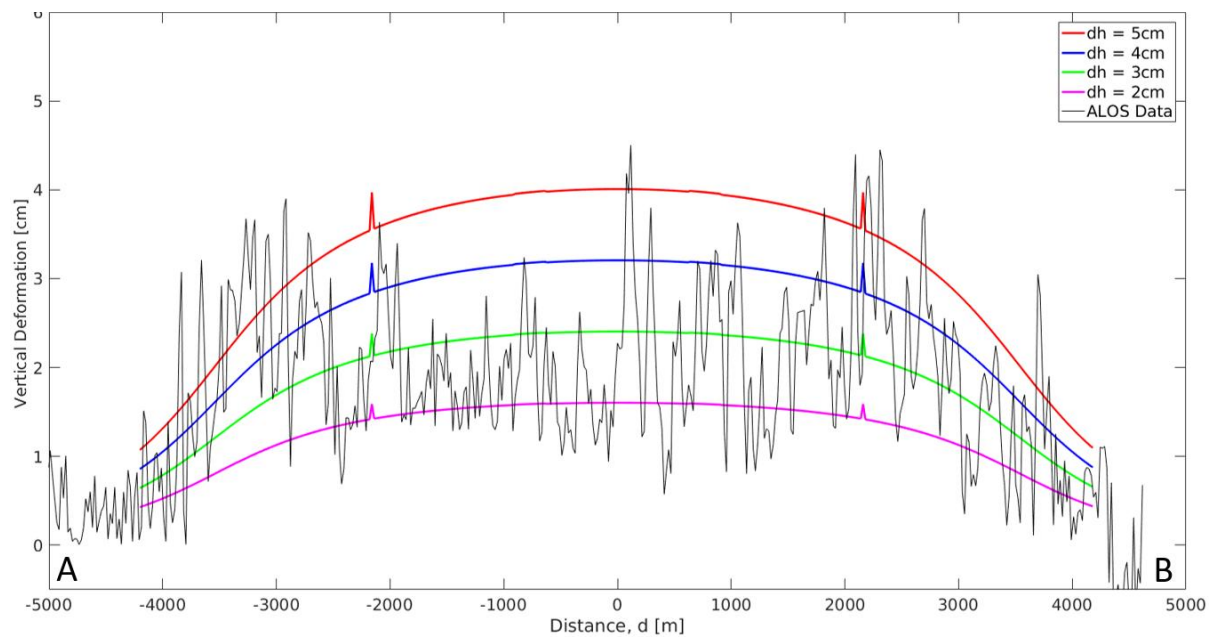
Figure 5-4 Cross section for the cumulative vertical displacement between December 2007 and 2010. Profile extends from point *A* (94.25W, 32.005N) to point *B* (94.25W, 31.899N).

The code for this elastic model, acquired from Le Mouélic et al. (2002), was generated in IDL programming language however the output results in Figure 5-4 were plotted in MATLAB.

The cross section of cumulative vertical displacements is shown in Figure 5-4, for four separate cases, an increase in hydraulic head of 2, 3, 4 and 5 cm. This shows that by constraining the radius of the reservoir at a known depth, the model fits well with the

lateral change in deformation, particularly towards the edges of the model. The model also fits the maximum cumulative uplift around 4 cm over the period 2007 to 2010. Due to the noise contained in the data, the amplitude of deformation is hard to constrain with a single value of *dh*. However, the best fitting value for head change, *dh*, lies within the range 2 to 5 cm.

In Figure 5-4 it is clear that there is some spatial variation along the region of maximum uplift between -3000 and 3000 m. Along this segment of the cross section, there are sections with lower surface displacements than others, causing deviations from the predicted model. These deviations may be due to the assumptions made in the model. For example, we assume a homogeneous half space throughout. However, in reality, this is not the case and inhomogeneous regions within the reservoir and surrounding half space exist, causing deviations from the models predicted displacements and the data. There are also artefacts present within the model located at -2000 and 2000 m.

Using the parameters found by fitting the best fit model to vertical surface displacements, the cumulative pressure change in the underlying reservoir can be calculated. This change in pressure is related to the change in head, Δh by,

$$\Delta P = \frac{E \, \Delta h}{h}$$
(Equation 5-4)

where E is Young's modulus of the reservoir and h is reservoir thickness. In order to perform this calculation, first the Young's modulus must be calculated. Young's modulus can be expressed in terms of Poisson's ratio and shear modulus, G,

$$E = 2G(1 + v)$$
(Equation 5-5)

A previous study by Shirzaei et al., (2016) found a shear modulus of 10 GPa for a limestone unit buried at a depth of ~1000m. Therefore, I calculate the Young's modulus, using Poisson's ratio equal to 0.4, E = 2.8 GPa. Using a change in head, Δh= 3±1 cm from Figure 5-4, I estimate the pressure change, ΔP = 1.05±0.35 MPa.

This result can be compared to that of a previous study over this region by Shirzaei et al., (2016). They identified a zone of maximum pore pressure increase under the eastern wells at a depth of 850 m within the Washita Limestone. They found a pore pressure increase of 0.5 to 1.5 MPa, which agrees with the result found in this study despite the differences in approach to modelling.

Although we see a significant increase in pore pressure, we do not witness seismicity at the eastern wells (Figure 2-2). Whilst large volumes of fluid are injected into the subsurface at the eastern wells, it is done in a shallow layer (875 m), within a stable frictional regime (Scholz, 2002) whereby changes in pore pressure are less likely to induce seismic rupture (Shirzaei et al., 2016). There are no faults present at this shallow depth, however faults may lay deeper in the underlying basement. The lack of seismicity at the eastern wells also suggests that the downward migration of fluid is restricted by the underlying impermeable Ferry Lake Anhydrite.

At the western wells however, wastewater is injected at greater depths of 1800 m, below the Ferry Lake Anhydrite, whereby small changes in pore pressure within the reservoir can initiate slip. The likelihood of slip at such depths are also increased in the presence of basement faults, which are known to be in the vicinity of the western wells.

5.3   Limitations

The main limitation in this study is the availability of InSAR data to provide both spatial and temporal coverage. First, ascending and descending data that overlaps in time and space is required in order to perform MSBAS processing. Although this study had one ascending and one descending dataset, which cover the entire study area, the temporal coverage only allowed for late 2016 to 2017 deformation to be measured using MSBAS. This is due to the Sentinel-1A satellite, which only had images available over the study area after late 2016. Second, there were no ALOS PALSAR frames which covered the entire study region, so only a single ALOS frame was chosen for SBAS processing. Third, although ALOS-2 frames covered the entire study area from 2014 to 2016, only three differential interferograms were available, which is insufficient for SBAS time series analysis.

For time series analysis, the main limitation with SBAS and MSBAS processing is that it relies on SAR data with small spatial and temporal baselines. Any large variations in these baselines cause significant decorrelation and the resulting differential interferogram is no longer useful for SBAS processing. Also, the solution to MSBAS is an approximation, since it neglects the north-south component of motion. This limits the amount of interpretation when modelling for horizontal motion for example with the elastic deformation modelling, which will then overestimate for horizontal motions.

A single DInSAR dataset is also limited by only measuring surface displacements in the satellites LOS. Therefore, when applying SBAS analysis, assumptions must be made when decomposing the LOS displacements into vertical and horizontal motions.

5.4   Future Work

There are several outstanding points for future studies related to this thesis that I would like to discuss in this section. First, the availability of SAR images limits the spatial and temporal coverage when performing MSBAS time series analysis. Over time, more SAR images will become available over Timpson, which can then be incorporated into the currently automated MSBAS processing scripts that I created for this study. For example, with the launch of the new Sentinel-1B satellite, the Sentinel constellation can acquire images every 6 days (ESA, 2017a). This will not only increase the length but also the density of the time series to provide near real-time deformation information at Timpson.

Future studies may consider further analysis of atmospheric errors within the differential interferograms. In the DInSAR community, advanced methods have been proposed to mitigate atmospheric noise. Bekaert et al. (2015) for example, compared the most effective InSAR tropospheric correction techniques, any of which could be applied in this study to improve surface deformation interpretations.

A follow-on study from this investigation could further analyze the surface displacements by modelling surface deformation using more advanced methods. For example, instead of using a simple one-dimensional deformation model, a two-dimensional model could be

applied by extrapolating the model used in this study over the study area. This would provide a better picture on the spatial magnitude and scale of deformation. Also, since the uplift pattern has an asymmetric pattern, a more complex shape of subsurface reservoir, taking into account a more detailed description of geological structures would be required to reproduce a more accurate shape of deformation.

GPS data also is commonly combined with DInSAR analysis to add to surface deformation measurements already provided by DInSAR. DInSAR only measures relative phase changes however, GPS provides a reference for which the DInSAR measurements can be resampled to. Although expensive, the installation of GPS stations at Timpson, will provide additional surface displacement measurements which the DInSAR results can be compared to.

Highly coherent differential interferograms are required in order to accurately perform MSBAS time series analysis. Higher resolution digital surface models (DSMs) provide higher accuracy topographic signal removal, therefore improving the quality of the differential interferograms. Optical satellites, such as Digital Globe's Worldview satellites, can be used to produce high-resolution (2 m) DSMs, which can then be used to remove the topographic signal. This would greatly improve the resolution of DInSAR dataset and provide a better estimate of the surface deformation occurring at Timpson.

This study uses advanced DInSAR analysis to relate induced seismicity to wastewater disposal activities, however, this approach could also be applied in regions where other unconventional oil and gas extraction techniques such as hydraulic fracturing activities are located. Western Canada in particular has seen a significant increase in seismicity related to hydraulic fracturing (Atkinson et al., 2016). An interesting further application of this work could be the comparison between hydraulic fracturing and wastewater disposal to ground deformation.

One final thought for future investigations at Timpson could be analysis of the errors associated with time series analysis. Typically, error analysis can be applied to GPS time series to decompose the sources of error into its different components. For example, Hector software can remove linear trends in time series caused by temporally correlated

noise (Bos et al., 2013). An interesting addition to this study would be an investigation into the errors associated with the MSBAS time series results found in this study.

5.5   Conclusions

In this thesis, I have successfully applied advanced DInSAR analysis to spatiotemporally relate induced seismicity and wastewater disposal activities at Timpson. I achieved this by applying differential interferometry and time series analysis using four space-borne satellites, RADARSAT-2, ALOS PALSAR, ALOS-2 and Sentinel-1A. For each of these satellites, I applied DInSAR analysis to generate a coherent stack of interferograms. Time series analysis was then performed using two techniques, SBAS and MSBAS, to reveal the spatial and temporal relationship between seismicity and wastewater injection activities.

In Chapter 1, I began by introducing induced seismicity in North America, including western Canada and central and eastern US. Next, I provided a background on the technique that I used in this investigation, DInSAR analysis, which includes SAR, InSAR and differential interferometry. Following this, I introduced the time series analysis technique used in this study including a derivation of the MSBAS method and its advantages and limitations.

In Chapter 2, I focused on the region of interest for this thesis, Timpson. Here, I analyzed the recent induced seismicity including the $M_w4.8$ earthquake that occurred on 17 May 2012. I then presented wastewater disposal activity in the form of maps of well locations and tables of depths and volumes of injection, for two pairs of major injection wells W1, W2, E1 and E2 and other wells within a 15 km radius. The remainder of Chapter 2 discussed the geology of the region, including the geological setting and well log analysis.

In Chapter 3 I described the satellite data and methods used in this study. Firstly, I introduced each satellite and presented a summary of the data provided by each. Second, I describe the step by step method of DInSAR data processing, which differs for each

satellite. Finally, MSBAS and SBAS methodology is discussed, including the format of input parameters and output of files.

In Chapter 4, I present the differential interferogram results for each satellite that I used in this study. Overall, these differential interferograms were highly coherent for short temporal and spatial baselines and were sufficient for MSBAS processing. Using these interferograms, I show the results of SBAS analysis using a single SAR dataset, RADARSAT-2 and ALOS, and MSBAS analysis to reveal two components of deformation. RADARSAT-2 and ALOS SBAS results revealed cumulative surface uplift between 2007-2010 and 2014-2017 respectively, however these results were limited by only measuring one component of motion in the satellites LOS. However, MSBAS results decomposed surface deformation into two components east-west and vertical motion using descending RADARSAT-2 and Sentinel-1A data. Results suggest a recent period of subsidence surrounding the injection wells which can be linked to the significant decrease in the rate of volume of injected fluid at the main wells.

Finally, in Chapter 5 I discuss the impact of these results in relating induced seismicity and wastewater injection activity and compared these to a previous study over the region. I also applied a simple elastic model which matches surface deformation from time series results. I found a 1.05±0.35 MPa pressure increase between 2007 and 2010, which agrees with results from previous studies.

5.5.1   Concluding Remarks

The main conclusion of this thesis is that advanced remote sensing techniques, such as DInSAR, are valuable tools in monitoring surface deformation in order to relate surface deformation to pressure changes within the subsurface. This work also shows that MSBAS analysis is a unique time series method that can track two-dimensional, small-scale surface deformation over long periods.

Although limited by data availability and spatial and temporal baselines, I have successfully applied SBAS time series analysis to measure surface uplift at Timpson over two separate periods, 2007-2010 and 2014 to 2016. Measurable surface deformation was

detected over 10 km from the injection wells, indicating the large extent of subsurface pressure perturbations. Also, a reservoir located at 875 m depth with a radius of ~7 km was found upon successfully fitting a simple elastic model to the data, agreeing with other studies for this region. It is evident from the results presented in Chapter 4 that MSBAS time series analysis relies heavily upon processing a highly coherent stack of differential interferograms. If differential interferograms are processed incorrectly or contain significant noise, such as atmospheric or orbital, MSBAS interpretations of surface displacements and velocities are highly affected.

In conclusion, this work demonstrates that ongoing monitoring of wastewater injection activity and associated induced seismicity using advanced DInSAR techniques provides an accurate, near-real time method in analyzing induced seismic hazard. This work forms part of a larger investigation in understanding induced seismicity processes and to mitigate the risk to critical infrastructure, through surface deformation or induced seismicity, posed by unconventional energy extraction technologies. Essentially, results from this study provide the objective scientific basis for public policy and regulation of the oil and gas industry.

Bibliography

AAPG 2016. Quick-look lithology from logs. Available from: http://wiki.aapg.org/Quick-look_lithology_from_logs [Accessed August 5, 2017].

Adams, R.L. 2009. Basement tectonics and origin of the Sabine Uplift. *Gulf Coast Association of Geological Societies Transactions*. **59**,pp.3–19.

Ai, B., Liu, K., Li, X. and Li, D.H. 2008. Flat-earth phase removal algorithm improved with frequency information of interferogram *In*: *Geoinformatics 2008 and Joint Conference on GIS and Built Environment: Classification of Remote Sensing Images*. Guangzhou, China.

Amelung, F., Galloway, D.L., Bell, J.W., Zebker, H. a. and Laczniak, R.J. 1999. Sensing the ups and downs of Las Vegas: InSAR reveals structural control of land subsidence and aquifer-system deformation. *Geology*. **27**(6),pp.483–486.

ASF 2017. Alaska Satellite Facility Vertex. Available from: https://vertex.daac.asf.alaska.edu/ [Accessed January 6, 2017].

Atkinson, G., Assatourians, K., Cheadle, B. and Greig, W. 2015. Ground Motions from Three Recent Earthquakes in Western Alberta and Northeastern British Columbia and Their Implications for Induced-Seismicity Hazard in Eastern Regions. *Seismological Research Letters*. **86**(3),pp.1022–1031.

Atkinson, G., Eaton, D., Ghofrani, H., Walker, D., Cheadle, B., Schultz, R., Shcherbakov, R., Tiampo, K., Gu, J., Harrington, R., Liu, Y., Baan, M. and Kao, H. 2016. Hydraulic Fracturing and Seismicity in the Western Canada Sedimentary Basin. *Seismological Research Letters*. **87**(3),pp.631–647.

Barnhart, W.D., Benz, H.M., Hayes, G.P., Rubinstein, J.L. and Bergman, E. 2014. Seismological and geodetic constraints on the 2011 Mw5.3 Trinidad, Colorado earthquake and induced deformation in the Raton Basin. *Journal of Geophysical Research: Solid Earth*. **119**(10),pp.7923–7933.

Bekaert, D., Walters, R.J., Wright, T.J., Hooper, A.J. and Parker, D.J. 2015. Statistical comparison of InSAR tropospheric correction techniques. *Remote Sensing of Environment*. **170**,pp.40–47.

Berardino, P., Fornaro, G. and Sansosti, E. 2002. A new algorithm for monitoring localized deformation phenomena based on small baseline differential SAR interferograms. *IEEE International Geoscience and Remote Sensing Symposium*. **40**(11),pp.2375–2383.

Bevis, M. and Businger, S. 1992. GPS meteorology: Remote sensing of atmospheric water vapor using the Global Positioning System. *Journal of Geophysical Research*. **97**(D14),pp.15787–15801.

Bos, M.S., Fernandes, R.M.S., Williams, S.D.P. and Bastos, L. 2013. Fast error analysis of continuous GNSS observations with missing data. *Journal of Geodesy*. **87**(4),pp.351–360.

Canada Center for Mapping and Earth Observation 2016. Fundamentals of Remote Sensing. Available from: http://www.ccrs.nrcan.gc.ca/resource/tutor/fundam/index_e.php [Accessed July 10, 2017].

Canadian Space Agency 2015. Radarsat-2 Satellite Characteristics. Available from: http://www.asc-csa.gc.ca/eng/satellites/radarsat/radarsat-tableau.asp [Accessed August 1, 2017].

Chen, Z.R. 2012. Poroelastic model for induced stresses and deformations in hydrocarbon and geothermal reservoirs. *Journal of Petroleum Science and Engineering*. **80**(1),pp.41–52.

Chirico, D. and Schirinzi, G. 2012. An extended Kalman smoothing approach for InSAR phase unwrapping *In*: *Advances in Radar and Remote Sensing*. Naples, Italy.

Costantini, M. 1998. A novel phase unwrapping method based on network programming. *Geoscience and Remote Sensing, IEEE Transactions on*. **36**(3),pp.813–821.

Curlander, J.C. and Mcdonough, R.N. 1991. *Synthetic aperture radar: systems and signal processing*. New York: Wiley.

Czarnogorska, M., Samsonov, S. and White, D. 2014. Ground deformation monitoring using RADARSAT-2 DInSAR-MSBAS at the Aquistore CO2 storage site in Saskatchewan (Canada). *ISPRS - International Archives of the Photogrammetry, Remote Sensing and Spatial Information Sciences*,pp.81–87.

DEOS 2008. Delft Object-oriented Radar Interferometric Software- User's manual and technical documentation. Available from: http://doris.tudelft.nl/usermanual/ [Accessed July 26, 2017].

Ding, X.L., Li, Z.W., Zhu, J.J., Feng, G.C. and Long, J.P. 2008. Atmospheric effects on InSAR measurements and their mitigation. *Sensors*. **8**(9),pp.5426–5448.

Eaton, D.W. 2017. Hydraulic Fracturing and Induced Seismicity *In*: *Penn State Extension Shale Education Webinar*.

Ekström, G., Nettles, M. and Dziewo Ski, A.M. 2012. The global CMT project 2004-2010: Centroid-moment tensors for 13,017 earthquakes. *Physics of the Earth and Planetary Interiors*. **200**–**201**,pp.1–9.

Ellsworth, W.L. 2013. Injection-Induced Earthquakes. *Science*. **341**(July),pp.1–8.

ESA 2017a. INTRODUCING SENTINEL-1. Available from: http://m.esa.int/Our_Activities/Observing_the_Earth/Copernicus/Sentinel-1/Introducing_Sentinel-1 [Accessed July 7, 2017].

ESA 2014. RADAR and SAR Glossary. Available from: https://earth.esa.int/handbooks/asar/CNTR5-2.html#eph.asar.gloss.radsar:SAR [Accessed August 10, 2017].

ESA 2017b. Sentinel-1A Acquisition Modes. Available from: https://sentinel.esa.int/web/sentinel/technical-guides/sentinel-1-sar/sar-instrument/acquisition-modes [Accessed August 5, 2017].

ESA 2013. Sentinel-1 User Handbook. Available from:
https://sentinel.esa.int/documents/247904/685163/Sentinel-1_User_Handbook
[Accessed July 7, 2017].

Evans, D.M. 1966. The Denver area earthquakes and the Rocky Mountain Arsenal
disposal well. *The Mountain Geologist*. **3**(1),pp.23–26.

Evenick, J. 2008. *Introduction to Well Logs and Subsurface Maps*. Tulsa, Oklahoma:
PennWell Books.

Fan, Z., Eichhubl, P. and Gale, J. 2016. Geomechanical analysis of fluid injection and
seismic fault slip for the M w 4.8 Timpson, Texas, earthquake sequence. *Journal of
Geophysical Research: Solid Earth*. **121**(4),pp.2798–2812.

Ferretti, A., Monti-Guarnieri, A., Prati, C. and Rocca, F. 2007. *InSAR Principles-
Guidelines for SAR Interferometry Processing and Interpretation*. AG Noordwijk:
ESA Publications.

Ferretti, A., Prati, C. and Rocca, F. 2001. Permanent Scatters in SAR Interferometry.
IEEE Transactions on Geoscience and Remote Sensing. **39**(1),pp.8–20.

Franceschetti, G. and Lanari, R. 1999. *Synthetic Aperture Radar Processing*. Boca Raton,
Fla: CRC Press.

Frohlich, C. and Davis, D. 2002. *Texas Earthquakes*. Austin, TX: University of Texas
Press.

Frohlich, C., Ellsworth, W., Brown, W.A., Brunt, M., Luetgert, J., MacDonald, T. and
Walter, S. 2014. The 17 May 2012 M4.8 earthquake near Timpson, East Texas: An
event possibly triggered by fluid injection. *Journal of Geophysical Research: Solid
Earth*. **119**(1),pp.581–593.

GAMMA 2008. *Differential Interferometry and Geocoding Software – DIFF&GEO*.
Gumligen, Switzerland.

GAMMA 2007. *Interferometric SAR Processing*. Gumligen, Switzerland.

GAMMA 2009. *Interferometric SAR Processor - ISP*. Gumligen, Switzerland.

Geertsma, J. 1973. Land subsidence above compacting oil and gas reservoirs. *Journal of Petroleum Technology*. (June 1973),pp.734–744.

German Aerospace Center 2014. TanDEM-X - the Earth in three dimensions. Available from: http://www.dlr.de/dlr/en/desktopdefault.aspx/tabid-10378/566_read-426/#/gallery/345.

Ghofrani, H. and Atkinson, G. 2016. A preliminary statistical model for hydraulic fracture-induced seismicity in the Western Canada Sedimentary Basin. *Geophysical Research Letters*. **43**(19),p.10,164-10,172.

Gibbs, J., Healy, J., Raleigh, C. and Coakley, J. 1973. Seismicity in the Rangely, Colorado, area: 1962-1970. *Bulletin of the Seismological Society of America*. **63**(5),pp.1557–1570.

Goldstein, R.M., Engelhardt, H., Kamb, B. and Frolich, R.M. 1993. Satellite radar interferometry for monitoring ice sheet motion—application to an Antarctic ice stream. *Science*. **262**(5139),pp.1525–1530.

Goldstein, R.M. and Werner, C.L. 1998. Radar interferogram filtering for geophysical applications. *Geophysical Research Letters*. **25**(21),pp.4035–4038.

Granata, W.H. 1963. Cretaceous Stratigraphy and Structural Development of the Sabine Uplift Area, Texas and Louisiana. *Shrevport Geological Society*,pp.50–95.

Grandin, R., Klein, E., Metois, M. and Vigny, C. 2016. Three-dimensional displacement field of the 2015 Mw8.3 Illapel earthquake (Chile) from across- and along-track Sentinel-1 TOPS interferometry. *Geophysical Research Letters*. **43**(6),pp.2552–2561.

Hansen, D.L. and O'Leary, D. 1993. The use of the L-curve in the regularization of

discrete ill-posed problems. *SIAM Journal on Scientific Computing*. **14**(6),pp.1487–1503.

Hanssen, R.F. 2001. *Radar Interferometry: Data Interpretation and Error Analysis*. Dordrecht: Springer Science & Business Media.

Haynes, M. 2017. Fast and Accurate Computation of the Multilook Interferometric Phase Probability Density Function. *IEEE Geoscience and Remote Sensing Letters*. **14**(5),pp.769–772.

Healy, J.H., Rubey, W.W., Griggs, G.T. and Raleigh, C.B. 1968. The Denver Earthquakes. *Science*. **161**(2838),pp.1301–1310.

Holland, A.A. 2013. Earthquakes triggered by hydraulic fracturing in south-central Oklahoma. *Bulletin of the Seismological Society of America*. **103**(3),pp.1784–1792.

Hooper, A., Segall, P. and Zebker, H. 2007. Persistent scatterer interferometric synthetic aperture radar for crustal deformation analysis, with application to Volcán Alcedo, Galápagos. *Journal of Geophysical Research: Solid Earth*. **112**(7),pp.1–21.

Hooper, A. and Zebker, H.A. 2007. Phase unwrapping in three dimensions with application to InSAR time series. *Journal of the Optical Society of America*. **24**(9),pp.2737–2747.

Hooper, A., Zebker, H., Segall, P. and Kampes, B. 2004. A new method for measuring deformation on volcanoes and other natural terrains using InSAR persistent scatterers. *Geophysical Research Letters*. **31**(23).

Jackson, M.P.A. 1982. *Fault Tectonics of the East Texas Basin*. Austin, TX: Bureau of Economic Geology.

Kavanagh, P. 1985. Doppler centroid ambiguity estimation for synthetic aperture radar. *PhD Thesis, University of British Columbia*.

Kenyi, L.. and Kaufmann, V. 2003. Measuring rock glacier surface deformation using

SAR interferometry *In*: *Proceedings of the 8th Int. Permafrost Conf. Zurich*. Switzerland.

Keranen, K.M., Savage, H.M., Abers, G.A. and Cochran, E.S. 2013. Potentially induced earthquakes in Oklahoma, USA: Links between wastewater injection and the 2011 Mw 5.7 earthquake sequence. *Geology*. **41**(6),pp.699–702.

Keranen, K.M., Weingarten, M., Abers, G.A., Bekins, B.A. and Ge, S. 2014. Sharp increase in central Oklahoma seismicity since 2008 induced by massive wastewater injection. *Science*. **345**(6195),pp.448–451.

Kramer, J.H. 2014. TSX (TerraSAR-X) Mission. Available from: https://directory.eoportal.org/web/eoportal/satellite-missions/t/terrasar-x [Accessed October 9, 2014].

Lanari, R., Lundgren, P., Manzo, M. and Casu, F. 2004. Satellite radar interferometry time series analysis of surface deformation for Los Angeles, California. *Geophysical Research Letters*. **31**(L23613),pp.1–5.

Li, Z. and Bethel, J. 2008. Image coregistration in SAR interferometry. *Internation Archives of Photogrammetry Remote Sensing And Spatial Information Sciences*. **37**(1),pp.433–438.

Massonnet, D. and Feigl, K.L. 1998. Radar interferometry and its application to changes in the Earth's surface. *Reviews of Geophysics*. **36**(97),pp.441–500.

Massonnet, D., Rossi, M., Carmona, C., Adragna, F., Peltzer, G., Feigl, K. and Rabaute, T. 1993. The displacement field of the Landers earthquake mapped by radar interferometry. *Nature*. **364**,pp.138–142.

McGarr, A., Bekins, B., Burkardt, N., Dewey, J., Earle, P., Ellsworth, W., Ge, S., Hickman, S., Holland, A., Majer, E., Rubinstein, J. and Sheehan, A. 2015. Coping with earthquakes induced by fluid injection. *Science*. **347**(6224),pp.830–831.

Motagh, M., Djamour, Y., Walter, T.R., Wetzel, H.U., Zschau, J. and Arabi, S. 2007.

Land subsidence in Mashhad Valley, northeast Iran: Results from InSAR, levelling and GPS. *Geophysical Journal International*. **168**(2),pp.518–526.

Le Mouélic, S., Raucoules, D., Carnec, C. and King, C. 2002. A ground uplift in the city of Paris (France) detected by satellite radar interferometry. *Geophysical Research Letters*. **29**(17),pp.1–4.

Natural Resources Canada 2014. Polarization in radar systems. Available from: http://www.nrcan.gc.ca/node/9567 [Accessed August 5, 2017].

Nishiguchi, T., Tsuchiya, S. and Imaizumi, F. 2017. Detection and accuracy of landslide movement by InSAR analysis using PALSAR-2 data. *Landslides*. **14**(4),pp.1483–1490.

Parker, A.L., Biggs, J., Walters, R.J., Ebmeier, S.K., Wright, T.J., Teanby, N.A. and Lu, Z. 2015. Systematic assessment of atmospheric uncertainties for InSAR data at volcanic arcs using large-scale atmospheric models: Application to the Cascade volcanoes, United States. *Remote Sensing of Environment*. **170**,pp.102–114.

Railroad Commission of Texas 2015. Annual Disposal/Injection Well Monitoring Report (Form H-10) Online Filing. Available from: http://www.rrc.state.tx.us/about-us/resource-center/research/online-research-queries/about-h-10-query/ [Accessed June 8, 2017].

Refice, A., Satalino, G., Stramaglia, S., Chiaradia, M.T. and Veneziani, N. 1999. Weights determination for minimum cost flow InSAR phase unwrapping. *International Geoscience and Remote Sensing Symposium (IGARSS)*. **2**,pp.1342–1344.

Rubinstein, J.L. and Mahani, A.B. 2015. Myths and Facts on Wastewater Injection, Hydraulic Fracturing, Enhanced Oil Recovery, and Induced Seismicity. *Seismological Research Letters*. **86**(4),pp.1060–1067.

Samsonov, S. 2007. Integration of Differential InSAR and GPS measurements for studying of surface deformation. *PhD Thesis, Western University*.

Samsonov, S., Czarnogorska, M. and Charbonneau, F. 2015. Selecting Optimal RADARSAT Constellation Mission Beams for Monitoring Ground Deformation in Albertas Oil Sands. *Canadian Journal of Remote Sensing*. **41**(5),pp.390–400.

Samsonov, S. and D'Oreye, N. 2017. Multidimensional Small Baseline Subset (MSBAS) for two-dimensional deformation analysis. Case study Mexico City. *Canadian Journal of Remote Sensing*. **43**(4),pp.318–329.

Samsonov, S. and D'Oreye, N. 2012. Multidimensional time-series analysis of ground deformation from multiple InSAR data sets applied to Virunga Volcanic Province. *Geophysical Journal International*. **191**,pp.1095–1108.

Samsonov, S., D'Oreye, N., Gonzalez, P.J., Tiampo, K., Ertolahti, L. and Clague, J. 2014. Rapidly accelerating subsidence in the Greater Vancouver region from two decades of ERS-ENVISAT-RADARSAT-2 DInSAR measurements. *Remote Sensing of Environment*. **143**,pp.180–191.

Samsonov, S., D'Oreye, N. and Smets, B. 2013. Ground deformation associated with post-mining activity at the French-German border revealed by novel InSAR time series method. *International Journal of Applied Earth Observation and Geoinformation*. **23**,pp.142–154.

Samsonov, S., Feng, W., Peltier, A., Geirsson, H., D'Oreye, N. and Tiampo, K. 2017. Multidimensional Small Baseline Subset (MSBAS) for volcano monitoring in two dimensions: opportunities and challenges. Case study Piton de la Fournaise volcano. *Journal of Volcanology and Geothermal Research*. **344**,pp.121–138.

Samsonov, S., van der Kooij, M. and Tiampo, K. 2011. A simultaneous inversion for deformation rates and topographic errors of DInSAR data utilizing linear least square inversion technique. *Computers and Geosciences*. **37**(8),pp.1083–1091.

Samsonov, S., Tiampo, K. and Feng, W. 2016. Fast subsidence in downtown of Seattle observed with satellite radar. *Remote Sensing Applications: Society and Environment*. **4**,pp.179–187.

Santoro, M., Wegmuller, U., Strozzi, T., Askne, J. and Fransson, J. 2009. Examples of thematic mapping with ERS-Envisat tandem cross-interferometry *In*: *ESA: Fringe 2009 Workshop*. Frascati, Italy.

Sarti, F., Vadon, H. and Massonnet, D. 1999. A method for the automatic characterization of InSAR atmospheric artifacts by correlation of multiple interferograms over the same site. *IEEEInternational Geoscience and Remote Sensing Symposium, IGARSS '99*. **4**,pp.1937–1939.

Satellite Imaging Corporation 2017. GeoEye-1 Satellite Sensor. Available from: http://www.satimagingcorp.com/satellite-sensors/geoeye-1/ [Accessed July 1, 2017].

Scheiber, R. and Moreira, A. 2000. Coregistration of interferometric SAR images using spectral diversity. *IEEE Transactions on Geoscience and Remote Sensing*. **38**(5),pp.2179–2191.

Schlumberger 2017. Oilfield Glossary. Available from: http://www.glossary.oilfield.slb.com/Terms/w/well_log.aspx [Accessed August 5, 2017].

Schneevoigt, N.J., Sund, M., Bogren, W., Kääb, A. and Weydahl, D.J. 2012. Glacier displacement on Comfortlessbreen, Svalbard, using 2-pass differential SAR interferometry (DInSAR) with a digital elevation model. *Polar Record*. **48**(244),pp.17–25.

Scholz, C.H. 2002. *The Mechanics of Earthquakes and Faulting*. Cambridge, UK: Cambridge University Press.

Schultz, R., Stern, V., Novakovic, M., Atkinson, G. and Gu, Y. 2015. Hydraulic fracturing and the Crooked Lake Sequences: Insights gleaned from regional seismic networks. *Geophysical Research Letters*. **42**,pp.2750–2758.

Schultz, R., Wang, R., Gu, Y., Haug, K. and Atkinson, G. 2017. A seismological overview of the induced earthquakes in the Duvernay play near Fox Creek, Alberta. *Journal of Geophysical Research: Solid Earth*. **122**(1),pp.492–505.

Shirzaei, M., Ellsworth, W.L., Tiampo, K.F., González, P.J., Manga, M., Gonzalez, P.J. and Manga, M. 2016. Surface uplift and time-dependent seismic hazard due to fluid injection in eastern Texas. *Science*. **353**(6306),pp.1416–1419.

Simon, R.B. 1969. Seismicity of Colorado: Consistency of Recent Earthquakes with Those of Historical Record. *Source: Science, New Series*. **165**(3896),pp.897–899.

Sowter, A., Bin Che Amat, M., Cigna, F., Marsh, S., Athab, A. and Alshammari, L. 2016. Mexico City land subsidence in 2014–2015 with Sentinel-1 IW TOPS: Results using the Intermittent SBAS (ISBAS) technique. *International Journal of Applied Earth Observation and Geoinformation*. **52**,pp.230–242.

Thapa, S. and Chatterjee, R.S. 2015. Estimation of atmospheric effects of Radarsat-2 D-InSAR product using groundbasedand spaceborne meterological data *In*: *International Archives of the Photogrammetry, Remote Sensing and Spatial Information Sciences - ISPRS Archives*. Munich, Germany, pp. 243–246.

The Academy of Medicine Engineering and Science of Texas 2017. *Environmental and Community Impacts of Shale Development in Texas*. Austin, TX: The Academy of Medicine, Engineering and Science of Texas.

Tikhonov, A.N. and Arsenin, V.Y. 1977. *Solution of ill=posed problems*. Washington, DC: Winston and Sons.

Touzi, R., Lopes, A., Bruniquel, J. and Vachon, P.W. 1999. Coherence estimation for SAR imagery. *IEEE Transactions on Geoscience and Remote Sensing*. **37**(1),pp.135–149.

Triyana, Y. 2003. Characterization of Rodessa Formation (Lower Cretaceous) in Van Field, Van Zandt County, Texas. *MSc. Thesis, Texas A&M University*.

USGS 1794. *Anhydrite Deposits of the United States and Characteristics of Anhydrite Important for Storage of Radioactive Wastes*. Denver, CO: Books and Open-File Reports Section.

USGS 2017. LP DAAC - Global Data Explorer. Available from: https://gdex.cr.usgs.gov/gdex/ [Accessed July 7, 2016].

Vasco, D.W., Karasaki, K. and Myer, L. 1998. Monitoring of Fluid Injection and Soil Consolidation Using Surface Tilt Measurements. *Journal of Geotechnical and Geoenvironmental Engineering*. **124**(1),pp.29–37.

Vasco, D.W., Rucci, A., Ferretti, A., Novali, F., Bissell, R.C., Ringrose, P.S., Mathieson, A.S. and Wright, I.W. 2010. Satellite-based measurements of surface deformation reveal fluid flow associated with the geological storage of carbon dioxide. *Geophysical Research Letters*. **37**,pp.1–5.

Wegmuller, U. and Werner, C.L. 1997. Gamma SAR processor and interferometry software *In*: *Third ERS Symposium on Space at the service of our Environment*. Florence, Italy.

Wegmüller, U., Werner, C.L., Strozzi, T. and Wiesmann, A. 2004. Multi-temporal Interferometric Point Target Analysis. *Series in Remote Sensing*. **3**,pp.136–144.

Wegmüller, U., Werner, C.L., Strozzi, T., Wiesmann, A., Frey, O. and Santoro, M. 2015. Sentinel-1 support in the GAMMA Software *In*: *Fringe 2015 Conference*. Frascati, Italy.

Weingarten, M., Ge, S., Godt, J.W., Bekins, B.A. and Rubinstein, J.L. 2015. High-rate injection is associated with the increase in U.S. mid-continent seismicity. *Science*. **348**(6241),pp.1336–1340.

Weissel, J.K., Czuchlewski, K.R. and Kim, Y. 2004. Synthetic aperture radar (SAR) - based mapping of volcanic flows : Manam Island , Papua New Guinea. ,pp.339–346.

Wempen, J.M. and McCarter, M.K. 2017. Comparison of L-band and X-band differential interferometric synthetic aperture radar for mine subsidence monitoring in central Utah. *International Journal of Mining Science and Technology*. **27**(1),pp.159–163.

Werner, C.L., Wegmuller, U. and Strozzi, T. 2002. Processing Strategies for Phase

Unwrapping for InSAR Applications *In*: *Proceedings of the 4th European Conference on Synthetic Aperture Radar.*

Werner, M. 2001. Shuttle radar topography mission (SRTM): experience with the X-band SAR interferometer *In*: *2001 CIE International Conference on Radar Proceedings*. Beijing, China, pp. 634–638.

Wessel, P., Smith, W., Scharroo, R., Luis, J. and Wobbe, F. 2013. Generic Mapping Tools: Improved version released. *EOS Trans. AGU*. **94**(45),pp.409–410.

Wright, T.J. 2002. Remote monitoring of the earthquake cycle using satellite radar interferometry. *Philosophical transactions. Series A, Mathematical, physical, and engineering sciences*. **360**,pp.2873–2888.

Wright, T.J., Fielding, E.J. and Parsons, B. 2001. Triggered slip: observations of the 17 august 1999 İzmit (Turkey) earthquake using radar interferometry. *Geophysical Research Letters*. **28**(6),pp.1079–1082.

Yague-Martinez, N., Prats-Iraola, P., Gonzalez, F.R., Brcic, R., Shau, R., Geudtner, D., Eineder, M. and Bamler, R. 2016. Interferometric Processing of Sentinel-1 TOPS Data. *IEEE Transactions on Geoscience and Remote Sensing*. **54**(4),pp.2220–2234.

Yeck, W.L., Hayes, G.P., McNamara, D.E., Rubinstein, J.L., Barnhart, W.D., Earle, P.S. and Benz, H.M. 2017. Oklahoma experiences largest earthquake during ongoing regional wastewater injection hazard mitigation efforts. *Geophysical Research Letters*. **44**(2),pp.711–717.

Zebker, H.A. and Goldstein, R.M. 1986. Topographic mapping from interferometric synthetic aperture radar observations. *Journal of Geophysical Research*. **91**(B5),pp.4993–4999.

Zebker, H.A., Rosen, P.A. and Hensley, S. 1997. Atmospheric effects in interferometric synthetic aperture radar surface deformation and topographic maps. *Journal of Geophysical Research*. **102**,pp.7547–7563.

Zebker, H.A., Rosen, P., Goldstein, M., Gabriel, A. and Werner, C.L. 1994. On the derivation of coseismic displacement fields using differential radar interferometry: The Landers earthquake. *Journal of Geophysical Research*. **99**(B10),pp.19617–19634.

Zebker, H.A. and Villasenor, J. 1992. Decorrelation in interferometric radar echoes. *IEEE Transactions on Geoscience and Remote Sensing*. **30**(5),pp.950–959.

Zink, M. 2003. The TerraSAR-L Interferometric Mission Objectives *In*: *FRINGE 2003 Workshop*. Florence, Italy.

van Zyle, J. 2016. *Interferometric Synthetic Aperture Radar*, Lecture Slide, Introduction to the Physics of Remote Sensing EE/Ae 157, Caltech University. Available from: http://www.its.caltech.edu/~ee157/lecture_note/Interferometry.pdf [Accessed July 4 2017]

Appendices

Appendix A: DInSAR RADARSAT-2 Processing Script

```
#!/usr/bin/env tcsh
# Script to run RADARSAT-2 images using GAMMA
# Author: Simon Thorpe, modified after S. Samsonov
# 10/05/2017

# Source GAMMA directory
source /usr/local/bin/use_gamma-20160625.csh

# Convert .tif files to SLC format
par_RSAT2_SLC product.xml lutSigma.xml imagery_HH.tif HH 20090225_HH.slc.par 20090225_HH.slc

# View the SLC file using disSLC
# Check width of SLC (5158) and SLC format (S or F-COMPLEX) in .par files
disSLC 20110322_HH.slc 7378 1 0:7378 1. .35 0

#################################################
# Create DEMs
# Use SLC_corners to find size of DEM
# Download DEM in .tif format from www.gdex.cr.usgs.gov - already mosaiced
# Use srtm2dem to convert to GAMMA accepted format
# This creates DEM parameter file already - make sure inout geoid (egm96_wgs84_diff.tif) is in current directory
srtm2dem 20160616112027_691293285.tif DEM DEM_par 2 egm96_wgs84_diff.tif

# Display DEM with shaded relief including pixel coordinates
disdem_par DEM DEM_par

# Tell GAMMA where to find the DEM and parameter file
set dem = /home/sthorpe5/Data/RADARSAT-2/Location38/Standard/DEM/DEM
set dempar = /home/sthorpe5/Data/RADARSAT-2/Location38/Standard/DEM/DEM_par

#################################################
# Define the multilooking factor
# Match the resolution of DEM
set rlks = 2
set azlks = 6

#################################################
# Define master SLC
# Based on smallest baseline / highest quality / similar time of year
# Different master for different wide / standard
set master = 20140524_VV

#################################################
# Define region that we want to match on the SLC image
# A region in the middle of the image with high coherence / persistant scatterer visible in all images
set rpos = 4897
set azpos = 16711

#################################################
# Put all the SLC files in the same directory (SLC)
# Create SLC_tab - a list of all the SLCs and parameter files
ls *.slc > slc
ls *.slc.par > par
paste slc par > SLC_tab
rm slc par

#################################################
# Estimate baselines
# Make sure the executable - base_calc is copied from the GAMMA directory to the current directory
./base_calc SLC_tab $master.slc.par bperp_file itab 1 - 0 2500 1 -

#################################################
# Multilook the SLC images using the predefined parameters
```

```
# Copy the executable mk_mli_all to the current working directory
./mk_mli_all SLC_tab ml $rlks $azlks 0

# View .mli images using dispwr <filename.mli> <width>

#################################################
# Convert DEM to radar co-ordinates
# Works if you don't specify an rpos and azpos to use
mk_geo $master.mli $master.mli.par $dem $dempar geo/ni_seg.dem geo/ni_seg.dem_par geo ni 0.000278 0 3 64
#mk_geo $master.mli $master.mli.par $dem $dempar geo/ni_seg.dem geo/ni_seg.dem_par geo ni 0.000278 1 3 64 # Use for long baselines
mk_geo $master.mli $master.mli.par $dem $dempar geo/ni_seg.dem geo/ni_seg.dem_par geo ni 0.000278 2 3 64
mk_geo $master.mli $master.mli.par $dem $dempar geo/ni_seg.dem geo/ni_seg.dem_par geo ni 0.000278 3 3 64
mk_geo $master.mli $master.mli.par $dem $dempar geo/ni_seg.dem geo/ni_seg.dem_par geo ni 0.000278 4 3 64

#################################################
# Coregister and resample all SLC images
# Within SLC directory - creates RSLSC directory within
SLC_resamp_all SLC_tab $master.slc $master.slc.par rslc RSLC_tab 0 1
SLC_resamp_all SLC_tab $master.slc $master.slc.par rslc RSLC_tab 1 1
SLC_resamp_all SLC_tab $master.slc $master.slc.par rslc RSLC_tab 2 1
SLC_resamp_all SLC_tab $master.slc $master.slc.par rslc RSLC_tab 3 1
SLC_resamp_all SLC_tab $master.slc $master.slc.par rslc RSLC_tab 4 1

# View .rslc images using disSLC 20110322_HH.rslc 7378 1 0:7378 1. .35 0

#################################################
# Create multilook master images (coregistered)
# Puts all multi looked images in rmli directory within rslc directory - had to change RSLC_tab directories after copying it over

# Create list of images to be averaged in file called ave_list in a column
# create an average image of all the rslcs
ave_image ave_list 5158 ave_im

./mk_mli_all RSLC_tab . $rlks $azlks 1 0.8 0.35 ave_im

# View .rmli images using dispwr <filename.rmli> <width>

#################################################
# Calculating differential interferograms
# Run inside rslc directory and copying everything from rmli into it
cp ../itab .
set rpos = 1221
set azpos = 833
mk_diff_2d RSLC_tab itab 0 ../../geo/ni_dem.rdc - $master.rmli . dint $rlks $azlks 5 1 1 0 $rpos $azpos

#  Look up width in dint/*.off!!
#  Can look at differential interferograms using 'dismph filename.diff 2450', where 2450 is the width from the *.off file

#################################################
# Filtering differential interferograms
# Run inside rslc directory
mk_adf_2d RSLC_tab itab $master.rmli dint/ 7 - - - - -

#################################################
# Unwrapping the differential interferograms
# Run inside rslc directory
mk_unw_2d RSLC_tab itab $master.rmli dint 0.4 0 1 1 1 1 - - 1 -

#################################################
# Calculate refined orbits
mk_base_2d RSLC_tab itab ../../geo/ni_dem.rdc dint/ pbaseline_refined

#################################################
# Create dint_refined folder inside rslc directory
mkdir dint_refined
cp dint/*.base dint_refined/
# Calculate new differential interferograms using precice orbits
mk_diff_2d RSLC_tab itab 1 ../../geo/ni_dem.rdc - $master.rmli . dint_refined $rlks $azlks 5 1 1 2
```

```
##################################################
# Filtering the refined interferograms
mk_adf_2d RSLC_tab itab $master.rmli dint_refined 7 - - - - -

##################################################
# Phase unwrapping of the refined interferograms
mk_unw_2d RSLC_tab itab $master.rmli dint_refined 0.4 - 1 1 1

# Run phase unwrapping again with higher cc threshold (was 0.3 )
# mk_unw_2d RSLC_tab itab $master.rmli dint_refined 0.5 - 1 1 1

# Viewing unrwapped ifgs in raster file
rasrmg 20140330_HH_20140423_HH.adf.unw ../20140330_HH.rmli 2103 - - - 4 4 1 - - - -
20140330_HH_20140423_HH.adf.unw.ras4

##################################################
# Defining some parameters inside rslc directory
set width = `awk '$1 == "range_samples:" {print $2}' $master.rmli.par`
set length = `awk '$1 == "azimuth_lines:" {print $2}' $master.rmli.par`
set width_dem = `awk '$1 == "width:" {print $2}' ../../geo/ni_seg.dem_par`
set length_dem = `awk '$1 == "nlines:" {print $2}' ../../geo/ni_seg.dem_par`
set lat = `awk '$1 == "corner_lat:" {print $2}' ../../geo/ni_seg.dem_par`
set lon = `awk '$1 == "corner_lon:" {print $2}' ../../geo/ni_seg.dem_par`
set latstep = `awk '$1 == "post_lat:" {print $2}' ../../geo/ni_seg.dem_par`
set lonstep = `awk '$1 == "post_lon:" {print $2}' ../../geo/ni_seg.dem_par`
set lat1 = `echo $lat $latstep $length_dem | awk '{print ($1+$2*$3);}'`
set lon1 = `echo $lon $lonstep $width_dem | awk '{print ($1+$2*$3);}'`

##################################################
# Geocode wrapped phase
# Run inside rslc directory
# Copy mk_kml to current directory
foreach file (dint_refined/*.adf.diff)
geocode_back $file $width ../../geo/ni_1.map_to_rdc $file.geo $width_dem 0 0 1
rasmph_pwr $file.geo ../../geo/ni_map.mli $width_dem 1 1 0 1 1 .8 .35
convert $file.geo.ras -quality 100%  $file.geo.jpg
mk_kml ../../geo/ni_seg.dem_par $file.geo.jpg $file.geo.jpg.kml
end

##################################################
# Geocode coherence
# Run inside rslc
foreach file (dint_refined/*.adf.cc)
geocode_back $file $width ../../geo/ni_1.map_to_rdc $file.geo $width_dem 0 0 0
rascc $file.geo ../../geo/ni_map.mli $width_dem
convert $file.geo.ras -quality 100%  $file.geo.jpg
mk_kml ../../geo/ni_seg.dem_par $file.geo.jpg $file.geo.jpg.kml
end

##################################################
# Geocode unwrapped phase and convert to displacement
# Run inside rslc
foreach file (dint_refined/*.adf.unw)
set off = `echo $file | awk '{sub(/.adf.unw/,""); print;}'`
dispmap $file - ../$master.slc.par $off.off $off.disp 0
geocode_back $off.disp $width ../../geo/ni_1.map_to_rdc $off.disp.geo $width_dem 0 0 0
rascc $off.disp.geo ../../geo/ni_map.mli $width_dem
convert $off.disp.geo.ras -quality 100%  $off.disp.geo.jpg
mk_kml ../../geo/ni_seg.dem_par $off.disp.geo.jpg $off.disp.geo.jpg.kml
end

# View displacement file .disp using dishgt
# dishgt 20140330_HH_20140423_HH.disp ../20140330_HH.rmli 2103 1 1 0 0.02
# View in ras file
# rashgt 20140330_HH_20140423_HH.disp ../20140330_HH.rmli 2103 - - - 1 1 0.02 - - - 20140330_HH_20140423_HH.disp.ras2
```

Appendix B: DInSAR ALOS and ALOS-2 Processing Script

```
#!/usr/bin/env tcsh
# Script to process ALOS PALSAR level 1.1 data
source /usr/local/bin/use_gamma-20170706.csh

# Convert to SLC
par_EORC_PALSAR LED-ALPSRP090750620-H1.1__A 20071008_HH.slc.par PRODUCT31/IMG-HH-ALPSRP090750620-
H1.1__A 20071008_HH.slc

# Oversample FBD by factor of 2 to convert to FBS
SLC_ovr_all SLC_tab FBD_OVR 2 SLC_tab_OVR # For FBD images only
mv *.slc ../SLC
mv *.slc.par ../SLC

set master = 20070506

# Concatenate frames using
SLC_cat_all SLC_620_tab SLC_630_tab cslc CSLC_tab 0 1 2650 18175
SLC_cat_all SLC_620_tab SLC_630_tab cslc CSLC_tab 1 1 2650 18175
SLC_cat_all SLC_620_tab SLC_630_tab cslc CSLC_tab 2 1 2650 18175
SLC_cat_all SLC_620_tab SLC_630_tab cslc CSLC_tab 3 1 2650 18175
SLC_cat_all SLC_620_tab SLC_630_tab cslc CSLC_tab 4 1 2650 18175

# Crop mosaiced SLC to region of interest
set croff = 0          # Starting range offset
set cloff = 9500       # Starting line offset
set cnl = 17000        # Set number of lines to process
SLC_copy_all CSLC_tab SLCCOPY $croff - $cloff $cnl

# Moving cropped SLCs
mkdir cslc
mv *_crop.slc cslc/
mv *_crop.slc.par cslc/
# Rename files to remove *_crop* extension

# Baselines
cd cslc
ls *.slc > slc
ls *.slc.par > par
paste slc par > SLC_tab
rm slc par
base_calc SLC_tab $master.slc.par bperp_file itab 1 1 0 2500 1 -

# Multilook
set rlks = 6
set azlks = 10
mk_mli_all SLC_tab ml $rlks $azlks 0
cp ml/$master.mli ../../
cp ml/$master.mli.par ../../

# DEM
cd ../DEM/
cp /usr/local/GAMMA_SOFTWARE-20170706/DIFF/scripts/egm96_wgs84_diff.tif .
srtm2dem 20160616112027_691293285.tif DEM DEM_par 2 egm96_wgs84_diff.tif
set dem = /home/sthorpe5/Data/ALOS/620_172/DEM/DEM
set dempar = /home/sthorpe5/Data/ALOS/620_172/DEM/DEM_par
cd ../
mk_geo $master.mli $master.mli.par $dem $dempar geo/ni_seg.dem geo/ni_seg.dem_par geo ni 0.000278 0 3 64
mk_geo $master.mli $master.mli.par $dem $dempar geo/ni_seg.dem geo/ni_seg.dem_par geo ni 0.000278 1 3 64
mk_geo $master.mli $master.mli.par $dem $dempar geo/ni_seg.dem geo/ni_seg.dem_par geo ni 0.000278 2 3 64
mk_geo $master.mli $master.mli.par $dem $dempar geo/ni_seg.dem geo/ni_seg.dem_par geo ni 0.000278 3 3 64
mk_geo $master.mli $master.mli.par $dem $dempar geo/ni_seg.dem geo/ni_seg.dem_par geo ni 0.000278 4 3 64

# Coregister
```

```
set rpos = 3207
set azpos = 5326
cd SLC/
SLC_resamp_all SLC_tab $master.slc $master.slc.par rslc RSLC_tab 0 1 - - $rpos $azpos
SLC_resamp_all SLC_tab $master.slc $master.slc.par rslc RSLC_tab 1 1 - - $rpos $azpos
SLC_resamp_all SLC_tab $master.slc $master.slc.par rslc RSLC_tab 2 1 - - $rpos $azpos
SLC_resamp_all SLC_tab $master.slc $master.slc.par rslc RSLC_tab 3 1 - - $rpos $azpos
SLC_resamp_all SLC_tab $master.slc $master.slc.par rslc RSLC_tab 4 1 - - $rpos $azpos

# Multilook coregistered SLCs
# emacs ave_list #name each rslc file to be multilooked
ave_image ave_list 4640 ave_im
mk_mli_all RSLC_tab . $rlks $azlks 1 0.8 0.35 ave_im

# Differential ifgs
cp ../itab .
mk_diff_2d RSLC_tab itab 0 ../../geo/ni_dem.rdc - $master.rmli . dint $rlks $azlks 5 1 1 0

# Filter ifgs
mk_adf_2d RSLC_tab itab $master.rmli dint/ 7 - - - - -
# Unwrapping the differential interferograms
mk_unw_2d RSLC_tab itab $master.rmli dint 0.4 0 1 1 1 1 - - 1

#################################################################
# Refined orbits
#################################################################
mk_base_2d RSLC_tab itab ../../geo/ni_dem.rdc dint/ pbaseline_refined
# mkdir dint_refined
cp dint/*.base dint_refined/
# Differential ifgs
mk_diff_2d RSLC_tab itab 1 ../../geo/ni_dem.rdc - $master.rmli . dint_refined $rlks $azlks 5 1 1 2
# Filtering ifgs
mk_adf_2d RSLC_tab itab $master.rmli dint_refined 7 - - - - -
# Unwrap ifgs
mk_unw_2d RSLC_tab itab $master.rmli dint_refined 0.4 - 1 1 1
#################################################################

# Set parameters in rslc directory
set width = `awk '$1 == "range_samples:" {print $2}' $master.rmli.par`
set length = `awk '$1 == "azimuth_lines:" {print $2}' $master.rmli.par`
set width_dem = `awk '$1 == "width:" {print $2}' ../../geo/ni_seg.dem_par`
set length_dem = `awk '$1 == "nlines:" {print $2}' ../../geo/ni_seg.dem_par`
set lat = `awk '$1 == "corner_lat:" {print $2}' ../../geo/ni_seg.dem_par`
set lon = `awk '$1 == "corner_lon:" {print $2}' ../../geo/ni_seg.dem_par`
set latstep = `awk '$1 == "post_lat:" {print $2}' ../../geo/ni_seg.dem_par`
set lonstep = `awk '$1 == "post_lon:" {print $2}' ../../geo/ni_seg.dem_par`
set lat1 = `echo $lat $latstep $length_dem | awk '{print ($1+$2*$3);}'`
set lon1 = `echo $lon $lonstep $width_dem | awk '{print ($1+$2*$3);}'`

#################################################################
# Geocoding
#################################################################
# Wrapped phase
foreach file (dint_refined/*.adf.diff)
geocode_back $file $width ../../geo/ni_1.map_to_rdc $file.geo $width_dem 0 0 1
rasmph_pwr $file.geo ../../geo/ni_map.mli $width_dem 1 1 0 1 1 .8 .35
convert $file.geo.ras -quality 100% $file.geo.jpg
mk_kml ../../geo/ni_seg.dem_par $file.geo.jpg $file.geo.jpg.kml
end

# Coherence # Skipped this to save space
#foreach file (dint_refined/*.adf.cc)
#geocode_back $file $width ../../geo/ni_1.map_to_rdc $file.geo $width_dem 0 0 0
#rascc $file.geo ../../geo/ni_map.mli $width_dem
#convert $file.geo.ras -quality 100% $file.geo.jpg
#mk_kml ../../geo/ni_seg.dem_par $file.geo.jpg $file.geo.jpg.kml
#end

# Unwrapped phase
foreach file (dint_refined/*.adf.unw)
```

```
geocode_back $file $width ../../geo/ni_1.map_to_rdc $file.geo $width_dem 0 0 0
rasrmg $file.geo ../../geo/ni_map.mli $width_dem
convert $file.geo.ras -quality 100% $file.geo.jpg
mk_kml ../../geo/ni_seg.dem_par $file.geo.jpg $file.geo.jpg.kml
end


# Displacement map
foreach file (dint_refined/*.adf.unw)
set off = `echo $file | awk '{sub(/.adf.unw/,""); print;}'`
dispmap $file - ../$master.slc.par $off.off $off.disp 0
geocode_back $off.disp $width ../../geo/ni_1.map_to_rdc $off.disp.geo $width_dem 0 0 0
rashgt $off.disp.geo ../../geo/ni_map.mli $width_dem - - - 1 1 0.03
convert $off.disp.geo.ras -quality 100% $off.disp.geo.jpg
mk_kml ../../geo/ni_seg.dem_par $off.disp.geo.jpg $off.disp.geo.jpg.kml
end
```

Appendix C: DInSAR Sentinel-1 Pre-Processing Script

```
#!/bin/bash
# Convert Sentinel-1 IW mode to SLC files
# Including deramping and multilook mosaicing
# #############
# NOTE for Rocky Mountain House only IW2 used (IW1+IW3 commented out)
# #############
# Author: Simon Thorpe

list=$(<SLC_list.txt)
SLCs=($list)
N_SLCs=${#SLCs[@]}

mkdir -p DInSAR/SLCs
mkdir -p DInSAR/IMG/IMG_mli

for (( i=0; i<${N_SLCs}; i++ ))
do

scene_id=`echo ${SLCs[$i]}`
echo $scene_id
cd $scene_id

###################################################
### Generating .slc .slc.par .slc.TOPS_par files ###
###################################################

cd measurement
IW1=`find . -name "*.tiff" | grep "s1a-iw1-slc-vv"`
IW2=`find . -name "*.tiff" | grep "s1a-iw2-slc-vv"`
IW3=`find . -name "*.tiff" | grep "s1a-iw3-slc-vv"`

cd ../annotation
IW1_ann=`find -maxdepth 1 -name "*.xml" | grep "s1a-iw1-slc-vv"`
IW2_ann=`find -maxdepth 1 -name "*.xml" | grep "s1a-iw2-slc-vv"`
IW3_ann=`find -maxdepth 1 -name "*.xml" | grep "s1a-iw3-slc-vv"`

cd calibration
IW1_cal=`find . -name "*.xml" | grep "calibration-s1a-iw1-slc-vv"`
IW2_cal=`find . -name "*.xml" | grep "calibration-s1a-iw2-slc-vv"`
IW3_cal=`find . -name "*.xml" | grep "calibration-s1a-iw3-slc-vv"`

IW1_noi=`find . -name "*.xml" | grep "noise-s1a-iw1-slc-vv"`
IW2_noi=`find . -name "*.xml" | grep "noise-s1a-iw2-slc-vv"`
IW3_noi=`find . -name "*.xml" | grep "noise-s1a-iw3-slc-vv"`

cd ../../

#par_S1_SLC */$IW1 */$IW1_ann */*/$IW1_cal */*/$IW1_noi $scene_id.iw1.slc.par $scene_id.iw1.slc $scene_id.iw1.slc.TOPS_par
par_S1_SLC */$IW2 */$IW2_ann */*/$IW2_cal */*/$IW2_noi $scene_id.iw2.slc.par $scene_id.iw2.slc $scene_id.iw2.slc.TOPS_par
```

```
#par_S1_SLC */$IW3 */$IW3_ann */*/$IW3_cal */*/$IW3_noi $scene_id.iw3.slc.par $scene_id.iw3.slc $scene_id.iw3.slc.TOPS_par

#echo $scene_id.iw1.slc $scene_id.iw1.slc.par $scene_id.iw1.slc.TOPS_par > SLC_tab
echo $scene_id.iw2.slc $scene_id.iw2.slc.par $scene_id.iw2.slc.TOPS_par > SLC_tab
#echo $scene_id.iw3.slc $scene_id.iw3.slc.par $scene_id.iw3.slc.TOPS_par >> SLC_tab

##############################################
### Azimuth spctrum deramping ###
##############################################

#echo $scene_id.iw1.slc.deramp $scene_id.iw1.slc.deramp.par $scene_id.iw1.slc.deramp.TOPS_par > SLC_tab_deramp
echo $scene_id.iw2.slc.deramp $scene_id.iw2.slc.deramp.par $scene_id.iw2.slc.deramp.TOPS_par > SLC_tab_deramp
#echo $scene_id.iw3.slc.deramp $scene_id.iw3.slc.deramp.par $scene_id.iw3.slc.deramp.TOPS_par >> SLC_tab_deramp
SLC_deramp_S1_TOPS SLC_tab SLC_tab_deramp 0 1


##############################################
### Multilooking and mosaicing of the iw1,iw2 and iw3 bursts ###
##############################################

rlks=12        #Number of range looks
azlks=2        #Number of azimuth looks

multi_S1_TOPS SLC_tab_deramp $scene_id.mli $scene_id.mli.par $rlks $azlks
SLC_mosaic_S1_TOPS SLC_tab_deramp $scene_id.slc $scene_id.slc.par $rlks $azlks

width_ml=`awk '/range_samples/' $scene_id.mli.par | awk -F ' ' '{print $2}'`
raspwr $scene_id.mli $width_ml - - - - - - -1 $scene_id.mli.tif

##############################################
### Copying slc and mli files to the same directory ###
##############################################
cp $scene_id.slc ../DInSAR/SLCs
cp $scene_id.slc.par ../DInSAR/SLCs
cp $scene_id.mli ../DInSAR/SLCs
cp $scene_id.mli.par ../DInSAR/SLCs
cp $scene_id.mli.tif ../DInSAR/IMG/IMG_mli

cd ..

done
```

Appendix D: DInSAR Sentinel-1 DInSAR-Processing Script

```
#!/bin/bash
# Sentinel-1 IW TOPS Processing using GAMMA Software
# Geocoding / coregistering / interferogram calculation
# Author: Simon Thorpe

### NOTE ###
# Run SLC_par_S1.tcsh prior to this script
# SLC_par_S1.tcsh creates SLC/MLI mosaics (deramped)
# Only IW2 subswath used for Rocky Mountain House - IW1 and 3 commented out

##################################################
### Creating list of InSAR pairs ###
##################################################
list=$(<list.txt)    # list of InSAR pairs
pair=($list)         # list to array
N_pair=${#pair[@]}   # number of InSAR pairs

#mkdir -p IMG/IMG_cc
#mkdir -p IMG/IMG_diff_unw
```

```
#mkdir -p IMG/IMG_diff_unw_utm

####################################################
### Loop through each InSAR pair ###
####################################################
for (( i=0; i<${N_pair}; i++ ))
do

   master=`echo ${pair[$i]}| awk -F '-' '{print $1}'`
   slave=`echo ${pair[$i]}| awk -F '-' '{print $2}'`
   master_slave=${master}_${slave}
   echo Processing interferogram pair $master_slave

   mkdir DIN_$master_slave
   cd DIN_$master_slave

   # Link to SLC files
   ln -s ../SLCs/$master.slc ./$master.slc
   ln -s ../SLCs/$master.slc.par ./$master.slc.par
   ln -s ../SLCs/$master.mli ./$master.mli
   ln -s ../SLCs/$master.mli.par ./$master.mli.par
   ln -s ../SLCs/$slave.slc ./$slave.slc
   ln -s ../SLCs/$slave.slc.par ./$slave.slc.par
   ln -s ../SLCs/$slave.mli ./$slave.mli
   ln -s ../SLCs/$slave.mli.par ./$slave.mli.par
   ln -s ../DEM/DEM ./DEM
   ln -s ../DEM/DEM_par ./DEM_par

   # Set parameters
   width=`awk '/range_samples/' $master.slc.par | awk -F ' ' '{print $2}'`  # number of samples of SLC
   lines=`awk '/azimuth_lines/' $master.slc.par | awk -F ' ' '{print $2}'`  # number of lines of SLC

   rlks=12  # number of range looks
   azlks=2  # number of azimuth looks

   width_ml=`expr $width / $rlks`    # number of multilooked samples
   lines_ml=`expr $lines / $azlks`   # number of multilooked lines

   ####################################################
   ### Generate DEM for each master ###
   ####################################################

   gc_map $master.mli.par - DEM_par DEM DEM_seg_par DEM_seg DEM.rough.map_to_rdc - - $master.sim_sar u v inc psi pix
ls_map 8 3 64

   width_dem=`awk '/width/' DEM_seg_par | awk -F ' ' '{print $2}'`   # number of samples of DEM
   lines_dem=`awk '/nlines/' DEM_seg_par | awk -F ' ' '{print $2}'`  # number of lines of DEM

   pixel_area $master.mli.par DEM_seg_par DEM_seg DEM.rough.map_to_rdc ls_map inc pix_sigma0 pix_gamma0
   create_diff_par $master.mli.par - $master.diff_par 1 0
   offset_pwrm pix_sigma0 $master.mli $master.diff_par $master.offs $master.snr 256 256 offsets 2 64 64
   offset_fitm $master.offs $master.snr $master.diff_par coffs coffsets - - 0
   gc_map_fine DEM.rough.map_to_rdc $width_dem $master.diff_par DEM.map_to_rdc 1
   geocode_back $master.mli $width_ml DEM.map_to_rdc $master.mli.map $width_dem $lines_dem 2 0
   raspwr $master.mli.map $width_dem 1 0 1 1 0.6 0.4 1 $master.mli.map.tif
   geocode DEM.map_to_rdc DEM_seg $width_dem $master.dem $width_ml $lines_ml 2 0

   ####################################################
   ### Coregistration TOPS mode ###
   ####################################################

   # Create RSLC_tab
   #echo $slave.iw1.rslc $slave.iw1.rslc.par $slave.iw1.rslc.TOPS_par > RSLC_tab
   echo $slave.iw2.rslc $slave.iw2.rslc.par $slave.iw2.rslc.TOPS_par > RSLC_tab
   #echo $slave.iw3.rslc $slave.iw3.rslc.par $slave.iw3.rslc.TOPS_par >> RSLC_tab

   # Link to ramped slc files for coregistering
   ln -s ../../$master/SLC_tab ./SLC1_tab
   ln -s ../../$slave/SLC_tab ./SLC2_tab
   ln -s ../../$master/$master.iw2.slc ./$master.iw2.slc
```

```
   ln -s ../../$master/$master.iw2.slc.par ./$master.iw2.slc.par
   ln -s ../../$master/$master.iw2.slc.TOPS_par ./$master.iw2.slc.TOPS_par
   ln -s ../../$slave/$slave.iw2.slc ./$slave.iw2.slc
   ln -s ../../$slave/$slave.iw2.slc.par ./$slave.iw2.slc.par
   ln -s ../../$slave/$slave.iw2.slc.TOPS_par ./$slave.iw2.slc.TOPS_par


   # STEP 1) Derive lookup table
   #rdc_trans $master.mli.par $master.dem $slave.mli.par $slave.mli.lt

   # STEP 2) Calculate offset using cross-correlation method
   #SLC_interp_lt_S1_TOPS SLC2_tab $slave.slc.par SLC1_tab $master.slc.par $slave.mli.lt $master.mli.par $slave.mli.par -
RSLC_tab $slave.rslc $slave.rslc.par
   #create_offset $master.slc.par $slave.slc.par $master_slave.off 1 $rlks $azlks 0
   #offset_pwr $master.slc $slave.rslc $master.slc.par $slave.rslc.par $master_slave.off offs snr 256 64 - 1 64 64
   #offset_fit offs snr $master_slave.off - - - 1 0
   #SLC_interp_lt_S1_TOPS SLC2_tab $slave.slc.par SLC1_tab $master.slc.par $slave.mli.lt $master.mli.par $slave.mli.par
$master_slave.off RSLC_tab $slave.rslc $slave.rslc.par
   #create_offset $master.slc.par $slave.slc.par $master_slave.off1 1 $rlks $azlks 0
   #offset_pwr $master.slc $slave.rslc $master.slc.par $slave.rslc.par $master_slave.off1 offs snr 256 64 - 1 64 64
   #offset_fit offs snr $master_slave.off1 - - - 1 0
   #offset_add $master_slave.off $master_slave.off1 $master_slave.off.total
   #SLC_interp_lt_S1_TOPS SLC2_tab $slave.slc.par SLC1_tab $master.slc.par $slave.mli.lt $master.mli.par $slave.mli.par
$master_slave.off.total RSLC_tab $slave.rslc $slave.rslc.par

   # STEP 3) Offset refinement using azimuth overlap regions
   #S1_coreg_overlap SLC1_tab RSLC_tab $master_slave $master_slave.off $master_slave.off.corrected 0.8 0.01 0.8 1
   #SLC_interp_lt_S1_TOPS SLC2_tab $slave.slc.par SLC1_tab $master.slc.par $slave.mli.lt $master.mli.par $slave.mli.par
$master_slave.off.corrected RSLC_tab $slave.rslc $slave.rslc.par
   #mv $master_slave.off.corrected $master_slave.off

   # GAMMA Script that does the above coregistration STEPS 1,2 and 3 and iterates for best coregistration
   S1_coreg_TOPS SLC1_tab $master SLC2_tab $slave RSLC_tab $master.dem  $rlks $azlks - - 0.6 0.02 0.8 1 0 # NOTE also
generates DInSAR ifg


   ###################################################
   ### Interferogram Filtering ###
   ###################################################

   adf $master_slave.diff $master_slave.adf.diff $master_slave.adf.cc $width_ml
   rasmph_pwr $master_slave.adf.diff $master.rmli $width_ml
   rascc $master_slave.adf.cc $master.rmli $width_ml - - - - - - - - - - $master_slave.adf.cc.tif

   ###################################################
   ### Phase Unwrapping ###
   ###################################################

   # Generate validity mask for phase unwrapping
   rascc_mask $master_slave.adf.cc $master.rmli $width_ml 1 1 - - - 0.3 - - - - - - $master_slave.adf.cc_mask.ras

   # Phase unwrapping using Minimum Cost Flow (MCF)
   mcf $master_slave.adf.diff $master_slave.adf.cc $master_slave.adf.cc_mask.ras $master_slave.adf.unw $width_ml 1 - - - - 1 1 - - -
   rasrmg $master_slave.adf.unw $master.rmli $width_ml - - - - - - - - - - $master_slave.adf.unw.tif

   ###################################################
   ### Create Displacement Map ###
   ###################################################

   dispmap $master_slave.adf.unw $master.dem $master.slc.par $master_slave.off $master_slave.disp 1
   rashgt $master_slave.disp $master.rmli $width_ml - - - - - 0.05 - - - $master_slave.disp.tif

   ###################################################
   ### Geocoding Displacement Map and Unwrapped IFG ###
   ###################################################

   # Geocoding unwrapped ifg
   geocode_back $master_slave.adf.unw $width_ml DEM.map_to_rdc $master_slave.adf.unw.geo $width_dem $lines_dem 2 0
   rasrmg $master_slave.adf.unw.geo $master.mli.map $width_dem - - - - - 1 - - - $master_slave.adf.unw.geo.tif
```

```
# Geocoding displacement
geocode_back $master_slave.disp $width_ml DEM.map_to_rdc $master_slave.disp.geo $width_dem 0 0 0
rashgt $master_slave.disp.geo $master.mli.map $width_dem - - - - - 0.05 - - - $master_slave.disp.geo.tif

# Clean space
rm $slave.iw2.rslc
rm $slave.slc
rm $master.rslc
rm $slave.rslc

mv $master_slave.adf.unw.tif ../IMG/IMG_diff_unw/
mv $master_slave.adf.cc.tif ../IMG/IMG_cc/

cd ..

echo processing complete for pair $master_slave

done
```

Appendix E: DInSAR resampling to MSBAS script

```
#!/usr/bin/env bash

rpos=1793
azpos=736
rad=40
CC=0.4

rm msbas_files.txt
while read n m s bp ts t1 t2 t3 t4
do

        echo $n $m $s
        master=$m"_HH"
        echo $master
        width=`awk '$1 == "range_samples:" {print $2}' $master.rmli.par`
        length=`awk '$1 == "azimuth_lines:" {print $2}' $master.rmli.par`
        width_dem=`awk '$1 == "width:" {print $2}' ../../geo/ni_seg.dem_par`
        length_dem=`awk '$1 == "nlines:" {print $2}' ../../geo/ni_seg.dem_par`
        lat=`awk '$1 == "corner_lat:" {print $2}' ../../geo/ni_seg.dem_par`
        lon=`awk '$1 == "corner_lon:" {print $2}' ../../geo/ni_seg.dem_par`
        latstep=`awk '$1 == "post_lat:" {print $2}' ../../geo/ni_seg.dem_par`
        lonstep=`awk '$1 == "post_lon:" {print $2}' ../../geo/ni_seg.dem_par`
        lat1=`echo $lat $latstep $length_dem | awk '{print ($1+$2*$3);}'`
        lon1=`echo $lon $lonstep $width_dem | awk '{print ($1+$2*$3);}'`

        f=`pwd`"/dint_refined/"$m"_HH_"$s"_HH"
        echo $f
        # extract computes an average coherence in the window, it is similar to grdinfo -L2
        acc=`./extract $f.adf.cc $width $length $rpos $azpos $rad 0 0 1 1`
        echo $acc
        flag=`echo "$acc $CC" | awk '{if ($1>$2) {print 1} else {print 0;}}'`

        if [ $flag -eq 1 ]; then

                echo $n $m $s $bp $ts $t1 $t2 $t3 $t4 >> msbas_bperp_file

                dispmap $f.adf.unw - ../$master.slc.par $f.off $f.disp 0
                geocode_back $f.disp $width ../../geo/ni_1.map_to_rdc $f.disp.geo $width_dem 0 0 0
                gmt xyz2grd $f.disp.geo -G$f.disp.geo.grd -R$lon/$lon1/$lat1/$lat -I$width_dem+/$length_dem+ -ZTLfw -d0
                gmt grdsample $f.disp.geo.grd -G$f.disp.geo.grd.cut -R-94.75/-93.89/31.49/32.23 -I3.5e-04=/3.5e-04=
                gmt grdmath $f.disp.geo.grd.cut 100 MUL = $f.grd #convert to cm
                gmt grd2xyz $f.grd -d0 -ZTLfw > $f.msbas
                interp_ad $f.msbas $f.msbasi `gmt grdinfo $f.grd | grep x_min | awk '{print $11}'` 16 16 16
                rasrmg $f.msbasi - `gmt grdinfo $f.grd | grep x_min | awk '{print $11}'` 1 1 0 1 1 1
                echo $f.msbasi $bp $m $s >> msbas_files.txt
                rm $f.disp  $f.disp.geo $f.disp.geo.grd $f.disp.geo.grd.cut
        fi
done < bperp_file
```

Curriculum Vitae

Name: Simon Douglas Thorpe

Post-secondary Education and Degrees:
University of Leeds
Leeds, UK
2011-2015 B.Sc., MGeophys

Western University
London, Ontario, Canada
2015-2017 M.Sc. Geophysics

Honours and Awards:
Western Graduate Research Scholarship
2015 – 2017

Related Work Experience
Teaching Assistant
Western University
2015-2017

Publications:

Thorpe, S. and Tiampo, K.F. 2016. S43C-2875: Mapping Fluid Injection and Associated Induced Seismicity Using InSAR Analysis *In*: *AGU Fall Meeting*. San Francisco, US.

Thorpe, S., Tiampo, K.F., Samsonov, S. V., Shirzaei, M. and González, P.J. 2017. Time series analysis of surface deformation associated with fluid injection and induced seismicity in Timpson, Texas using DInSAR methods *In*: *CGU-CSAFM National Meeting*. Vancouver, Canada.